Correlative X-ray Microscopy Studies of CuIn$_{1-x}$Ga$_x$Se$_2$ Solar Cells

by

Bradley West

A Dissertation Presented in Partial Fulfillment
of the Requirements for the Degree
Doctor of Philosophy

Approved January 2018 by the
Graduate Supervisory Committee:

Mariana I. Bertoni, Chair
Darren Verebelyi
Zachary Holman
Volker Rose

ARIZONA STATE UNIVERSITY

May 2018

ABSTRACT

It is well known that the overall performance of a solar cell is limited by the worst performing areas of the device. These areas are usually micro and nano-scale defects inhomogenously distributed throughout the material. Mitigating and/or engineering these effects is necessary to provide a path towards increasing the efficiency of state-of-the-art solar cells. The first big challenge is to identify the nature, origin and impact of such defects across length scales that span multiple orders of magnitude, and dimensions (time, temperature etc.). In this work, I present a framework based on correlative X-ray microscopy and big data analytics to identify micro and nanoscale defects and their impact on material properties in $CuIn_{1-x}Ga_xSe_2$ (CIGS) solar cells.

Synchrotron based X-ray Fluorescence (XRF) and X-ray Beam Induced Current (XBIC) are used to study the effect that compositional variations, between grains and at grain boundaries, have on CIGS device properties. An experimental approach is presented to correcting XRF and XBIC quantification of CIGS thin film solar cells. When applying XRF and XBIC to study low and high gallium CIGS devices, it was determined that increased copper and gallium at grain boundaries leads to increased collection efficiency at grain boundaries in low gallium absorbers. However, composition variations were not correlated with changes in collection efficiency in high gallium absorbers, despite the decreased collection efficiency observed at grain boundaries.

Understanding the nature and impact of these defects is only half the battle; controlling or mitigating their impact is the next challenge. This requires a thorough understanding of the origin of these defects and their kinetics. For such a study, a temperature and atmosphere controlled *in situ* stage was developed. The stage was utilized to study CIGS films during a rapid thermal growth process. Comparing composition variations across different acquisition times and growth temperatures required the implementation of machine learning techniques,

including clustering and classification algorithms. From the analysis, copper was determined to segregate the faster than indium and gallium, and clustering techniques showed consistent elemental segregation into copper rich and copper poor regions. Ways to improve the current framework and new applications are also discussed.

ACKNOWLEDGMENTS

Had you spoken to me five years ago, I would have never guessed that today I would be preparing to defend my dissertation. It is almost surreal, until I remember all the hard work it took to get here, and I have so many people to thank who have helped me throughout this journey.

First and foremost, I want to thank my advisor Professor Mariana Bertoni. I would not be in the position I am in today without her. She was the one who encouraged me to pursue a Ph.D., and has continued to encourage me every step of the way, even when she thought I was going crazy and "seeing things" in the data. Hopefully, I've made my case since then, that yes they are grains. Her advice and mentorship have made me a better researcher, taught me the importance of knowing your audience, and given me the confidence in my abilities and to pursue my ideas in the future.

I would also like to thank the rest of my committee. Dr. Darren Verebelyi has been a part of this process since almost day one, and was one of the first people I met in the CIGS community. His insight and feedback have been invaluable and I appreciate his ability to ask the important questions. I want to thank Professor Zachary Holman, who gave me my first introduction to semiconductor device physics, and helped me build the knowledge base necessary for me to pursue this work. I also want to thank Professor Volker Rose, for the fruitful conversations during the seemingly endless experiments at Sector 26. I would also like to acknowledge the rest of my collaborators at APS, Dr. Barry Lai and Dr. Jörg Maser. Thank you for teaching me and sharing your love of X-ray science, and contributing to all the experiments we ran at APS.

I want to thank Professor William Shafarman, Robert Lovelett, Lei Chen, and Sina Soltanmohammad from the University for Delaware, for all of the solar cells, precursor stacks, substrates, and input and feedback on experimental design and our results. This work would not have been possible without your assistance and collaboration. I also want to acknowledge

QESST for providing avenues for the collaboration to exist. To our collaborators at NREL, Dr. Harvey Guthrey and Dr. Mowafak Al-Jassim: Thank you for the rewarding collaboration, support over the years. I particularly appreciate you sharing your expertise in materials characterization and knowledge of grain boundaries. I am especially grateful for the two weeks I was able to spend at NREL learning about CIGS growth processes, the FIB, and cathodoluminescence. I would also like to acknowledge John Mosely for the introduction to the watershed technique.

I want say how grateful I am to have had the opportunity to work so closely with my postdoc Michael Stuckelberger. I have thoroughly enjoyed learning from his seemingly endless depth of knowledge and working together to tackle new problems. His tenacity to always broaden his understanding and ask more questions is contagious, and his desire to pass that knowledge along to others made him an excellent mentor.

To my teammates (both current and former) in the DEfECT Lab: April, Simone, Tiné, Laura, Pablo, Sebastian, Sri, Xiaodong, Genevieve, Jake, Nick, Michael (the younger), Trumann, and Tara. Thank you for making the ERC a fun place to work, Tempe a fun place to live, and being so giving with your time, providing thoughtful feedback, and/or beers, whenever needed.

I have treasured the encouragement and confidence I have received from my family. Their assurance throughout this process helped me persevere. And last but absolutely not least, thank you to my boyfriend Killian, for always being there for me, moving across the country to support me, and your unwavering certainty that I could do this. I love you.

TABLE OF CONTENTS

LIST OF TABLES

LIST OF FIGURES

Chapter 1

INTRODUCTION

1.1   The Case for Thin Film Photovoltaics

Energy is a vital resource for both developing and developed societies. Global power
demands are expected to increase from $17\,\mathrm{TW}$ today to $20\,\mathrm{TW}$ by 2050, and renewable energy
resources are necessary to keep up with increasing demand [1]. Of the energy resources
available solar energy is by far the most abundant with $\sim 165{,}000\,\mathrm{TW}$ hitting the earth's
surface constantly every day [2]. While not all of this energy is available to use (plants need
access to the suns power to convert CO_2 to O_2), or is easily accessible (oceans make up 72%
of the earths surface), the magnitude of the resource is remarkable. Roadmaps toward 100%
renewable power generation in the United States estimate that solar energy will make up $\sim 45\%$
of power generation in 2050 through a combination of photovoltaics (PV) and concentrated
solar power, with a majority coming from utility scale and rooftop PV [3].

A common argument against the viability of renewable energy sources, and particularly
photovoltaics, is the cost. In 2011 the U.S. Department of Energy launched the SunShot
Initiative, with the goal of reducing the cost of utility scale photovoltaic (PV) systems to 1
$/W by 2020. Today this program is three years ahead of schedule with the price of fixed tilt
utility scale solar dropping to 0.99 $/kWh equivalent to 6 ¢/kWh levelized cost of electricity
assuming 20% module efficiency, 0.2% degradation over 30 years, and 1.1 $/W installation
costs [4–6]. These advancements also coincide with solar energy reaching grid parity in 20
states, meaning PV electricity costs equivalent to or less than current grid prices [7].

While these advancements are impressive and highlight the great potential for PV to be an

abundant, cost effective, and clean source of electricity, there is still room for improvement. Commercial PV module efficiencies are still less than half the theoretical limit for single junction devices, and low-cost multi-junction devices have yet to be realized. In addition to this, efficiency has been identified to have the largest impact on reducing system cost for silicon based PV modules [8]. Aside from cell and module level efficiencies, the full lifecycle of the PV system needs to be considered. This includes the energy required to mine, and process raw materials, module installation costs, and costs associated with generation and dispatching of electricity [9, 10]. It is from this perspective that technologies alternative to silicon, which currently dominates the market, become more attractive.

Thin film technologies have an inherent lower manufacturing cost than wafer based technologies, since they use in-line deposition systems. Thin film technologies are polycrystalline, and growth of polycrystalline (PC) absorbers are generally faster, cheaper and less energy intensive than single crystals, leading to, among other things, a reduced energy payback time for the final module [11]. Even multicrystalline silicon cut from cast ingots, benefits from less expensive process when compared to CZ crystal growth furnaces. As of 2015, PC absorbers accounted for 76% of the global module production. Of these PC modules, an overwhelming majority (90%) are PC silicon modules, with the remaining 10% coming from thin film technologies based on CdTe and $Cu(In,Ga)Se_2$ (CIGS) absorber layers [12].

Thin film modules require much lower material usage ($\sim 5\,\mu m$ for active layers of CIGS cells) compared to $150\,\mu m$ for typical silicon cells. This low material usage also enables deposition on flexible substrates like stainless steel foil, or polymers, increasing the number of applications PV systems from outdoor gear (camping tents and backpacks) to wearable PV (solar powered t-shirts and gloves) [13]. It also reduces the balance-of-system costs for traditional applications, for utility or rooftop scale deployments. Another benefit of the reduced weight, is the capability to deploy rooftop PV on low weight bearing structures, and

2

the implementation into buildings (BIPV) [14]. Flexible CIGS modules would also be ideal for rooftop installations in rural areas of developing countries, where low weight bearing structures are more common and distributed energy generation is essential as well as more economical.

1.2 Motivation

Despite many of these apparent advantages of thin films over silicon cells, they also pose unique challenges. Firstly, the semiconductors used for the absorber layers are inherently more complicated, from binary systems like CdTe to quaternary systems in the case of CIGS. This does not include other binary and ternary compounds used for device completion, from buffer layers to transparent conducting oxides. Adding to the complexity is the large number of defects present in these systems from point defects like vacancies and anti-sites to planar defects like grain boundaries, surfaces and interfaces. These defects can cause the material to be non-homogeneous on a length scale from nanometers (around grain boundaries) to micrometers (between grains and layers) making it complicated to decipher how individual defects contribute to device performance. Because of this, many advances in efficiency made of these devices have been the result of guided empiricism. The lack of understanding at these scales really limits our ability to further improve the performance of these devices and engineer the absorber by promoting the beneficial defects and limiting the negative ones.

While it may be counter intuitive that 'defects' can be beneficial, there are many examples of this throughout the PV industry. On a very basic level dopants are defects, purposely introduced to give semiconductors the desired conductivity. Hydrogen passivation of grain boundaries in polycrystalline silicon is known to reduce their recombination activity [15]. $CdCl_2$ treatments for CdTe solar cells has been shown to increase collection at grain boundaries, by creating a local p-n homojunction [16]. Similarly, the diffusion of Na from the soda lime

3

glass substrate typically used in CIGS solar cells is critical to reducing defect density at grain boundaries and increasing the carrier concentration [17, 18]. Understanding the origin of defects and their impact on device performance allows for the engineering of the absorber properties to increase the efficiency.

The motivation for the study of CIGS solar cells lies, in particular, behind the complexity and tunability of the system. The composition window of the CIGS phase is wide and stable, by changing the relative abundance of Group III elements (Ga/[Ga+In]) the bandgap can be varied and changing the ratio between Group I and Group III elements (Cu/[Ga+In]) the carrier concentration can be varied. This is achievable without producing secondary phases [19]. This same flexibility with respect to composition is not available in the CdTe system. The CIGS system can also readily alloy with other elements. For example, silver is sometimes used to replace copper, and sulfur is used to replace selenium, to provide more control over the position of the band edges. This provides a wide parameter space to investigate the relationship between elemental variations and device performance. Additionally, this wide material space is also available on the industrial scale, enabling advances on the laboratory scale to quickly upscale. For example, depth dependent gallium grading, an advancement made on the laboratory scale, is currently standard process for industrial CIGS module manufacturers to achieve a better back surface field and carrier transport.

This compositional flexibility inherently results in inhomogeneities at the micro and nanoscale. Inhomogeneities can have both positive and negative effects on device properties. The goal of this work is to correlate these inhomogeneities with macro scale device properties to understand which variations result in relative improvements and which are detrimental. I also propose to understand the origin of these inhomogeneities and their formation kinetics with the goal of providing a pathway towards defect engineering absorber layer properties, by promoting beneficial defects and suppressing detrimental ones.

4
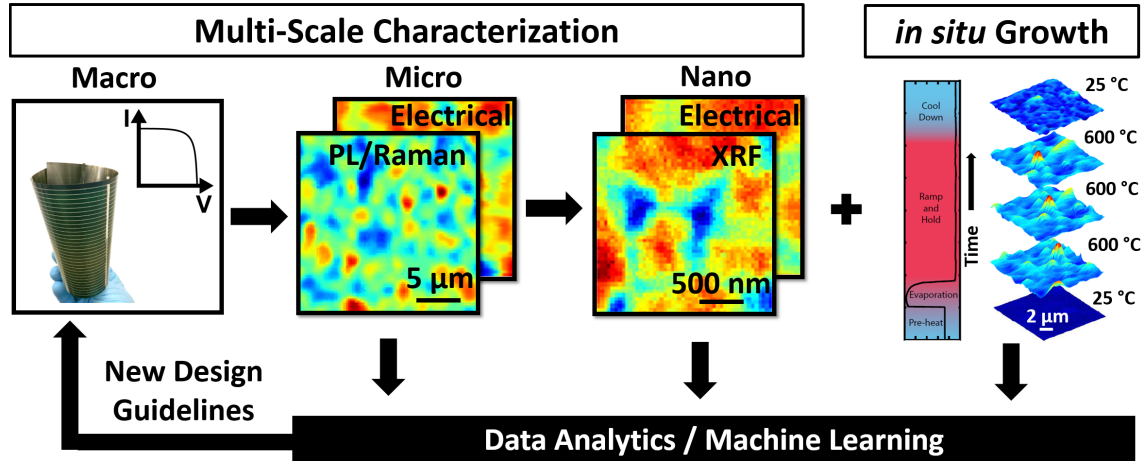
Figure 1.1 Schematic showing multi-scale correlative microscopy, in combination with *in situ* characterization of absorber layer growth. The results of these studies are quantitatively analyzed, via image processing and machine learning techniques to generate new design guidelines for improving device performance.

1.3 Approach

To tackle this challenge I developed and implemented a characterization framework depicted in Fig. 1.1 to study the effect of inhomogeneities on electrical properties of CIGS devices, and their origins via in-situ studies. Full device characterization is done at the macro scale including light and dark I-V characterization. Photoluminescence and Raman microscopy are conducted at the micro scale, with the addition of LBIC/LBIV done simultaneously. X-ray characterization is utilized at the nanoscale correlating composition from X-ray fluorescence and electrical properties from X-ray beam induced current and voltage. Combining the learnings obtained from state-of-the-art devices, and learnings from *in situ* growth studies to understand how these material properties arise, new design guidelines are proposed to improve device efficiency. Each characterization technique generates large amounts of data, requiring the use of image processing and machine learning techniques to ensure that all the trends in the data are captured.

5

While this work does not focus on device fabrication, we strive to develop deeper understanding of how CIGS behaves under operation and the origin of the behavior, using a data driven approach, to provide pathways for those who do fabricate devices to push the efficiency higher.

In the following sections we will provide background on the current state of CIGS based solar cells, what is known and still under debate. Synchrotron based X-ray microscopy techniques used to study the material will be introduced, as well the methodology developed to accurately handle the resulting data. Chapter 4, these techniques are applied to improve the understanding of composition variations and their impact on charge collection at grain-to-grain (micoscale) and at grain boundaries (nanoscale). Chapter 5 presents the effect of Na concentration on CIGS devices and inhomogeneities in the absorber layer. Chapter 6, presents the design of an *in situ* stage to study the growth of CIGS absorber layers via X-ray fluorescence, as well as the study of copper segregation during CIGS growth.

Chapter 2

BACKGROUND

The performance of a solar cell determined by its efficiency (the maximum electrical power output obtained for a given incident power coming from the sun [20]. This is shown in Eq. 2.1,

$$\text{Efficiency} = \frac{V_{oc} \cdot J_{sc} \cdot \text{FF}}{P_{in}} \qquad (2.1)$$
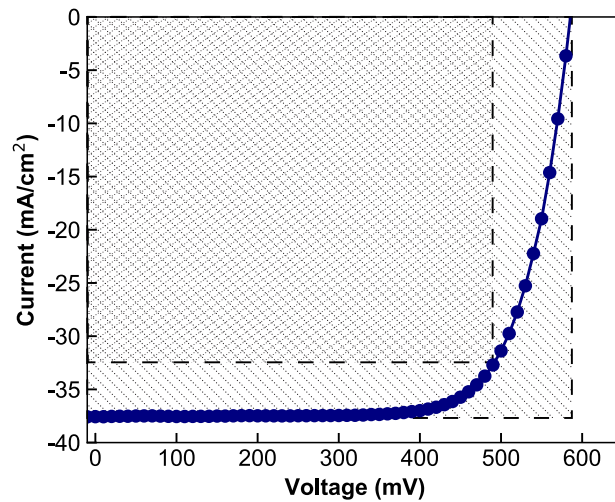
Figure 2.1 Representative I-V Curve of a solar cell

where V_{oc} is the open circuit voltage measured in volts, J_{sc} is the short circuit current measured in mA/cm^2. FF is the fill factor of the device, as a percentage, and P_{in} is the incident power in mW/cm^2. Figure 2.1 shows a representative I-V curve of a solar cell. V_{oc} is the maximum voltage that can be produced in the cell. It can be seen as the x-intercept of Fig. 2.1. The open-circuit voltage is dependent the bandgap of the absorber layer and carrier recombination. J_{sc} is the maximum current that can be produced by the cell. This is identified

7

by the y-intercept of Fig. 2.1. The short circuit current is most sensitive to the intensity of the incident light, number of carriers absorbed, and to a smaller extent recombination. FF is a term that accounts for losses within solar cell. It is the ratio of the maximum power theoretically achievable (V_{oc} x J_{sc}) and the power achievable at the maximum power point along the I-V curve, or ratio of the larger and the smaller hatched boxes in Fig. 2.1.

2.1 $CuIn_{1-x}Ga_xSe_2$ Thin Film Solar Cells

Copper Indium Gallium Diselenide, $CuIn_{1-x}Ga_xSe_2$, absorber layers are uniquely suited for low cost and high efficiency solar cells as described previously. The highest certified record efficiency achieved for small area laboratory scale devices is currently 22.6% [21] with approximately 30% gallium concentration relative to indium. The following sections describe the device fabrication, tolerance to some defects, and current challenges associated with increasing efficiency. Historical advances in CIGS record device performance are shown in Fig. 2.2. Between 1990 and 2000 major advances were made via the implementation of the 3-stage growth process developed at the National Renewable Energy Laboratory (NREL) and depth dependent bandgap grading [22, 23]. Up until 2013, advances were made by improving the buffer layer deposition and improving current collection [24]. More recently, advances have been made through the use of NaF and KF post deposition treatments [21, 25], with heavier alkali elements (RbF and CsF) currently being investigated. Moving forward defect engineering is going to become more important, as once minor efficiency losses become more detrimental.
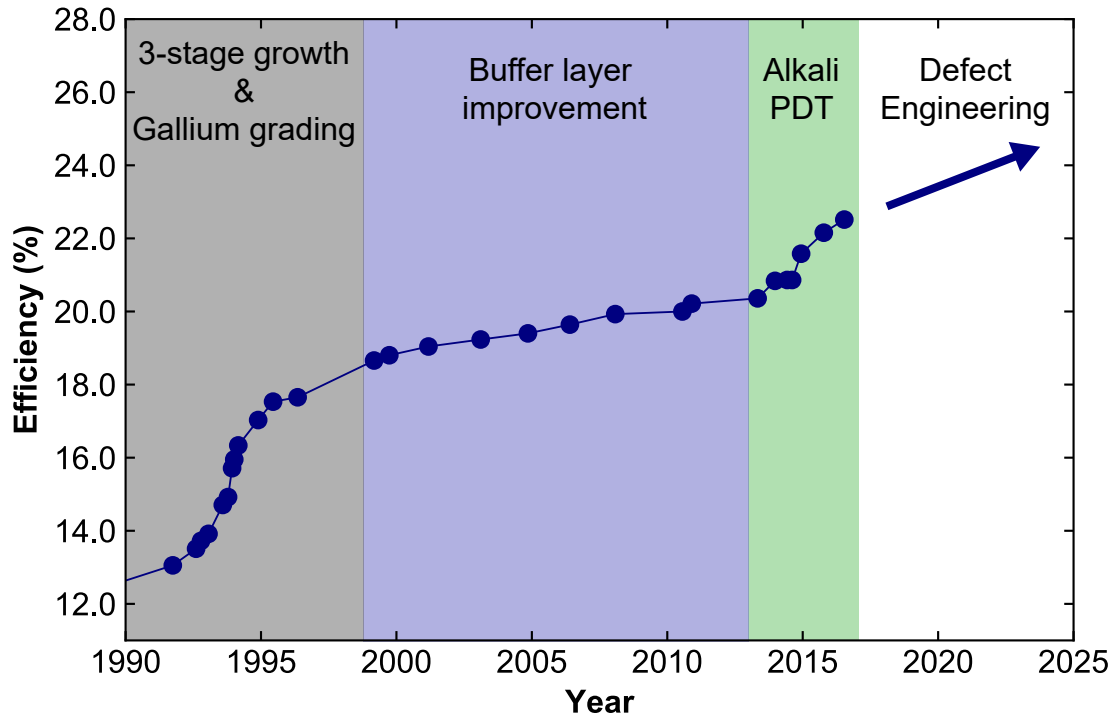
Figure 2.2 Improvement of CIGS device performance over time, highlighted by technological advance.

2.1.1 Device Fabrication

A state of the art CIGS device structure is shown in Fig. 2.3. The substrate is typically soda lime glass (SLG), with a sputtered molybdenum back contact $\sim 700\,\mathrm{nm}$ thick. Soda lime glass is commonly used because of the beneficial effects of Na that diffuses into the CIGS layer during growth. Flexible alternatives to SLG are also a topic of study including polyimide, and stainless steel. These substrates however tend to result in poorer performing devices [26]. Polyimide substrates for example limit the maximum growth temperature of CIGS [27], and stainless steel substrates can introduce metal contamination needs to be mitigated through the use of barrier layers [28]. Additionally, the lack of alkali metals in common flexible alternatives

9

to SLG are sodium free, require new methods to introduce sodium during and post growth [27, 29, 30].
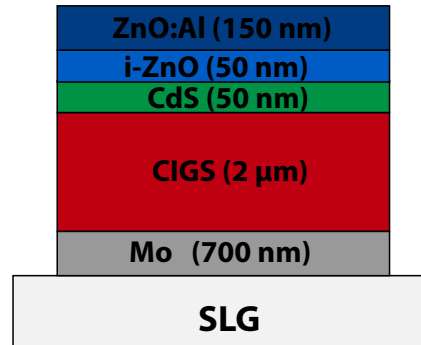
Figure 2.3 Typical CIGS device structure

Molybdenum is the most common back contact because the formation of $MoSe_2$ during growth promotes CIGS/Mo adhesion and creates an ohmic contact [31]. Alternative back contacts have been investigated including: W, Cr, Ta, Nb, V, Ti, Mn. The only viable alternatives that produced comparable efficiencies were W and Ta. Cr, Ti, V, Mn have shown to be unstable during CIGS deposition, and Nb results in poorer device performance [32]. Indium tin oxide has also been proposed as a transparent back contact for CIGS to enable bifacial devices [33].

A p-type CIGS absorber layer is approximately $2\,\mu m$ thick and typically grown by a co-evaporation or selenization process. Co-evaporated CIGS has produced the record lab scale devices, first reported by NREL [22]. In this process elemental Cu, In, and Ga are evaporated under vacuum with excess selenium beneath a heated substrate. The growth temperature is typically between $500\,°C$ and $600\,°C$. The process can be done in one-stage, where the three cations are evaporated simultaneously, or in a three-stage process that has been shown to produce larger grains by starting and ending the deposition with a copper deficient CIGS

phase and a copper rich phase in between [34]. An advantage of the three-stage process is the improved control over composition gradients and stoichiometry. Selenization is a two-stage process where metal precursors (either elemental Cu, In and Ga, or selenium containing compounds) are deposited via sputtering or electroplating on a substrate and the growth process takes place in a second chamber in the presence of H_2Se or elemental selenium to complete the CIGS growth. This process was developed by ARCO Solar Inc. [35] as an industrial alternative to co-evaporation, in its ability to handle larger substrates and result in less material loss during growth [36]. To date, the highest efficiency (19.2%) large area ($0.8\,m^2$) modules have been produced by Solar Frontier via coevaporation [37].

Alternative low-cost high throughput non-vacuum growth process have also been proposed. Such methods are of interest given the high capital expenditure associated with high vacuum equipment and reviewed in [38]. Methods include, rapid thermal processing of precursors layers [39, 40], electroplating [41], inkjet printing [42], and spray pyrolysis [43].

Cadmium Sulfide, $\sim 50\,nm$, is the n-type buffer layer commonly deposited by chemical bath deposition. The use of cadmium however has ignited many environmental and health concerns due to its toxicity, and prompted the study of alternate buffer layers [44]. Alternatives including, InS [45], ZnS [46], and Zn(Mg,O) [47] have achieved efficiencies >16%, with Zn(O,S) emerging as the most promising replacement. Alternative buffer layers have been deposited by both chemical bath deposition and atomic layer deposition. To date Zn(O,S) buffer layers are used in Solar Frontier's record CIGS module [37] and achieved efficiencies comparable to record CdS devices on the laboratory scale [48]. i-ZnO and aluminum doped zinc oxide (ZnO:Al) are sputter coated as the transparent conductive front contact. i-ZnO is often used as a resistive layer to reduce the impact of poor performing regions of the device, and limit shunt paths. Alternatively to ZnO:Al, indium doped tin oxide (ITO) can be used. ZnO:Al is the preferred transparent contact for the studies presented in the following chapters

to prevent convolution of the indium fluorescence from ITO and the fluorescence from the absorber layer [49]. The final device has a metalization grid made of Ni/Al fingers and MgF_2 as an anti-reflective coating.

2.1.2 Defect Tolerance

One of the most interesting properties of the CIGS system is the ability it has to handle large composition variations. By substituting gallium for indium, the bandgap can be tuned from 1.04 to $1.67\,eV$ for $CuInSe_2$ (CIS) to $CuGaSe_2$ (CGS) respectively. The change in bandgap is largely dominated by an increase in the conduction band minimum with increasing gallium incorporation [50]. Record devices take advantage of this property and utilize a double bandgap grading that decreases from the CdS/CIGS interface to a minimum, and then increases towards the CIGS/Mo interface. This provides a beneficial effect of decreasing recombination in the space charge region at the CdS/CIGS interface, and imparts a back surface field to reduce recombination at the back contact [23]. The copper stoichiometry is normally referred to as by [Cu]/[Ga+In] or CGI. Recent high efficiency devices (>20%) have been prepared with CGI ranging from 0.8 – 0.9 [51].

Figure 2.4 shows the unit cell of the CIGS chalcopyrite (α phase). The unit cell is tetragonal, with a c/a ratio of $\sim$ 2. For $CuInSe_2$, a $= 0.579\,nm$ and c $= 1.162\,nm$ [19]. The single phase region of α-CIGS exists over a narrow composition range, and typical copper poor CIGS films are a mixture of α-CIGS and β-CIGS. The β phase has the same structure as the α phase but a different stoicheometry ($CuIn_3Se_5$), leading to one copper atom missing from a copper site in the α-CIGS unit cell.

To describe defects in a consistent way, like one missing copper atom, Kröger-Vink defect notation is used [52]. The notation is from the point of view of the defect and not the matrix.
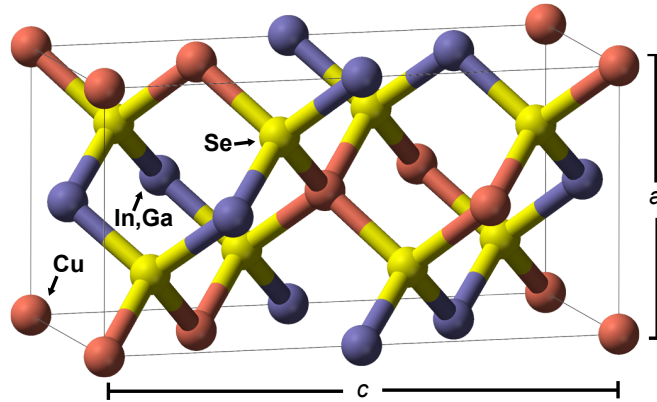
Figure 2.4 Unit cell of the CIGS chalcopyrite structure. Red = Copper, Blue = In,Ga, Yellow= Selenium.

It is as follows: Z_S^C, where Z is the species of interest, such as an atom (Cu, In, Ga, etc.), or a vacancy (V). S corresponds to the lattice site that the species occupies. C is the electronic charge of the species relative to the site it occupies, with ● representing a single positive charge (donor), ′ representing a single negative charge (acceptor), and **x** representing neutral charge. The calculation of the relative charge is shown in Eq. 2.2, and Table 2.1 shows examples of various defect notations for the CIGS system, their description in words, and the calculation of the charge state.

$$\text{Charge State} = \text{Species Charge} - \text{Site Charge} \qquad (2.2)$$

Table 2.1 Examples of Kröger-Vink defect notation.

Notation	Description	Charge Calculation
Se_{Se}^x	Selenium atom, occupying a selenium site with a neutral charge	(-2) - (-2) = 0
V_{Cu}'	Vacancy (no atom) on a copper site with a charge of -1	0 - (+1) = -1
$In_{Cu}^{\bullet\bullet}$	Indium atom, occupying a copper site with a charge of +2	(+3) - (+1) = +2
Se_i''	Selenium atom, occupying an interstitial site with a charge of -2	(-2) - 0 = -2

It is widely accepted that the electrical performance of CIGS devices is enhanced by the

13

presence of structural defects like grain boundaries given that high efficiency polycrystalline devices (>18%), with small grain sizes between 1-2 μm, significantly outperform their mono-crystalline counterparts (12.5 %) [53]. While the origin is not entirely agreed upon, we show in the following discussion, that many studies have looked into the impact of extrinsic chemical passivation of boundaries, as well as intrinsic compositionally induced field effect passivation. Extrinsic passivation of grain boundaries has been argued to occur with the addition of O_2 by air annealing and sodium ions entering the film from the soda lime glass substrate during growth. Post deposition anneal of the CIGS film in air at $200\,°C$ for 30 min has been shown to boost device performance by annihilating the double donor defect $V_{Se}^{\bullet\bullet}$ and creating O_{Se}^x [54] and Na is argued to catalyze this effect [17].

The conductivity of CIGS is largely driven by native defects associated with composition deviations from stoichiometry and growth methods. By growing the sample cation rich the conductivity is n-type and by growing cation poor the conductivity is intrinsically p-type [55]. Copper vacancies (V_{Cu}') are beneficial to device performance because they act as shallow acceptor states with a low formation energy, which have been linked to p-type doping and charge carrier concentration [56]. Local density-functional approximation has been used to find that the beneficial V_{Cu}' also readily forms a defect pair with a potentially detrimental deep donor state $In_{Cu}^{\bullet\bullet}$. The defect pair ($2V_{Cu}' + In_{Cu}^{\bullet\bullet}$) even though it has a very low formation energy it is electrically inactive [57]. State of the art devices are grown copper poor to promote these native copper vacancies, increasing the p-type conductivity.

Reports based on first principle calculations have suggested that cation terminated grain boundaries in the form of V_{Cu}' or $In_{Cu}^{\bullet\bullet}$ induce a valance band offset generating the aforementioned field effect passivation. Persson and Zunger presented in [58] the energetically favorable formation of Cu-poor grain boundaries for (112) polar surfaces in CIS. Note that a majority of grains in CIGS are (112) oriented. They propose that the Cu depleted surface

decreases the valance band maximum (VBM) caused by the repulsion of the Cu-d and Se-p orbitals. Cu-p orbitals push the VBM upward, thus a Cu-depleted boundary will have a lower VBM, creating a barrier for holes. When this work was expanded [59] to compare CIS and CGS grain boundaries, it was observed that the valance band offset is more pronounced in CIS than in CGS. Cu-depleted boundaries in CGS films also result in an increase in the conduction band minimum (CBM) creating a barrier for electrons and holes. Yan et al. [60] reached a similar conclusion in their density functional theory calculations and proposed that sodium plays a role as well. They calculated a large segregation potential for sodium between 2.2 and $2.4\,\mathrm{eV}$ relative to the grain interiors, and argued that it occupies an interstitial site between two selenium dangling bonds.

A wide variety of experimental techniques have been used to investigate and corroborate the results from first principle calculations, and the results have been varied. Atom probe tomography has been combined with electron backscatter diffraction (EBSD) to investigate composition variations in CIGS at grain boundaries [61]. The boundary investigated showed an increase in the copper concentration and decrease in indium concentration, which is contrary to the results of Persson and Zunger. However, the boundary did exhibit a high concentration of O, Na, and K atoms, supporting arguments towards extrinsic grain boundary passivation. Energy dispersive X-ray spectroscopy (EDS) has been utilized in a transmission electron microscope also to investigate the composition variation around grain boundaries. Several boundaries were investigated and no composition variations were detected between grains or at the grain boundaries above the detection limit [62]. Cathodoluminescence spectroscopy (CLS) and micro-auger electron spectroscopy (AES) were combined to investigate the correlation between composition and band gap fluctuations at some grain boundaries in CIGS prepared by cleaving under high vacuum [63]. Boundaries showed a decrease in copper concentration relative to the grain cores, which could correlate to increase in the number of V'_{Cu}. This

15

result agrees well with the findings by Persson and Zunger. Electron beam induced current (EBIC) and EBSD were combined to determine the role that structure plays on the electronic behavior of grain boundaries. Looking at a CIGS films in cross section it was determined that twin boundaries do not contribute to increased collection and grain orientation was not correlated to increased collection at boundaries [64]. CLS has also been used to investigate bandgap fluctuations and trap states with high spatial resolution. A red shift is observed at grain boundaries which are argued to act as hole barriers leading to reduced recombination [65]. Contrary to first principle calculations, these results find a smaller bandgap at the boundary, rather than an increase.

I have chosen to highlight several of the scanning electron beam based measurements, because of their ability to correlate composition, structure and electrical properties; however, scanning probe microscopy (SPM) has been widely used as well. SPM is used to determine surface potential variation, capacitance, and current collection variations between grains and grain boundaries in CIGS [66–69].

2.1.3 Challenges to increasing efficiency

While these composition variations and the corresponding bandgap variations can have some beneficial effects in CIGS cells it is also estimated to be a limiting factor in the efficiency. It was proposed by Siebentritt, that the dark saturation current density (j_0) is the limiting factor in record efficiency CIGS devices which is dominated largely by recombination due to electrostatic potential fluctuations (non-uniform energy bands both in energy and lateral position) originating from charged defects, like dislocations and grain boundaries [70]. While current losses are a factor, relating to 3% absolute efficiency decrease, almost 7% absolute efficiency could be gained through a voltage increase by minimizing or eliminating these

fluctuations, bringing j_0 closer to its theoretical minimum. The relationship between V_{oc} and j_0 are described in equations 2.3 and 2.4, where n is the diode ideality factor, kT is the thermal energy, q is the elemental charge of an electron, j_{ph} is photogenerated current, j_{00} is a current prefactor term, $\bar{E}_g$ is the average bandgap, and $\sigma = \sqrt{\sigma_{eg} + \sigma_{el}}$ accounting for the contribution from both bandgap and electrostatic potential fluctuations [70–72].

$$V_{oc} = \frac{nkT}{q} \ln(\frac{j_{ph}}{j_0}) \tag{2.3}$$

$$j_0 = j_{00} \exp\left[\frac{-\bar{E}_g}{kT} + \frac{\sigma^2}{2(kT)^2}\right] \tag{2.4}$$

Figure 2.5 presents CIGS device efficiencies as a function of bandgap for single junction devices compared to the Shockley-Queisser limit [73]. The highest efficiency devices have a bandgap of $\sim 1.2\,\text{eV}$ corresponding to 30% gallium content, which lines up well with one theoretical maximum for the AM1.5G spectrum. However, as more gallium is incorporated into the sample, increasing the bandgap, the average device efficiency decreases, despite the second theoretical maximum that can be seen at $1.4\,\text{eV}$. The cause of this is largely due to a non-linearity between bandgap and V_{oc}. It is argued that this is due to a change in the band alignment between the CIGS and CdS layers from a 'spike' to a 'cliff' configuration [74]. What is not understood sufficiently however, the absorber itself changes with higher concentrations of gallium and how it affects composition variations at grain boundaries.

There is a lack of consensus within the CIGS community surrounding the cause of the unique grain boundary behavior. This can be partly due to a lack of statistically meaningful data. These data can be obtained with high resolution imaging of composition and local collection efficiency. Very high spatial resolution and sensitivity is needed when grain sizes are $2\,\mu\text{m}$ and smaller. Unfortunately, many of the techniques currently used involve extensive
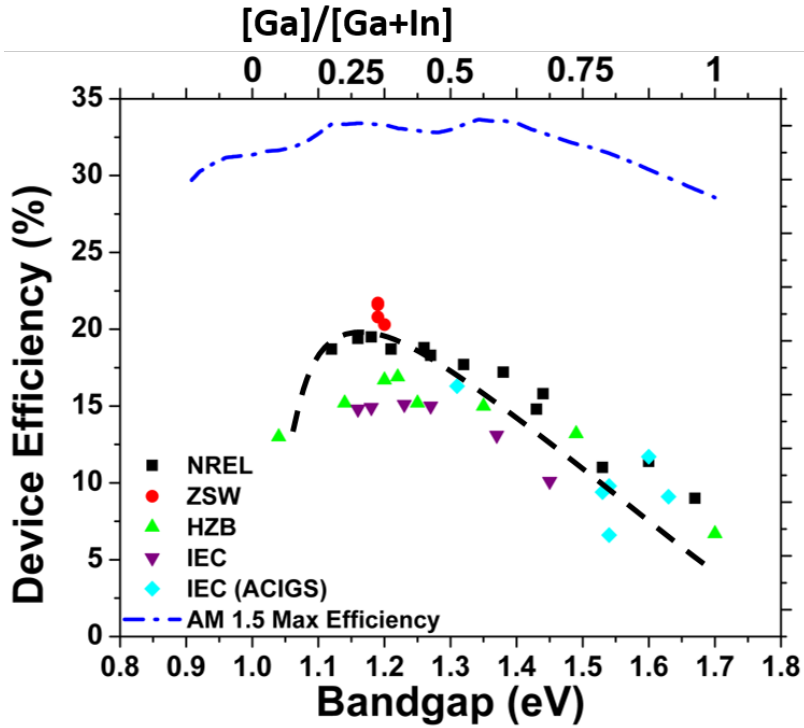
Figure 2.5 CIGS device efficiency as a function of absorber band gap. A curved dashed black line is used to highlight the trend in the scatter plot data. Data taken from NREL [75], ZSW [51], HZB [76], IEC [77], IEC (ACIGS) [78], AM 1.5G Max Efficiency [73]

sample preparation, which makes collecting statistically meaningful data challenging. The following sections outline our approach to this problem and the show potential of synchrotron light sources to characterize thin film solar cells.

2.2 Synchrotron Radiation

Synchrotron based characterization is a promising tool to investigate grain boundaries in thin film solar cells, because of the high spatial resolution, high sensitivity due to the large incident photon flux, and capability to combining multiple techniques to simultaneously measure structural, chemical, electrical, and compositional properties. Synchrotron light sources generate X-rays from particle accelerators called storage rings, mostly using electrons. Photons are tangentially diverted by electrons from the storage ring through an undulator. An undulator consists of a series of stationary magnets with alternating magnetic field to cause the electron beam to oscillate. This change in angular momentum causes high energy photons (X-rays) to be emitted. The X-rays are then focused using optics such as diffraction-based zone-plates or grazing incidence mirrors. Synchrotron light sources are compared in terms of brilliance, which has the units shown in Eq. 2.5. Brilliance that takes into account the photon flux per unit time, the spot size, the beam coherence, and the "monochromaticity" which is measured as the percentage of photons falling within 0.1% bandwidth (beam energy). For X-ray fluorescence, the most important terms are the flux and the spot size.

$$\text{brilliance} = \frac{\text{photons}}{\text{sec} \cdot \text{mrad}^2 \cdot \text{mm}^2 \cdot 0.1\%\text{BW}} \tag{2.5}$$

Third generation synchrotron light sources reviewed here [80], are the most brilliant in the world. Figure 2.6 shows a comparison between the brilliance of US light sources, (Advanced Photon Source (APS) at Argonne National Laboratory, and Advanced Light Source (ALS) at Lawrence Berkeley National Laboratory), with typical Cu Kα sources present in most laboratory X-ray diffractometers (copper Kα / molybdenum Kα). As it can be seen, for energies higher than $10\,\text{keV}$, the APS offers 10 orders of magnitude higher brilliance than laboratory sources.
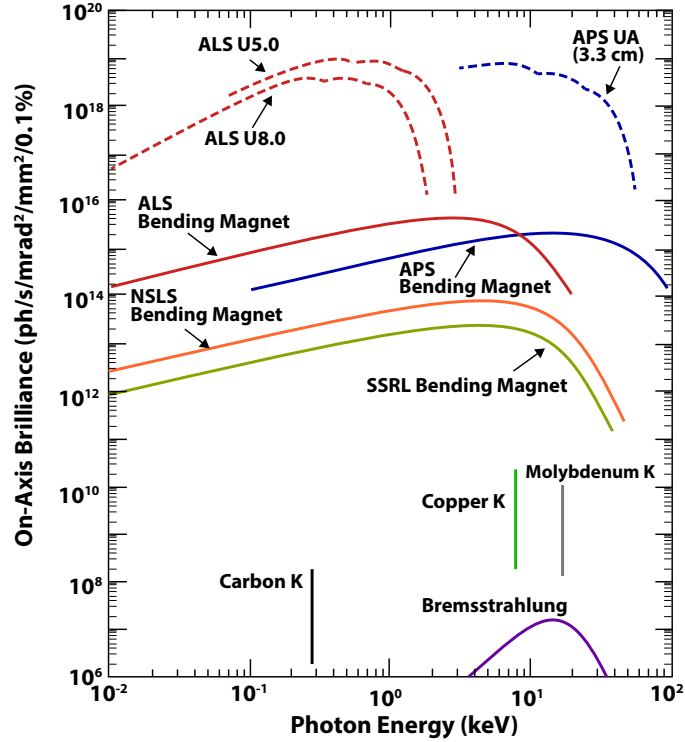
Figure 2.6 Brilliance tuning curves as a function of energy for several synchrotron light sources compared with laboratory X-ray sources such as Carbon K, Copper K, and Molybdenum K radiation. Data from [79]

.

We have utilized the high brilliance of this light source to combine X-ray fluorescence (XRF) and X-ray beam induced current (XBIC) for *in situ* and operando studies of full CIGS solar cells. Prior to 2013, XRF and XBIC were mainly applied to silicon solar cells to investigate dislocations and metal impurities [81–85]. More recently, studies discussed here and published by others have looked at CIGS [86–91], CdTe [92], organic photovoltaics [93], perovskites [94], and GaAs [95] devices. The advent of hard X-ray nanoprobes, like those at APS [96], NSLS-II [97], and ESRF [98], have enabled these studies by achieving spot sizes below 50 nm.

Figure 2.7 shows the setup of APS 2-ID-D. The x-y stage and nano-positioner where the sample is mounted not only facilitates the spot-to-spot correlation between composition
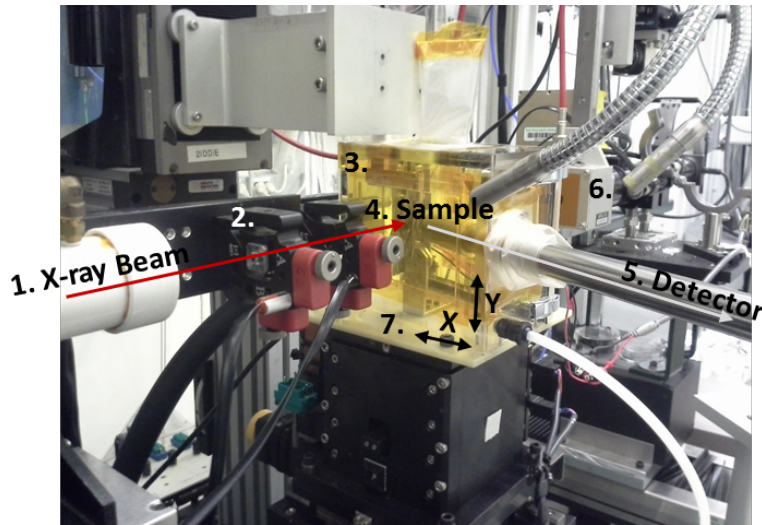
Figure 2.7 Setup of APS beamline 2-ID-D, with the 1.incident X-ray beam, 2. Zone plates (focusing optics) 3. Atmosphere controlled box. 4. Sample, 5. Fluorescence Detector. 6. Down Stream Ion Chamber. 7, X-Y stage.

(XRF) and electrical properties (XBIC), it also provides the advantage of collecting statistically meaningful data. These techniques are non-destructive and are capable of large scan areas ($100\,\mu m^2$) within a few hours with a spatial resolution on the order of $50\,nm$ to $100\,nm$. The high resolution and the short measurement time allows for statistically significant point-by-point correlations, which are huge advantages over many of the techniques currently in use and described in the previous section. A statistical representation will highlight the most prominent effects of grain boundaries in CIGS overall performance and allow for the proper evaluation of defect engineering techniques to enhance devices output. This study is shown in Section 4.

2.2.1   X-ray Fluorescence

XRF is a characterization technique used to determine elemental composition of a material or material system. Incident X-ray photons with energy high enough to overcome the binding

XRF

Photon E_{in}

Energy

E_{vac}
E_c
E_v — $10^0 - 10^1$ eV

$L\alpha$
$K\alpha$

4
3
2 — Core Levels
1 — $10^3 - 10^5$ eV
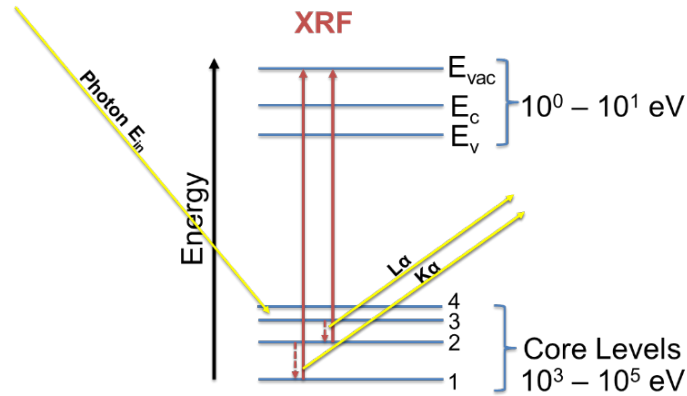
Figure 2.8 Schematic of the XRF process. High energy incident photons excite an electron in a core shell which is then filled by an electron in a higher energy state releasing a secondary photon.

energy of core atomic levels, excite electrons in those levels leaving an unfilled state. Electrons from higher energy levels can fill the newly unoccupied state by releasing energy in the form of a photon. These photons can be collected with an energy dispersive detector; the photon energy is specific to the type of transition and element. This process is shown in Figure 2.8 with Kα and Lα transitions.

The transitions are labeled based on the shell which has available states after X-ray excitation. An electron transitioning from a higher energy level to an empty state in the first energy level corresponds to a K transition, one transitioning to the second energy level is L, etc. Greek letters are used to identify the particular transition that generates the fluorescence by filling the now empty core energy levels. An electron that drops from one state above is α, two states above is β, etc. For example, an electron in the first energy level enters an excited state due to an incident photon of high enough energy to overcome the binding energy, and leaves one state in the first level open. This state is filled by an electron in the second energy level by emitting a photon. This is identified as a Kα transition. An electron transitioning to the first energy level from the third by emitting a photon, is refered to as a Kβ transition. The ratio of the intensity between two transitions is defined as their branching ratio.

22
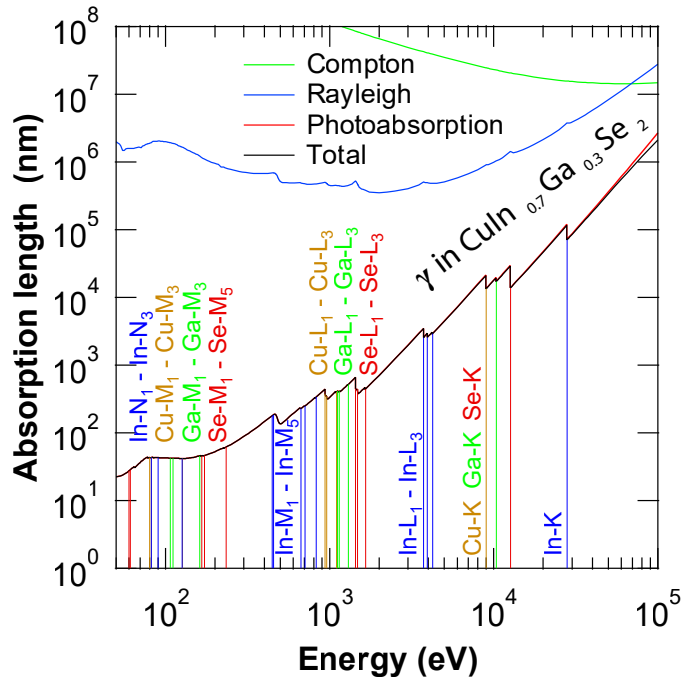
Figure 2.9 Absorption length of X-ray photons at varying energies in an infinitely thick CIGS layer. Contributions from Compton, Rayleigh, and Photoabsorption are shown.

The energy of each transition is intrinsic to the element, thus XRF can be used as a good technique to fingerprint the elemental constituents of a compound. The intensity of fluorescent photons for each transition depends predominately on the concentration of the element in the sample and the incident beam energy. An incident beam energy close to the binding energy of the K or L shell of an element will have a higher excitation probability due to the higher capture cross section, which is related to the absorption coefficient. This can be seen in Fig. 2.9 where the absorption length of photons, with energies just above an absorption edge in the material is lower than photons with energies below the same edge.

Figure 2.9 shows the absorption length of varying X-ray photon energies, in an infinitely thick CIGS film with 30% gallium incorporation. The total absorption length is the sum of the primary interaction mechanisms of X-rays with matter, Compton scattering (green), Rayleigh scattering (blue), and photoabsorption (red). It can be seen that photoabsorption is the dominant

mechanism defining the absorption length. The vertical lines mark the K, L and M absorption edges Cu, In, Ga, and Se.

2.2.2 X-ray beam induced current vs. electron beam induced current

In XBIC, incident X-rays create photoexcited electrons similar to the process described for XRF. However instead of using a photodetector to collect fluorescent photons, electrical contact is made to measure the current generated from the secondary photogenerated electrons. XBIC is similar to other beam induced current methods like EBIC or laser beam induced current (LBIC), wherein an incident particle beam with energy higher than the bandgap of the semiconductor is used to generate electron hole pairs (ehp) within the material. The ehp can be separated and collected in the presence of an internal electric field (p-n junction) or by applying an external bias. By scanning the beam across the sample surface, a 2D map is generated, storing a current value at each pixel, which can be used to determine areas of high/low recombination in the device.

There are some key differences between XBIC and other beam induced current methods. While LBIC and XBIC both use incident photons, the incident photon energy in LBIC is just above the bandgap energy, therefore, each incident photon can be considered to generate one ehp. In contrast, XBIC uses incident photons with energies that are several orders of magnitude above the bandgap, resulting in the generation of many ehp per incident photon. This can make the quantification of the XBIC signal significantly more challenging.

EBIC utilizes an electron beam as the excitation source, which is similar in energy range to XBIC, however primary electrons undergo many more scattering processes compared to incident photons, limiting the penetration depth for equivalent excitation energies. Figure 2.10(a) compares the penetration depth of incident photons (γ) and electrons (e^-) for a given

24
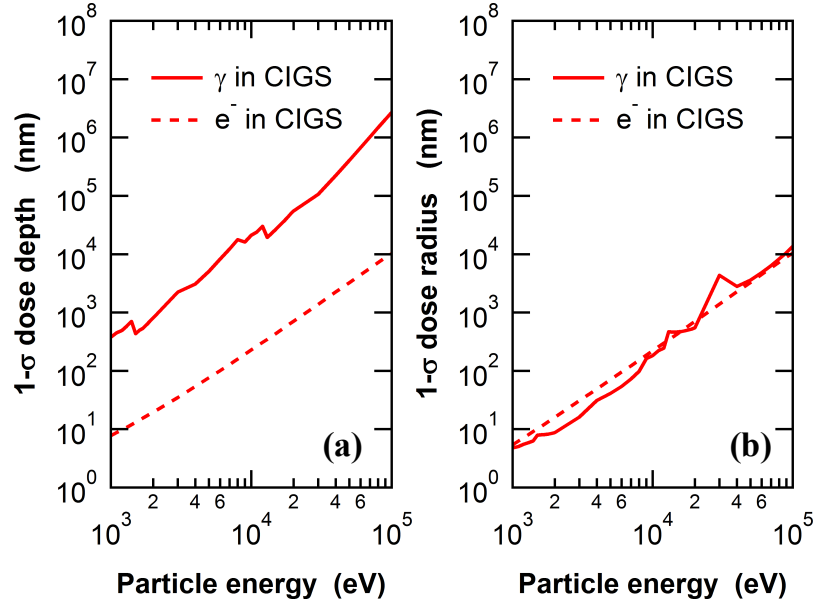
Figure 2.10 Interaction radius vs probe depth for X-ray beam vs electron beam in CIGS

particle energy. The data in this plot is the result of Monte Carlo simulations conducted in PyPenelope [99], based on 10^8 incident particles. The 1-σ dose depth refers to the maximum depth achieved by 68% of the deposited energy dose. It can be seen that at $10\,\mathrm{keV}$ the penetration depth of photons is approximately 2 orders of magnitude greater than for incident electrons. This indicates that XBIC measurements are more sensitive to bulk properties where as EBIC is more sensitive to the emitter (for similar incident energies).

While the probe depth of photons is greater than those of incident electrons, it is interesting to note that the radius of the excitation is comparable between photons and electrons. This is shown in Fig. 2.10(b). Once a photon is absorbed and a photo-electron is generated, it undergoes the same scattering processes as the electrons from EBIC. It should be noted however, that in order to achieve the same penetration depth as X-rays, the incident electron beam requires much greater energy, which would also result in a larger probe radius.

While EBIC measurements are capable of achieving smaller spot sizes ($\sim 1\,\mathrm{nm}$) compared to XBIC ($> 10\,\mathrm{nm}$) and LBIC ($> 1\,\mathrm{\mu m}$), the resolution of these electrical measurements is a

combination of the spot size, excitation volume and the diffusion length of the excited carriers. For a material system with a diffusion length on the order of a few μm, a spot size of ∼ 1 nm does not provide much benefit, because the carriers that thermalize at the band edges will be able to interact with defects several μm away from the spot. This is in addition to the scattering processes that take place, which also expand the excitation volume. This is extremely important to consider when conducting any beam induced current characterization.

2.2.3 Measuring X-ray Beam Induced Current

It is also important to note the difference between XBIC and total electron yield (TEY) measurements, also conducted at synchrotron light sources. While both measure a current induced by X-rays, TEY measures the replacement current associated with electrons leaving the sample surface, in order to maintain charge neutrality. In this case the current is measured between the sample surface and the chamber wall causing the measurement to be highly surface sensitive. XBIC measures the current induced by the excess carriers by making contact to the p and n terminal of the device. Because electrons can still be ejected from the sample surface, the method of sample grounding is important to consider for accurate XBIC measurements.

Figure 2.11 shows different grounding schemes for XBIC measurements. For all the samples described in this dissertation, a majority of the electrons leaving the sample exit from the side exposed to the incident beam. Because of this effect, this is the side that should be grounded and is shown in Fig. 2.11(a,c). It can be seen in Fig. 2.11(b,d) that if the back of the device is grounded, the XBIC signal is reduced by the current of the electrons exiting the surface. The situation becomes less clear if measuring the sample in cross section (Fig. 2.11(e)), and has not been studied experimentally, but it is probably wise to ground the terminal matching the majority carrier in the absorber layer.

26
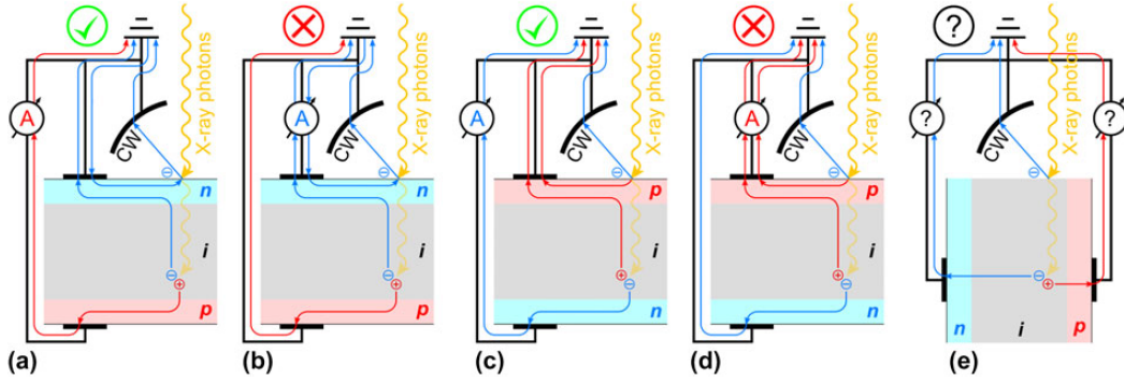
Figure 2.11 Different grounding schemes for X-ray beam induced current (XBIC) measurements showing the benefit of grounding the front of the sample compared to the back, independent of carrier type.
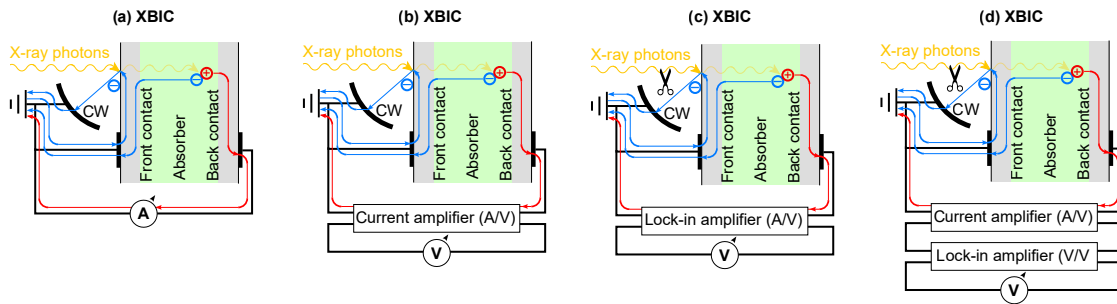
Figure 2.12 Electrical setup for X-ray beam induced current (XBIC) for different amplification configurations discussed in the text and The abbreviation "CW" stands for Chamber Wall.

In addition to the grounding scheme utilized, the method for signal amplification must also be addressed. Four different amplification configurations are shown in Fig. 2.12. Typical XBIC measurements utilize the configuration presented in Fig. 2.12(b), and at APS 2-ID-D and APS 26-ID-C the current amplifier used is a Stanford Research Preamplifier SR 570. Across both APS beamlines the voltage-frequency converters are used for data acquisition, with conversion of 10^5 cts/V. The use of a current amplifier improves the signal to noise compared to the setup shown in Fig. 2.12(a), and applies a conversion of A/V described further in Sec. 2.2.4.

If XBIC is being measured with voltage or light bias, to be representative of device operating conditions, a lock-in amplifier is necessary to measure the induced current from the X-ray beam above the current from the light/electrical bias. Lock-in amplifiers chop the input signal at a given frequency and measures the difference between the off and on signals. The relative benefits of each amplification configurations in terms of the signal to noise ratio, and ability to measure devices under bias are shown in Table 2.2.

The lock-in amplifier used for these tests is the MFLI from Zurich Instruments. The X-ray beam was chopped at a frequency of $318\,\text{Hz}$ using a MC1F10 filter wheel from Thorlabs with an ON/OFF transmittance ratio of $> 10^{12}$ for a photon energy of $10.5\,\text{keV}$. When selecting the frequency of the chopper it was important to ensure that it is not within the range of other frequencies in the environment (ie: grid frequency $= 60\,\text{Hz}$, synchrotron frequency $= 100\,\text{kHz}$). The chopper was place upstream of the zone plates, labeled as 2 in Fig. 2.7.

Table 2.2 Comparison of signal amplification configurations shown in Fig. 2.12 for XBIC measurements, with respect to their signal-to-noise and bias support.

Setup	Lock-in/DC	Signal-to-noise	Bias Support
Fig. 2.12(a)	DC	$--$	$--$
Fig. 2.12(b)	DC	$-$	$--$
Fig. 2.12(c)	Lock-in	$+$	$++$
Fig. 2.12(d)	Lock-in	$++$	$++$

2.2.4   Quantifying X-ray Beam Induced Current

Raw XBIC data stored in the MAPS software package developed at APS is saved as counts. The first step to quantifying the XBIC data is converting the raw counts to a current, by dividing by the voltage to frequency converter scalar (at APS 10^5 cts/V) and multiplying by the amplifier sensitivity (A/V). While the current of the solar cell is of interest, a more meaningful parameter

used widely throughout the photovoltaics community is the collection efficiency (CE), that is defined as the ratio of collected charge carriers $N^{\text{coll}}_{e^-/h^+}$ to the generated charge carriers $N^{\text{gen}}_{e^-/h^+}$:

$$\text{CE} := \frac{N^{\text{coll}}_{e^-/h^+}}{N^{\text{gen}}_{e^-/h^+}} \tag{2.6}$$

Collection efficiency for solar cells exposed to visible light (VIS) is measured based on the external quantum efficiency (EQE) and internal quantum efficiency (IQE), shown in Eq. 2.7.

$$\text{EQE} := \frac{N^{\text{coll}}_{e^-/h^+}}{N^{\text{in}}_{\text{ph}}} \text{ and } \text{IQE} := \frac{N^{\text{coll}}_{e^-/h^+}}{N^{\text{abs}}_{\text{ph}}} \tag{2.7}$$

The main difference between these parameters is the reference number of photons. For EQE, the number of collected carriers ($N^{\text{coll}}_{e^-/h^+}$) is divided by the total number of photons incident on the sample ($N^{\text{in}}_{\text{ph}}$), where as IQE is referenced to the number of photons absorbed ($N^{\text{abs}}_{\text{ph}}$). For incident photons in the visible range (like those in LBIC) the number of photons generated is approximately equal to the number of photons absorbed (ie: one photon generates one electron hole pair), show in Eq. 2.8

$$N^{\text{gen}}_{e^-/h^+} \overset{\text{VIS}}{\approx} N^{\text{abs}}_{\text{ph}} \tag{2.8}$$

This approximation does not hold for incident X-ray photons because the high energy photons result in an electron shower, such that one absorbed X-ray photon can generate several thousand electron hole pairs. Estimating the number of electrons generated, however, is not trivial, and depends on multiple variables including: bandgap, incident photon flux, the probability of secondary scattering/excitation events, and the number of photons absorbed within the absorber layer. These factors are accounted for in the term C in equation 2.9.

$$\text{XCE} := \frac{N^{\text{coll}}_{e^-/h^+}}{N^{\text{gen}}_{e^-/h^+}} \overset{\text{X-ray}}{=} \frac{N^{\text{coll}}_{e^-/h^+}}{C \cdot N_{\text{inph}}} \tag{2.9}$$

The correction factor can be approximated by $C \approx A \cdot B$, where A is the fraction of absorbed photons and B is the number of generated electron-hole pairs per absorbed X-ray photon. For a qualitative analysis the XBIC signal can be normalized to the incident photon flux, maybe viewed as XCE as long as C remains constant. This is the case for solar cell devices with low variations in thickness, like silicon solar cells (ignoring the metallization). This however is not true for thin film solar cells like CIGS where C is strongly dependent on the layer thickness.
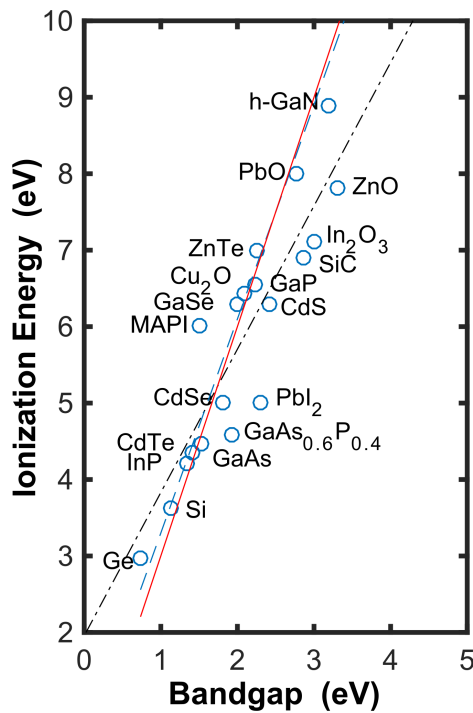
Figure 2.13 Ionization energy E_{ion} compared to the band gap E_g for a variety of semiconductors. The values are from Ref. [100] (Ge, Si, GaAs, CdTe, GaP, CdS, PbO, SiC), Ref. [101] (Cu_2O, In_2O_3, ZnO), Ref. [102] (PbI_2, GaSe, ZnTe, CdSe), Ref. [103] (MAPI), Ref. [104] (ionization energy of h-GaN), Ref. [105] (ionization energy of InP), Ref. [106] (ionization energy of GaAsP), Ref. [107] (band gap of InP, GaN), and Ref. [108] (band gap of GaAsP). The dashed blue line follows $E_{ion} = \frac{14}{5} * E_g + 0.5eV$ as suggested in Ref. [109]. The solid red line follows $E_{ion} = 3 * E_g$. The dashed/dotted black line is a linear fit, following $E_{ion} = 1.875 * E_g + 1.956eV$.

A can be determined by measuring the incident photon flux, with either a calibrated p-i-

n diode or an ion chamber, and using Beer-Lambert's law to calculate the number of photons absorbed in the absorber layer. For multi-layered structures (described in more detail in Chapter 3) the photons absorbed in layers upstream from the absorber layer need to be taken into account as well. B can be estimated based on the ionization energy of the material. The ionization energy is the minimum energy required to eject an electron from the material. By dividing the incident photon energy by the ionization energy of the material, the maximum number of electron-hole pairs per incident photon is estimated. The ionization energy of a material is dependent upon its bandgap, which is shown in Fig. 2.13. For material systems like CIGS with a non-uniform bandgap in x-y, B should be calculated on a pixel by pixel basis.

2.2.5   X-ray Beam Induced Voltage

For a complete representation of the solar cell behavior and a fundamental understanding of the electrostatic potential fluctuations [70, 72], we need to be able to measure the voltage of a device under operation. This prompted the development and implementation of X-ray beam induced voltage (XBIV) [110]. Figure 2.14 shows a hexbin plot of XBIV vs XBIC, collected on the same spot of a CIGS solar cell measured under bias. The electrical measurements are in uncorrected units of μV and nA. The linear trend between current and voltage is indicated by the dashed white line. This highlights the sensitivity of each technique to recombination, where regions resulting in poor voltage also have poor current collection. Another interesting feature is the bright feature in the top right corner of the map. This shows that most of the pixels in the map are high performing (note the log color scale) in both current and voltage. The magnitude of the current and voltage is likely limited by the poorer performing regions marked by the green triangle.

The green lines are representative of a qualitative dependence of both current and voltage,
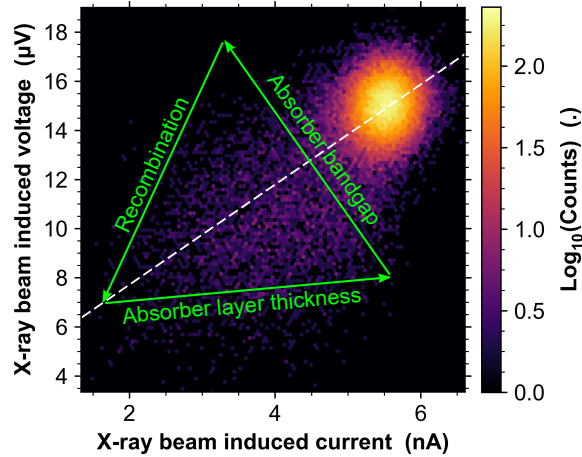
Figure 2.14 Hexbin plot of the pixel-by-pixel correlation of the XBIV measurement with the XBIC measurement at $300\,\mathrm{mV}$ forward bias. The green lines indicate the qualitative dependence of XBIC and XBIV on recombination, absorber bandgap, and absorber thickness.

on absorber layer thickness, bandgap of the absorber layer, and carrier recombination. As mentioned previously the XBIC signal is highly dependent on the number of photons absorbed, with a large part attributed to variations in absorber layer thickness (more material = more current). XBIV is much less dependent on these small thickness variations. Both XBIV and XBIC are dependent on variations in absorber bandgap. XBIC is dependent through the ionization energy of the material, where an increase in bandgap causes a decrease in number of electron hole pairs generate. XBIV on the other hand is positively correlated with the bandgap where an increase in bandgap leads to an increased V_{oc}, shown in Equations 2.3 and 2.4. Lastly, XBIV is more sensitive to carrier recombination than XBIC due to the logarithmic dependence on the recombination current.

There are inherent benefits associated with measuring voltage compared to current. As described previously, and shown in Figure 2.14, XBIV is much less sensitive to thickness variations. Quantifying XBIC measurements, requires corrections for the number of photons absorbed based on the composition and film thickness. This is described in detail in Chapter 3. These corrections require assumptions about overall film uniformity, thickness, and

surface roughness. These assumption introduce additional uncertainty into the measurement. Measuring XBIV does not require the same assumptions be made, allowing one to interpret the raw voltage data.

However, measuring XBIV under bias and with lock-in amplification, poses a unique challenge. Figure 2.15(a) shows qualitatively the linear dependence of current on photon intensity for a high performing cell (red), vs a poor performing cell (black). Under low illumination (or no light bias) the difference between beam 'ON' and beam 'OFF' is shown in the bottom left corner by the shaded boxes by ΔX_{dark}. It can be seen that for the same change in injection level the increased current ΔI of the high performing cell is greater than the poor performing cell ($\Delta I^{good} > \Delta I^{poor}$). The same is observed with increased photon intensity (with light bias), for a fixed ΔX the increase in current of the high performing cell is greater than the poor performing cell. This is to be expected, and is due to the linear relationship between current and photon intensity.

The same conclusions can not be made when measuring the cell voltage under light bias, due to the logarithmic dependence of voltage on photon intensity, shown in Fig 2.15(b). With no light bias, and a change in incident photon intensity of ΔX_{dark}, it can be seen that $\Delta V^{good} > \Delta V^{poor}$. This is true to the left of the 'shoulder' in the logarithm where voltage has a strong dependence on photon intensity. However, this is not necessarily true when the cell is under light bias, where the voltage is less sensitive to changes in photon intensity. In this situation, ΔV alone can not be used to predict 'good' and 'poor' regions.

Addressing these challenges is currently ongoing work in the group. Combining XBIC and XBIV measurements on the same spot for a pixel-by-pixel correlation could help identify 'good' and 'poor' regions relatively, however this is not the focus of this work. Here the focus is on establishing the framework for measurements of XBIC and growth kinetics.
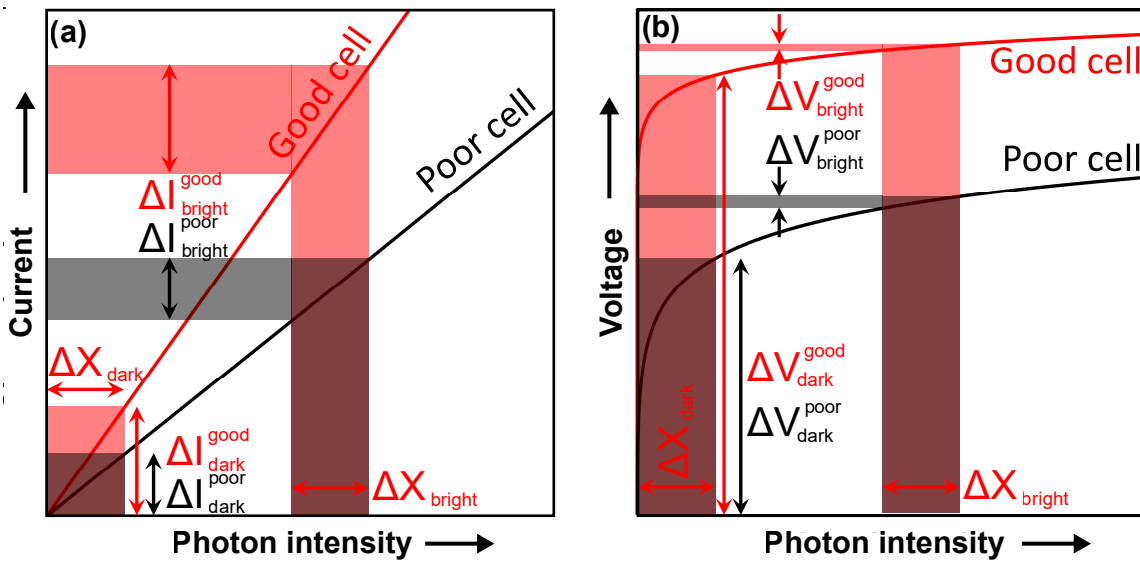
Figure 2.15 In experiments with lock-in amplification, the proportionality between current and photon intensity in (a) leads to a higher response of a good cell than of a poor cell $\Delta I^{good} > \Delta I^{poor}$, independent of the absolute photon intensity. In contrast, the logarithmic relationship between voltage and photon intensity in (b) does not allow for a prediction whether the good or poor cell provides a higher response ΔV.

Chapter 3

X-RAY FLUORESCENCE ON MULTI-LAYERED STRUCTURES

Common applications of XRF microscopy involve the use of hard x-rays to detect small quantities or even traces of an element in a low absorption matrix (typically Si or organic materials) [81, 85, 111, 112]. Obtaining accurate quantification of XRF data becomes more challenging, when measuring of thin films solar cells (with a thickness on the order of a few micrometers) that consist of heavier elements, including:

1. Layers of interest buried within a complex stack of several layers, including substrates, that all can contain XRF-active elements. How do you distinguish fluorescence from different layers?

2. Quantifying minor composition fluctuations, if the elements of interest are the majority components, not traces in an x-ray transparent matrix, and the constituent layer has significant thickness variations

While, the physics governing these challenges have been described in detail [113–115], and some aspects have already been implemented in X-ray data analysis packages [116–118], it is still important for us to address the practical implementation of these analyses towards high resolution microscopy of real material systems, like thin film solar cells. In the following sections we describe the derivation of the formula used to correct the XRF data. We address sources of error associated with correcting data for materials with thickness variations, and depth dependent composition variations. We also show the potential for misinterpretation if these factors are not properly addressed.

3.1   Fitting Raw Data and Thickness Correction

Figure 3.1 depicts the data processing procedure from raw data to corrected XRF maps. Maps are collected, by scanning the sample in X and Y directions, and a full energy spectrum is collected for each measurement spot (Fig. 3.1a). Isolating the peak associated with a particular element shows the x-y distribution of that element in units of counts (see Fig. 3.1b). Prior to correcting the data for absorption losses, the XRF spectra are fitted for the quantification of different elements (Fig. 3.1c). To ensure an accurate fit, branching ratios (described in section 2.2.1) need to be well defined. Branching ratios of X-ray fluorescence from K-lines are tabulated in literature and well-studied [119], however L-line branching ratios tend to vary as a function of excitation energy [120]. Therefore, it may be necessary to measure L-edge branching ratios for a specific experiment. From the fit, the intensities of the peaks are isolated and compared with the intensities of a well-quantified standard that is measured under the exact same geometry as the sample [121]. Applying a calibration curve to the elements of known concentration in the standard gives access by interpolation/extrapolation to the relative XRF signal of different elements that are not contained in the standard but may be in the sample. The data are processed in this fashion, pixel by pixel in each map collected, resulting in elemental maps in units of weight per area (Fig. 3.1d). To accurately quantify the elemental composition of a sample with multiple layers of materials with non-negligible absorption coefficients, the data should be corrected for attenuation (Fig. 3.1e). If the sample is not perfectly flat, surface topology has an impact on the data collected. In our case, we are interested in compositional variations, which need to be separated from thickness variations for accurate data interpretation. To account for thickness variations, mass based concentrations can be converted to atomic percentages by dividing an elemental distribution map by the density weighted sum of all elements in the layer of interest, pixel by pixel, isolating

36

a) Single XRF Spectrum

b) Raw XRF Map

c) Fit XRF Spectrum

d) Quantified XRF Map

e) Absorption Correction

f) Thickness Correction
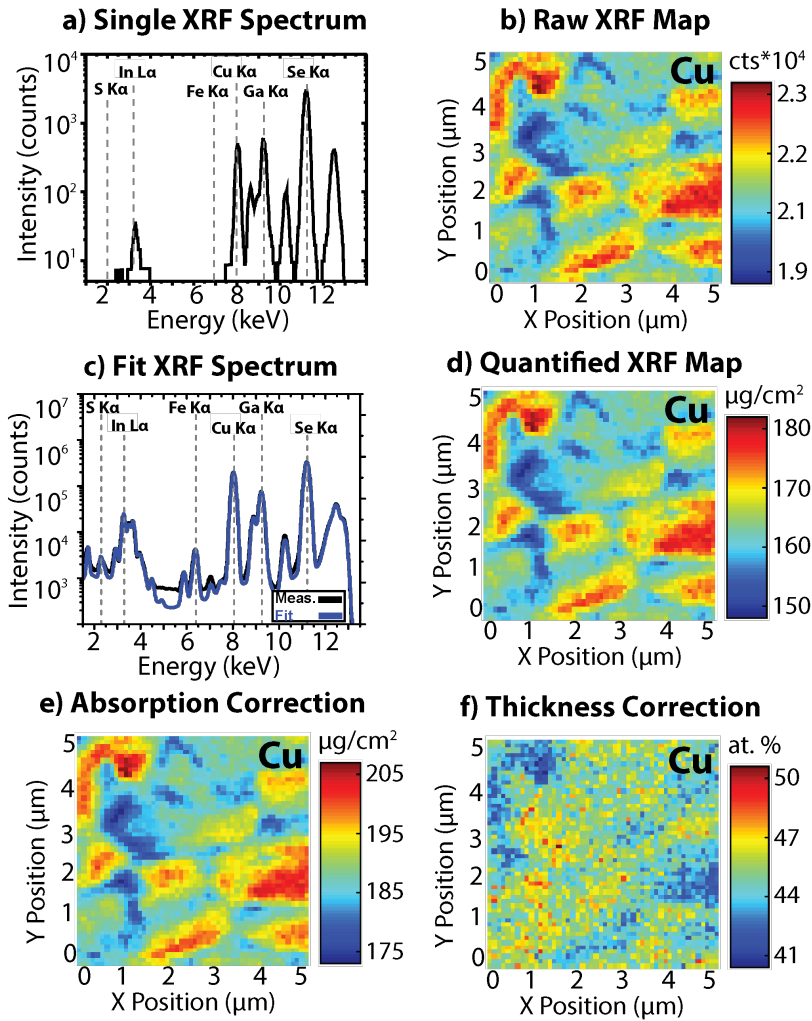
Figure 3.1 Diagram showing the evolution of a copper map in a CIGS solar cell while following the steps described above as the procedure to quantify the elemental distribution from X-ray fluorescence measurements. Starting with the single spectra found in each pixel (a), going to the 2-D unfitted XRF map (b), a fit of each pixel (integrated spectrum shown) (c), and proceeding through quantification (d), absorption correction (e) and thickness correction (f).

changes in stoichiometry (Fig. 3.1f). An alternative approach could involve measuring the thickness variations directly (e.g. by atomic force microscopy), and conducting XRF on the same area or combining XRF scans with tomographic information [122].

3.2   Correcting for Attenuation Losses

Beer-Lambert's law [123], shown in Eq. 3.1, describes the intensity decay of light in matter.

$$\frac{I}{I_0} = e^{-\mu L} \tag{3.1}$$

I/I_0 represents the fractional intensity of transmitted light, μ is the attenuation coefficient in cm^{-1}, and L (cm) is the path length of the light in the material. The attenuation coefficient is the product of the density ρ (g/cm^3) and the capture cross-section σ (cm^2/g). For many material systems, μ is well known and tabulated. However, for systems where μ is not well characterized, it can be calculated from capture cross-section databases available for most elements through the National Institute of Standards and Technology [124] and by using a sample-specific material density. Beer-Lambert's law in its current form is useful for describing the intensity decay of visible light or X-rays propagating through a single uniform medium to a certain depth or thickness. To account for other samples structures, and inhomogoenous materials, it should be expanded to account for: multiple layers, such as stacks used in thin film solar cells, depth-dependent composition variations, attenuation of both the incident beam and generated fluorescent photons, and average attenuation as fluorescence occurs continuously throughout the sample thickness. The following formulation is intended to serve as an experimental approach to correct for attenuation and self-absorption of the exciting photons and photons at a fixed fluorescence energy, which can be repeated and applied to each element of interest. Note that an accurate representation of the attenuation of all fluorescence generated within the layer stack will require a more complete formalism that accounts for the probability for fluorescence to occur, secondary fluorescence effects, and a three dimensional model that account for the 4π generation of fluorescence. Figure 3.2 depicts these effects in a multicomponent layered structure. The incident X-ray beam, hitting the sample surface

38
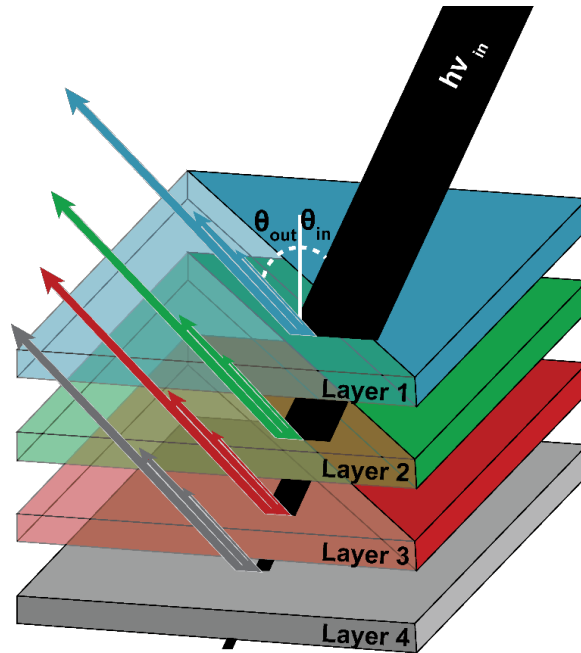
Figure 3.2 Diagram showing the propagation and attenuation of high energy photons entering the sample stack and fluorescent photons exiting towards the detector. Each multicomponent layer generates photons of different energies that have different attenuation coefficients in each layer. The multicomponent nature of each layer is represented with multiple arrows exiting each layer.

under the angle θ_{in}, shown in black, is attenuated through each layer of the stack. The multiple arrows exiting each layer represent the fluorescent photons with varied energies that are also attenuated as they exit the stack. The increased attenuation throughout the thickness leads to increased XRF signal from the sample surface, and decreased signal from the bulk and back of the sample. While the fluorescence process is isotropic, we only need to consider those photons that are emitted under the angle θ_{out} such that they can reach the fluorescence detector. These two angles impact the beam path length and ultimately the measured fluorescence intensity.

To account for multiple layers, and depth dependent composition variations, μ is no longer constant along the light path L. The light path can be divided into small sublayers of length (Δl) over which μ can be assumed constant. The product of Eq. 3.1 over each of these sublayers

is the total intensity decay, and the exponent can be treated as a summation shown in Eq. 3.2, where N is the total number of layers in the structure and $\mu(l_i)$ is the attenuation coefficient at length l_i.

$$\frac{I}{I_0} = e^{-\mu L} = e^{-\mu_1 \Delta l} \cdot e^{-\mu_2 \Delta l} \dots = \exp\left[\sum_{i=1}^{N} -\mu(l_i)\Delta l\right] \tag{3.2}$$

By taking the limit of the summation as N approaches infinity, the expression can be re-written as a definite integral from the top of the layer stack (0), where the incident beam hits the sample, to the total light path length. This is shown in Eq. 3.3.

$$\frac{I}{I_0} = \exp\left[\lim_{N\to\infty}\sum_{i=1}^{N} -\mu(l_i)\Delta l\right] = \exp\left[\int_0^L -\mu(l)dl\right] \tag{3.3}$$

Equation 3.3 describes only the incident light path. The exiting fluorescence is attenuated in a similar way. The measurement geometry and thickness of the sample impacts the length of both light paths, and is accounted for in Eq. 3.4 in terms of the sample thickness. We introduced the terms $L = T/\cos(\theta_{\text{in}})$ for the incident beam and $L = T/\cos(\theta_{\text{out}})$ for the exiting beam to treat the light path in terms of thickness and measurement geometry.

$$\frac{I_t}{I_0} = \exp\left[\int_0^{T/\cos\theta_{\text{in}}} -\mu_{\text{in}}(t)dt + \int_0^{T/\cos\theta_{\text{in}}} -\mu_{\text{out}}(t)dt\right] \tag{3.4}$$

This equation describes the intensity decay from the incident beam (μ_{in}) and generated fluorescence of a particular element of interest (μ_{out}) at a given depth t, and sample thickness T, as the ratio of the intensities of the specified elemental fluorescence (I_t) and the incident beam intensity (I_0). It should be noted that this equation just describes the attenuation of the X-rays, and the probability of fluorescence to occur is taken into account during the fitting and quantification of the spectrum. Effects such as secondary fluorescence are not included and assumed to be negligible for the purpose of this analysis. For a detailed discussion on how to take into account secondary fluorescence when necessary, refer to [41]. As mentioned

previously, the detector measures the number and energy of photons collected, and photons generated from different sample depths are treated equally. Because, fluorescence occurs continuously throughout the sample thickness, the average attenuation caused by the stack needs to be calculated. This is shown in Eq. 3.5.

$$\frac{I}{I_0} = \frac{1}{T} \int_0^T \frac{I_t}{I_0} dt'$$

$$= \frac{1}{T} \int_0^T \exp\left[\int_0^{T'/\cos\theta_{in}} -\mu_{in}(t)dt + \int_0^{T'/\cos\theta_{in}} -\mu_{out}(t)dt \right] dT'$$

(3.5)

The resulting value I/I_0 is a value between 0 and 1 representing the average intensity decrease of detected fluorescence compared to the incident beam intensity. While mathematically accurate, this equation is in general not analytically solvable due to the depth-dependence of μ_{in} and μ_{out}. It can be simplified by assuming a finite layer thickness (Δt) over which $\mu(t)$ can be assumed constant. This is shown in Eq. 3.6. Once the losses are calculated for each of the elements of interest, every pixel value in the XRF map is then divided by I/I_0, to correct for the losses described in this section. Additionally, I/I_0 in the final formulation presented here should be considered an as an effective correction factor taking into account attenuation of exciting and fluorescent radiation through capping layers, as well as self-attenuation within a layer of interest. It should be noted again, that this analysis assumes a radiation-free attenuation of generated XRF photons. These secondary effects are assumed negligible in the following case, although can have an impact.

$$\frac{I}{I_0} = \frac{1}{T} \sum_{i=1}^T \exp\left[\sum_{i=1}^N \left[\frac{-\mu_{in}(t_i)}{\cos(\theta_{in})} \Delta t_i + \frac{-\mu_{out}(t_i)}{\cos(\theta_{out})} \Delta t_i \right] \right]$$

(3.6)

3.2.1 Setup for Experimental Validation

The process described in section 3.2 was tested on a CIGS solar cell measured at two different beam lines (2-ID-D [125] and 26-ID-C [96]) at APS at Argonne National Laboratory. The measurement parameters are described in Table 3.1.

Table 3.1 Measurement geometries and beam information for two separate beamlines at APS used to measure XRF on CIGS solar cells

Beamline	Beam Energy	Beam Angle (θ_{in})	Detector Angle (θ_{out})	Spot Size
APS 2-ID-D	10.4 keV	0°	77°	185 nm
APS 26-ID-C	10.4 keV	15°	75°	50 nm

The device structure is similar to that shown in Figure 3.2. Layer 1 corresponds to intrinsic ZnO and ZnO:Al (150 nm), Layer 2 is CdS (50 nm), Layer 3 is CIGS with a Ga/(Ga+In) ratio of 0.3 (1.6 m), and Layer 4 is Mo (700 nm) deposited on a soda lime glass substrate. A more detailed discussion of sample preparation and device structure conducted at the National Renewable Energy Laboratory (NREL) can be found in [22]. This device exhibits a typical "V" shaped grading through the CIGS layer with high gallium content at the front and back and lower in the middle, described previously. As reference, an AXO thin film standard was used, containing the elements and concentrations shown in Table 3.2. The substrate is silicon nitride.

The data was quantified and fitted using MAPS software developed at APS [126, 127]. Fluorescence was detected by a Vortex-ME4, four-element energy dispersive silicon drift detector at beamline 26-ID-C, a Vortex-EM/ASIC single element energy dispersive silicon drift detector at 2-ID-D.

Table 3.2 Concentration of elements in AXO standard [121]

Element	Concentration $(\mathrm{ng/mm^2})$
Pb	7.6 ± 0.8
La	11.7 ± 1.8
Pd	1.5 ± 0.3
Mo	0.8 ± 0.2
Cu	2.0 ± 0.6
Fe	3.9 ± 0.4
Si	substrate

3.2.2   Results

Figure 11 shows typical XRF maps collected at APS 2-ID-D. Uncorrected data refer to the XRF data not treated for absorption losses, depth dependent composition variations, or thickness variations, and corrected data refers to the data after correcting for these factors. The maps are $5\,\mathrm{\mu m} \times 5\,\mathrm{\mu m}$ with $100\,\mathrm{nm} \times 100\,\mathrm{nm}$ pixel size, taken with 1 second dwell time. Selenium (Se K edge = $12.66\,\mathrm{keV}$) was not collected during this run, to enhance sensitivity to the cations, Cu, Ga, and In. After correcting for thickness variations, attenuation losses, and depth dependent composition grading, the maps look quite different. The top left corner appears to have the highest concentration of all copper, gallium, and indium, across the map. However, after thickness correction, described previously, it can be seen that that region is actually copper and gallium poor, and indium rich. This highlights that the concentration variations observed in the uncorrected map are largely due to thickness variations because the compositional inhomogeneity of the sample is smaller in magnitude than variations due to surface roughness. This leads to a significantly different interpretation of the XRF data than would have resulted using uncorrected maps. It should be noted that the thickness corrected XRF maps appear much noisier than the uncorrected images. This is mainly due to the noise
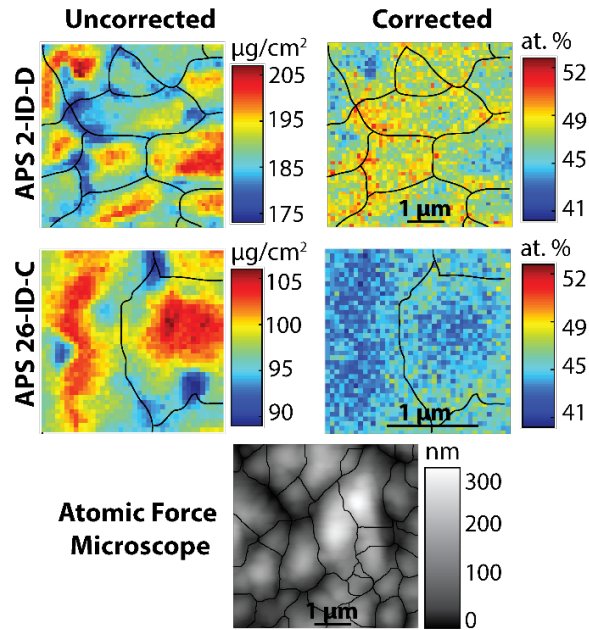
Figure 3.3 Copper X-ray Fluorescence maps of the same CIGS sample, taken at two beamlines with different geometries and beam intensity. Atomic force microscopy map with delineated grain boundaries presents a comparison to the grain sizes obtained using the watershed technique. Note: measurements are not on the same area.

associated with the indium channel. The incident beam energy of $10.4\,\mathrm{keV}$ is much higher than the indium L_1 edge ($4.34\,\mathrm{keV}$), leading to decreased sensitivity to variations in indium.

Figure 3.3 shows XRF maps for a CIGS device measured at two different APS beam lines. The uncorrected maps show the fitted quantified data in $\mu\mathrm{g/cm^2}$. The large difference in the quantification of uncorrected maps should be noted. For example, the measurement taken at 2-ID-D shows a maximum copper concentration of $205\,\mu\mathrm{g/cm^2}$, whereas the measurement taken at 26-ID-C shows a maximum of $105\,\mu\mathrm{g/cm^2}$. After application of the corrections to account for the different attenuation losses between the two geometries and normalized for thickness, the concentration measured in atomic percent shows better agreement between the two beamlines. The remaining 4 % difference between the average atomic percentages of copper for the two maps can be attributed to the inhomogeneities in the sample and standards

used to quantify the raw XRF data. It should also be noted that two different standards were used to quantify these data sets.

The black lines on the images depict the position of the grain boundaries and are the result of image processing by flooding watershed [128]. This technique has been successfully applied to particle segmentation in X-ray tomography and is well-established to separate grains [129,130]. We have also verified its accuracy by comparing AFM and SEM images on the same area measured by XRF, this is described in the following chapter. A comparison of the AFM and XRF images in Figure 3.3, taken on the same sample, reveals similar grain sizes ($1\,\mu$m to $2\,\mu$m) and shapes, suggesting that the flooding watershed technique is an appropriate method to identify grain boundaries in our case, and it confirms that we are not limited by beam spot size for grain identification.

3.2.3 Sensitivity Analysis

Potential sources of error and uncertainty should be taken into consideration when calculating correction factors for non-ideal samples using this method. To determine the impact of uncertainty in the grading profile, I/I_0 was calculated for Cu Kα, Ga Kα, In Lα1, and Se Kα fluorescence as a function of CIGS layer thickness for five different simulated [Ga]/[Ga+In] grading profiles,. These values were calculated using the device structure described previously, with a beam energy of $10.4\,$keV and sample/detector geometry used at 26-ID-C (see table 3.1). It should be noted that the following results describe not only the attenuation from ZnO and CdS layers but self-attenuation in the CIGS layer as well. The thickness variations shown are only for the CIGS layer, and the ZnO and CdS thickness are kept constant. These curves are shown in Figure 3.4 and the subset in Figure 3.4D shows the grading profiles. The flat profile
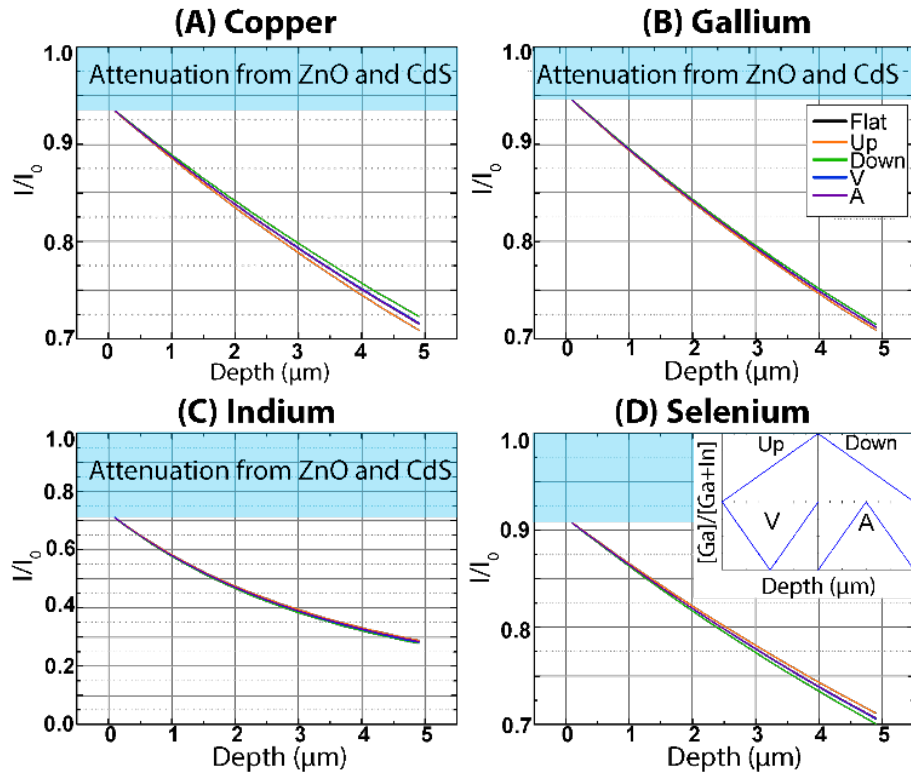
Figure 3.4 I/I$_0$ values for (A) copper, (B) gallium, (C) indium, and (D) selenium as a function of CIGS layer thickness for five different grading profiles all assuming the same average film composition. The insets in (B) and (D) refer to all panels. The difference in scale for (C) should be noted when compared with (A), (B), and (D).

is not shown, but represents a uniform composition throughout the film thickness. Each profile has the same average [Ga]/[Ga+In] ratio of 0.5.

It can be seen that as layer thickness increases, I/I_0 for each element decreases. As the layer thickness approaches 0, I/I_0 values do not reach 1. This is due to the attenuation from the CdS and ZnO layers. It can be seen that for CIGS under these measurement conditions, variations in the grading profile have a small impact $< 1\,\%$ for typical layer thickness $\sim 2\,\mu\mathrm{m}$ but can reach closer to 2 % for Cu and Se for thicker layers. The "V", "A", and flat grading (see Fig. 3.4 inset) profiles show negligible change between them, but slight variations are observed for the linear 'up' and 'down' profiles. The 'down' profile results in less copper and

gallium attenuation compared with the 'up' profile and the opposite was observed for indium and selenium. For indium and gallium this is due to the fact that the highest concentration of these elements is closest to the surface, for their respective grading profiles, resulting in less total signal attenuation from the CIGS bulk. Selenium fluorescence is strongly absorbed by Ga and by having a higher gallium concentration at the surface there is a slight decrease in the selenium I/I_0 . The same justification can be made for copper fluorescence being more affected by a high indium concentration at the surface .

Using the same geometry, layer stack, beam energy and assuming a flat grading profile, we have also examined the impact of surface roughness on I/I_0 . It is clear from Figure 3.4 and the derivation explained in the earlier section that thickness has a large impact on beam and fluorescence attenuation. Figure 3.5 shows the change in I/I_0 for copper, gallium, indium and selenium with varying layer thickness and surface roughness from 10% to 100% of the film thickness with the black reference line representing no surface roughness. The two dashed lines for each surface roughness represent maximum change in I/I_0 for a positive and negative thickness variation. The distance between these lines for a given thickness can represent the uncertainty in the correction factor. CIGS films investigated typically have a surface roughness between $150\,\mathrm{nm}$ and $200\,\mathrm{nm}$ for films that are between 1.5 and $2\,\mathrm{\mu m}$ thick, leading to $\sim 10\%$ surface roughness. This leads to ~ 2 % uncertainty for Cu, Ga, and Se Kα lines and ~ 5 % uncertainty for indium. As total film thickness increases the uncertainty in the correction factor for a given surface roughness also increases. For very rough samples with materials that have high attenuation coefficients, the uncertainty in the correction can be quite large if surface roughness is not considered.

I/I_0 values for copper (A), gallium (B), indium (C) and selenium (D) as a function of CIGS layer thickness for five different surface roughness, from $\pm$ 10% of the film thickness to $\pm$ 100% of the film thickness. The difference in scale for indium (C) should be noted when
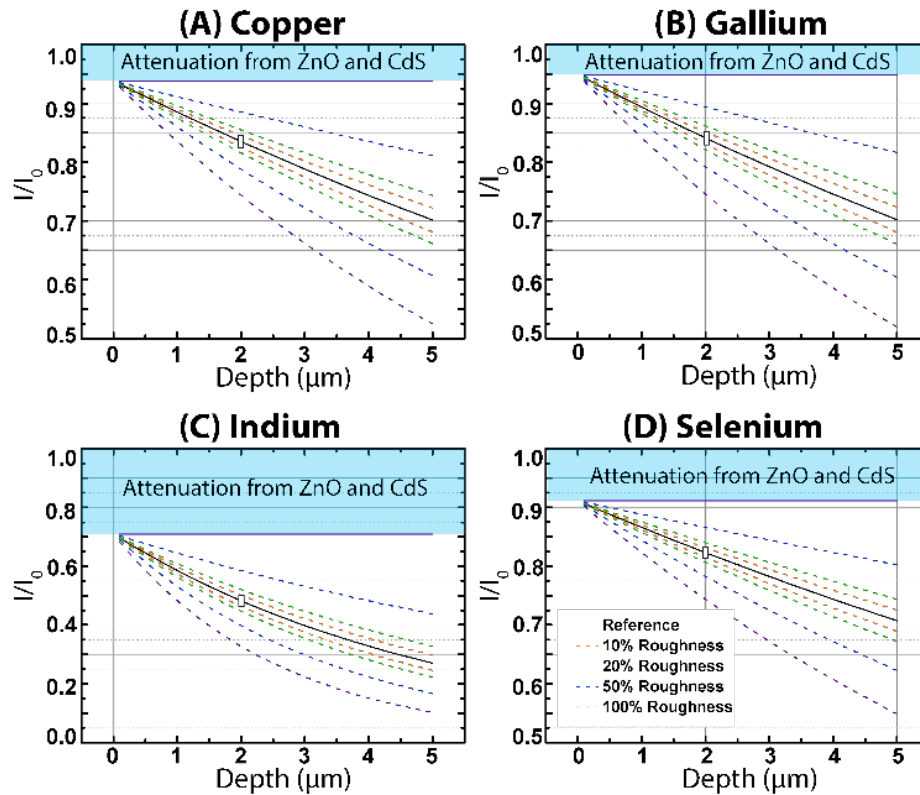
Figure 3.5 I/I$_0$ values for copper (A), gallium (B), indium (C) and selenium (D) as a function of CIGS layer thickness for five different surface roughness, from $\pm$ 10% of the film thickness to $\pm$ 100% of the film thickness. The difference in scale for (C) should be noted when compared with (A), (B), and (D). The white box across the reference line at 2 μm in all panels represents a typical CIGS film with 10% surface roughness.

compared with (A), (B), and (D). The white box across the reference line at 2 μm in all panels represents a typical CIGS film with 10% surface roughness.

It can be seen that there is a large uncertainty for elements with high attenuation coefficients in rough films. To reduce this uncertainty and bring I/I_0 as close to 1 as possible, the path lengths for both the incident beam and exiting fluorescence should be reduced. This can be challenging, as the angle between incident beam and fluorescence detector is often mechanically fixed to 90° to reduce the background signal from scattered photons. This leads to a trade-off between the excitation volume of the beam and the path length of fluorescence. For a fixed detector/beam geometry of θ_{in}+ θ_{out}= 90°, a good compromise is in many cases

θ_{in}= 15°. However in an ideal case, θ_{in}= 0°, such that a pixel in the map corresponds to the fluorescence signal of a perpendicular column in the sample (for a $2\,\mu m$ thick layer stack, an incident angle of 15° corresponds to the collection of fluorescence photons generated along $\tan(15°)$ x $2\,\mu m = 536\,nm$ in the plane of the sample surface). This is typically much wider than the spot size of the beam, which decreases the lateral spatial resolution given by the spot size.

It is important to note that while individually the sources of error maybe small, when they are combined during the analysis they can result in non-negligible quantities, especially when handling multiple elements with low I/I_0 values, similar to indium in the case described above.

While the data shown here are based on CIGS thin film solar cells, the process can be applied to any layered structure where surface roughness and depth dependent composition variations are non-negligible. This process also enables the investigation of metal contaminates in silicon solar cells by estimating the depth of the detrimental contaminate. The investigation of fuel cell can be expanded to allow for *in situ* characterization of membrane contamination, by correcting for losses through the anode, cathode, and membrane assembly. Therefore, the presented approach is a useful tool with broad reaching impact across multiple disciplines, to be coupled with existing XRF analysis software, increasing the quantification accuracy, understanding areas of uncertainty, and enabling the analysis of more complex samples.

Chapter 4

IMPACT OF GALLIUM ON CIGS INHOMOGENEITIES

The following section describes the applications of XRF and XBIC microscopy to the study of composition variations at grain boundaries in low and high gallium CIGS solar cells. This section is also published elsewhere [90]. A schematic of the experimental set up used to study low and high gallium CIGS cells, is shown in Figure 4.1. Given that the XBIC and XRF signals are excited by the same nanoprobe X-ray beam, we are able to report spot-to-spot correlated electronic and compositional properties. The corresponding analysis is highly statistical to provide a reference for the large variation in grain boundary behavior reported in literature.

CIGS devices with average [Ga]/[Ga+In] (GGI) values of 0.3 and 0.6 were grown at the National Renewable Energy Laboratory, using a 3-stage co-evaporation [22, 34]. The device structure is comparable to that shown in Figure 4.1, with a $200\,\mathrm{nm}$ ZnO layer, $50\,\mathrm{nm}$ CdS, $1.8\,\mathrm{\mu m}$ CIGS, $700\,\mathrm{nm}$ Mo, grown on a $1.6\,\mathrm{mm}$ soda lime glass substrate. Because typical CIGS grain sizes are 1-2 μm, CIGS layers were grown slightly thinner than the typical $2\,\mathrm{\mu m}$ to $3\,\mathrm{\mu m}$ to ensure a single layer of columnar grains. Final device solar energy conversion efficiencies were 18% and 14% for GGI = 0.3 and GGI = 0.6 respectively, and consistent with the trends in Fig. 2.5.

Samples were measured at the hard X-ray nanoprobe beam line at the Center for Nanoscale Materials at the Advanced Photon Source [96]. The angle between the beam and detector was fixed at 90° and the sample was tilted to 75° from the sample surface to the incident beam. We chose a beam energy of $10.5\,\mathrm{keV}$, just above the Ga absorption K-edge, for the highest cation sensitivity and to ensure sufficient incident photon flux to remain sensitive to composition variations. Therefore, selenium was not measured (K edge at $12.66\,\mathrm{keV}$). Zone plates with
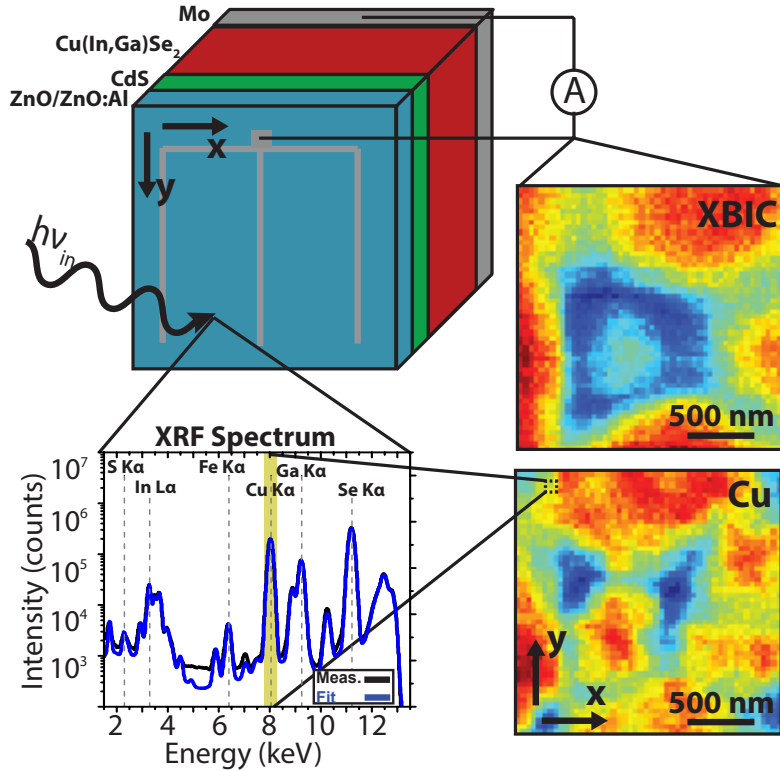
Figure 4.1 Overview of beamline setup and measurement capabilities for XRF and XBIC, capable of collecting composition and charge carrier collection efficiency simultaneously with high spatial resolution.

$180\,\mu m$ diameter and $50\,nm$ outer zone width were used giving a $60\,nm$ beam full width at half maximum (FWHM) and a depth of focus of $52\,\mu m$.

The collected XRF spectra were fitted using the MAPS software developed at APS [126, 127] and quantified using a thin film standard of known composition produced by AXO Dresden (see table 3.2). More information on the fitting processes is available in [131]. We corrected the data for surface roughness, losses due to beam and fluorescence attenuation, and depth dependent compositional variations due to gallium grading following the steps described in Chapter 3. XBIC data were converted to X-ray collection efficiency (XCE) as described in section 2.2.4. The carrier generation was estimated based on the incident photon flux, the percent of photons absorbed in the material, and the ionization energy of the material. Due
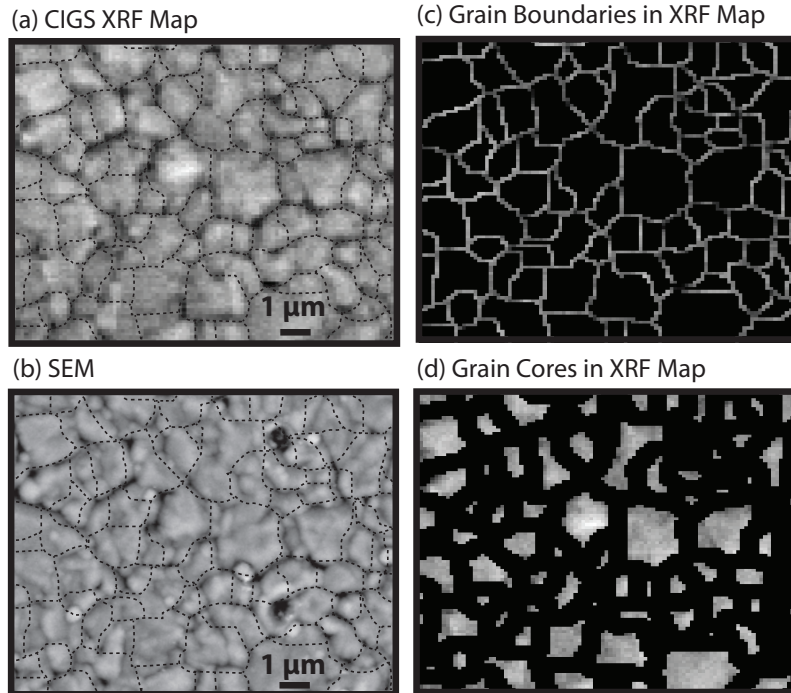
Figure 4.2 (a) XRF image of the sum of the Cu and Ga channels. Indium was not used to reduce the noise in the image. The dashed black lines over the image are the result of the watershed image processing technique. (b) A backscattered electron image of the same location measured by XRF. A watershed is overlaid on each of the images confirming its identification of grains and grain boundaries (c,d) The isolation of grain boundaries and grain interiors as related to the watershed image.

to uncertainty in the estimation of the incident photon flux, the maximum of the data set was scaled to 100 % XCE, for this data set, for ease of comparison.

Photoluminescence (PL) data were collected to corroborate with the GGI values determined from XRF measurements. PL maps were collected using a Renishaw in-Via Raman microscope with a $532\,\text{nm}$ nm laser. Maps with dimensions of $10\,\mu\text{m} \times 10\,\mu\text{m}$ ($100\,\text{nm}$ step size) were collected with a 100x objective and numerical aperture of 0.85 yielding a spot size of $\sim 900\,\text{nm}$. Spectrally resolved photoluminescence was collected for each pixel in the map using a silicon CCD detector for the cell with a high gallium absorber, and an Andor InGaAs near-IR detector for the cell with low gallium absorber.

Grain boundary regions were isolated from grain core regions using a watershed analysis [128]. Grain cores were regions identified as $400\,nm$ away from a grain boundary, to account for the tilt of the sample during the measurement. Figure 4.2(a) shows an XRF map of the CIGS layer and a corresponding SEM Back-scattered electron image of the same region (Figure 4.2(b)). The watershed analysis was conducted using the XRF map and then overlaid on the SEM image. Since XRF is not a structural measurement, an alternative method is needed to validate the watershed. The good agreement between the two images confirms that grain boundaries were properly identified [132]. Figure 4.2(c) and (d) show the resulting image after separation of grain boundary and grain core regions respectively.

4.1 Results

Figure 4.3 shows the copper, gallium and indium XRF channels of a CIGS device side by side to the X-ray collection efficiency map (from XBIC) and the calculated GGI and [Cu]/[Ga+In](CGI) ratios. The black lines in the figure delineate the position of the grain boundaries, defining in this case three different grains with very different composition and electrical behavior. It can be seen that the top left grain core has a higher gallium and copper concentration compared to the neighboring grains, as well as a higher GGI and CGI. Throughout the map indium anti-correlates with copper and gallium, something we observed in multiple scans. The indium and gallium anti-correlation is expected since they are substitutional in the CIGS matrix. Even though this technique does not provide atomic resolution the indium-copper anti-correlation could point to the generation of Cu_{In}'' acceptor or $In_{Cu}^{\bullet\bullet}$ donor anti-site defects. It can be seen that regions with higher Cu and Ga (lower In) content have higher XCE than regions with lower Cu and Ga concentration. Composition does not seem to be the only source of variations in XCE as can be noted from the bright triangular-shaped

53
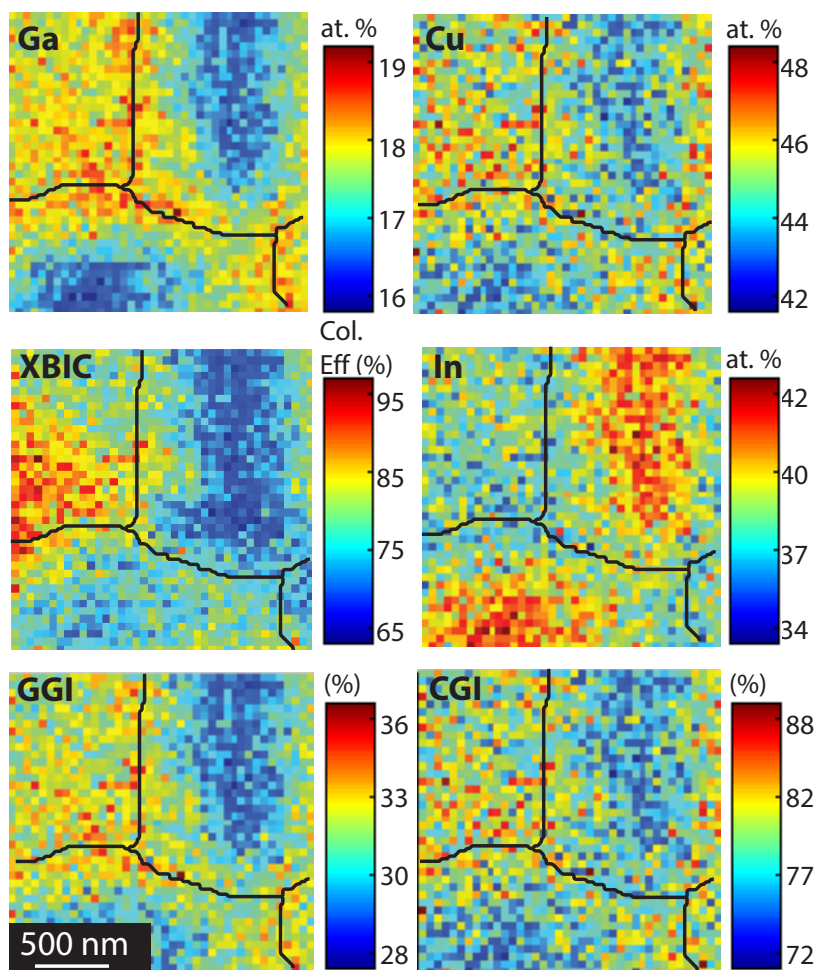
Figure 4.3 Typical XRF/XBIC maps of the Cu, Ga, In channels and the elemental ratios GGI and CGI. Atomic percent, refers to the cation (Cu,Ga,In) percentage as Se was not detected. Each map is $2\,\mu m \times 2\,\mu m$ with $50\,nm$ step size

region in the current collection map that does seem to have a counterpart in the composition maps. In this map Ga rich and In poor boundaries are able to be detected. Similar maps to 4.3 were collected in multiple spots on both low and high gallium CIGS samples. Over 1000 data points were acquired for grain cores and grain boundaries in these samples and most of the data treatment described hereafter is highly statistical in nature.

Figure 4.4 shows the distribution of the composition and charge carrier collection efficiency measured at grains and grain boundaries for both low and high GGI absorber layers. For low
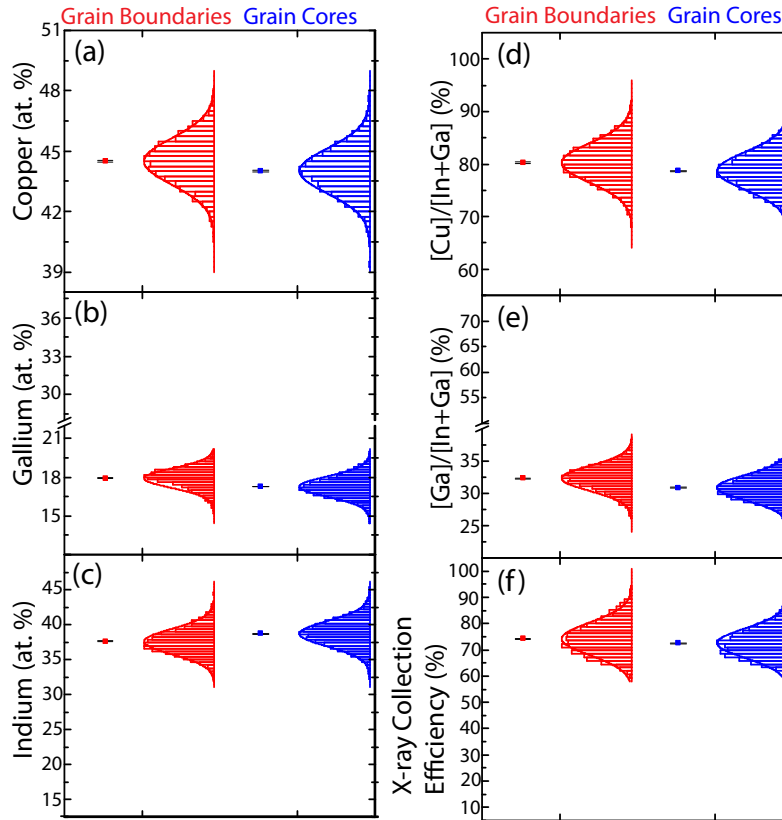
Figure 4.4 (a-f) shows the distribution of copper, gallium, indium, CGI, GGI concentration, and XCE for 30% gallium samples between grains and grain boundaries. The histograms show the distribution of composition measured at each region and the solid line is a fit to a normal distribution. The data point next to the distribution represents the mean $\pm$ the standard error with 95 % confidence.

GGI (Figure 4.4 (a)-(f), there is a noticeable change in the composition between the grain boundaries and grain cores. The compositions measured follow a normal distribution, with similar standard deviations at GBs and GCs, and shifts observed in the mean. The average copper content across all boundaries is observed to be 0.5 ± 0.05 at.% higher than the grain cores. An increase in gallium (0.65 ± 0.03 at.%) and decrease in indium (-1.1 ± 0.08 at.%) was observed as well at boundaries with respect to cores. Similar trends were observed for the CGI and GGI elemental ratios. The average CGI increased from grain cores to grain boundaries by 1.5 ± 0.2 % and GGI increased by 1.4 ± 0.08 %. The uncertainty was calculated as the
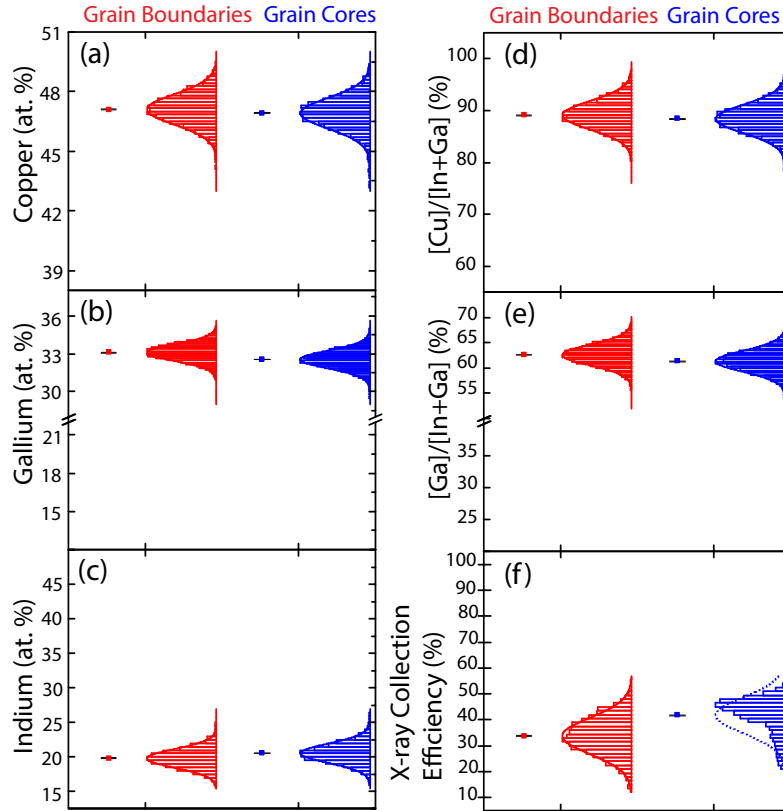
Figure 4.5 (a-f) shows the distribution of copper, gallium, indium, CGI, GGI concentration, and XCE for 60% gallium samples between grains and grain boundaries. The histograms show the distribution of composition measured at each region and the solid line is a fit to a normal distribution. The data point next to the distribution represents the mean $\pm$ the standard error with 95 % confidence.The non-normal distributions seen in the collection efficiency are acknowledged by a dashed curve rather than solid line.

standard error with 95% confidence. The XCE also shows a 1.6 $\pm$ 0.3 % increase from grain cores to grain boundaries indicating improved charge transport at grain boundaries.

For high GGI (Figure 4.5 (a)-(f)) absorber layers, the change in composition between GC and GB is smaller than the change observed for low GGI. A negligible change in copper concentration from GC to GB (0.19 $\pm$ 0.04 at. %) was observed, near the detection limits for this measurement. A slight increase in CGI 0.69 $\pm$ 0.13 at. % approximately half that of the low GGI film. A larger change was observed for gallium (0.55 $\pm$ 0.03) and indium (-0.7 $\pm$

0.06) as well as a positive change in GGI (1.2 ± 0.1 at. %). The largest change for this sample was observed in the XCE with a decrease of 8.0 ± 0.3 % from GC to GB. The non-Gaussian distribution of the grain core XCE should be noted. This is likely due to the large variation observed in collection between large and small grains. Because the data is represented on a pixel by pixel basis the larger grains with a higher XCE are weighed more heavily.

The errors reported here are the 95 % confidence intervals for the average of the sample set. The uncertainty due to thickness variations reported in section 3.2.3 are associated with the absolute quantification of a single pixel. Larger sample sizes (N > 1,000 vs. N = 1) reduce the uncertainty in the population average provided the sample set follows a normal distribution, which is shown in Fig. 4.4 and 4.5. This accounts for the discrepancy in the errors reported in here and in the previous chapter. Additionally, the composition variations observed in this study are greater than the 2 % uncertainty for copper and gallium and 5 % uncertainty for indium.

We plotted the copper, gallium and indium concentrations and elemental ratios against the measured XCE, on a pixel by pixel basis, for all grain cores and grain boundaries. The data was fit to a line and the slopes were extracted, representing the change in atomic percentage with respect to the change in collection efficiency. An example of this is shown in Fig. 4.6

Large values for slope indicate that for a large change in composition a smaller change in collection efficiency is observed. Similarly, smaller slopes indicate a higher dependence of collection efficiency on composition. However due to the wide distribution of composition values, there is a minimum threshold above which a correlation can be detected. This threshold was determined as the standard deviation of the composition divided by the maximum change in collection efficiency.

An analysis of the residuals was conducted to ensure that a linear regression model is appropriate to describe the data. An unbiased regression should result in residuals of the fit
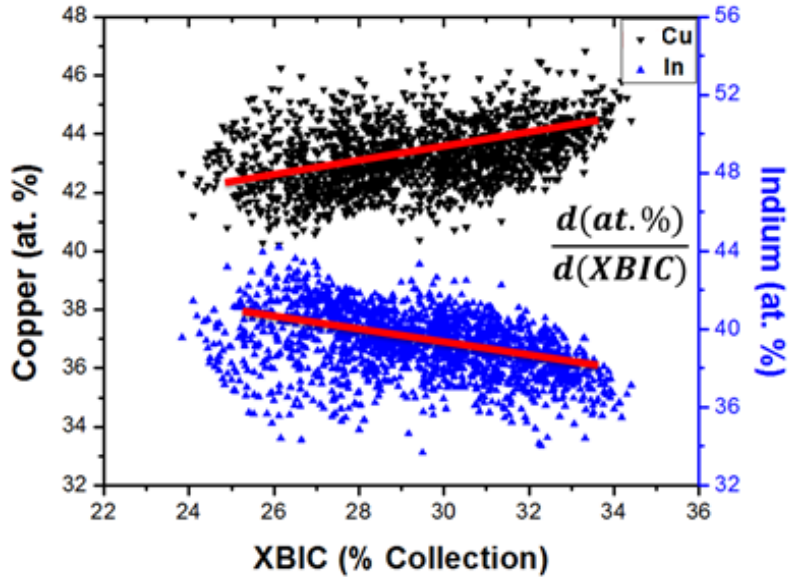
Figure 4.6 Scatter plot showing the point to point correlation between copper and indium atomic percent and XBIC. The red line is used to highlight the trend observed in the data. Copper has a positive correlation with XBIC and indium has a negative correlation

following a normal distribution. This analysis is shown in Figure 4.7. The data is shown in the form of a probability plot, where the y axis is scaled to a Gaussian distribution. Residuals following a linear trend support the use of a linear regression.

The results are shown in Figure 4.8 with the height of the bar correlating to the magnitude of the slope extracted from the scatter plot and the uncertainty is represented as the standard error of the slope with 95 % confidence. Slopes that fall below the minimum threshold are shown without color.

For low GGI absorbers, we observe that Cu and Ga correlate positively with collection efficiency and In correlates negatively. XCE seems is more dependent on gallium concentration, compared to copper and indium, due to the smaller slope. Both CGI and GGI correlate positively with collection efficiency, indicating that that increasing the GGI and CGI at both grain boundaries and grain cores in low GGI CIGS will lead to improved charge
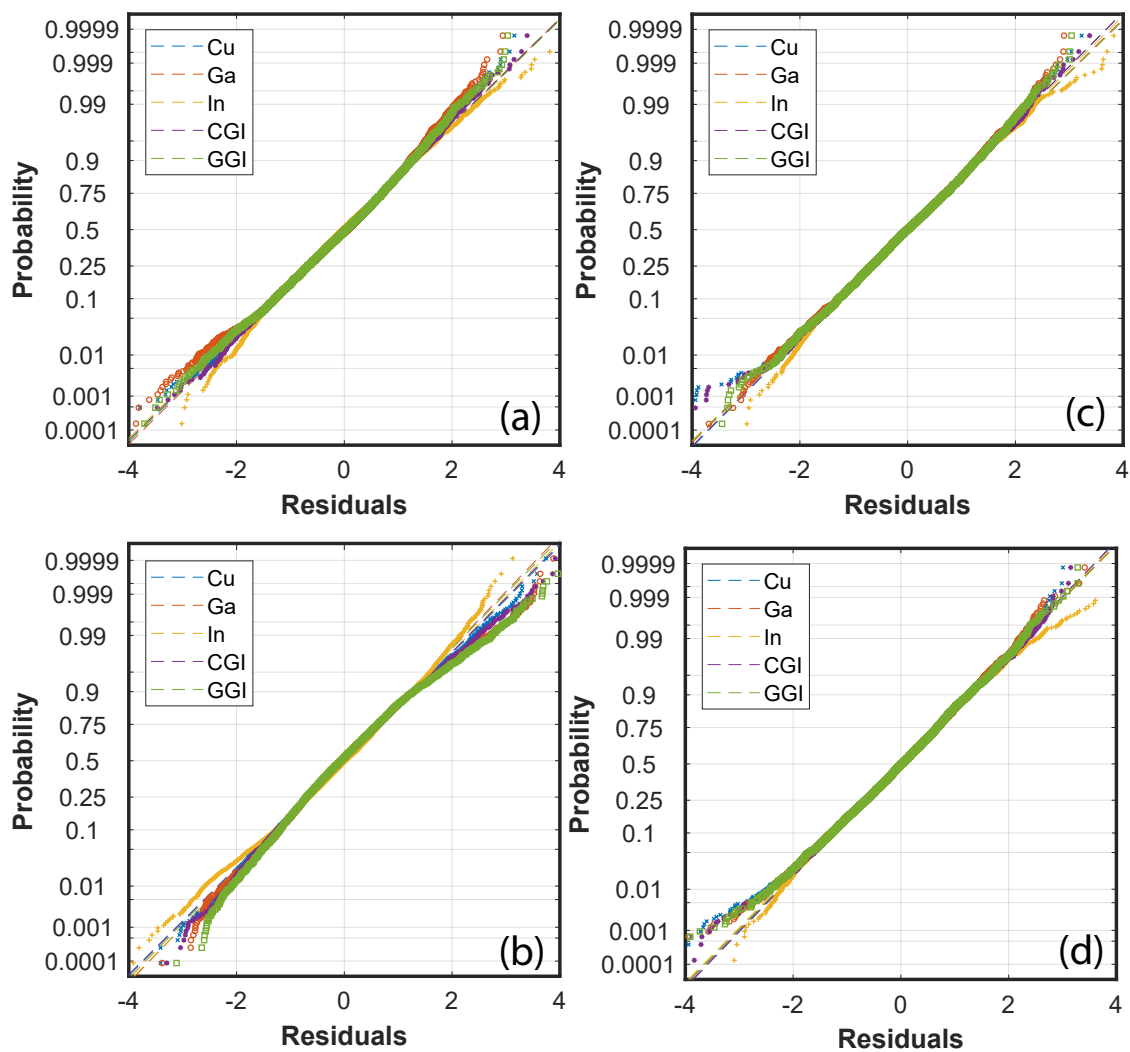
Figure 4.7 Probability plot of the residuals (symbols) from the linear fit of composition against X-ray collection efficiency for both low (a,b) and high GGI films (c,d) at grain boundaries (a,c) and grain cores (b,d). Note the Gaussian scaling associated with the probability. The dashed lines are a Gaussian fit of the residuals.
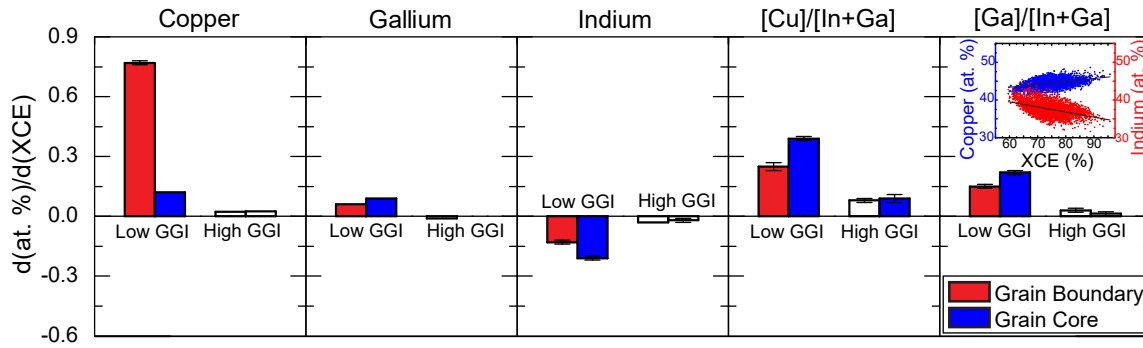
Figure 4.8 Shows the values of slope, correlating composition and elemental ratios charge collection, at different regions, for both low and high GGI CIGS. High slopes indicate a small change in XCE for large composition variations. A low slope indicates small change in composition has a large impact on collection efficiency. The error bars represent the standard error associated with the slope with 95 % confidence. Bars shown without color fall below the detection limit for this analysis. The inset shows a scatter plot of each pixel in a Cu and In XRF map plotted against XCE.

carrier collection. The XCE is more sensitive to changes in CGI and GGI at grain boundaries than the grain cores, indicating a potential area for improvement.

Collection efficiency at grain boundaries in the high gallium absorber exhibit is largely independent of composition, or below the detection limits of this analysis . The grain cores show a unique behavior with CGI showing a strong positive correlation with XCE, and largely independent of indium and gallium concentration. This suggests that, although the change in copper concentration between grain boundaries and grain cores is small, increasing the CGI at grain cores will lead to increased carrier collection.

4.2   Sensitivity Analysis

The values reported in Section 4.1 are smaller than other composition variations reported [61, 133], which were measured by an electron beam, due to the relatively large beam spot size compared to grain boundary area. Figure 4.9 shows the impact of beam spot size, and
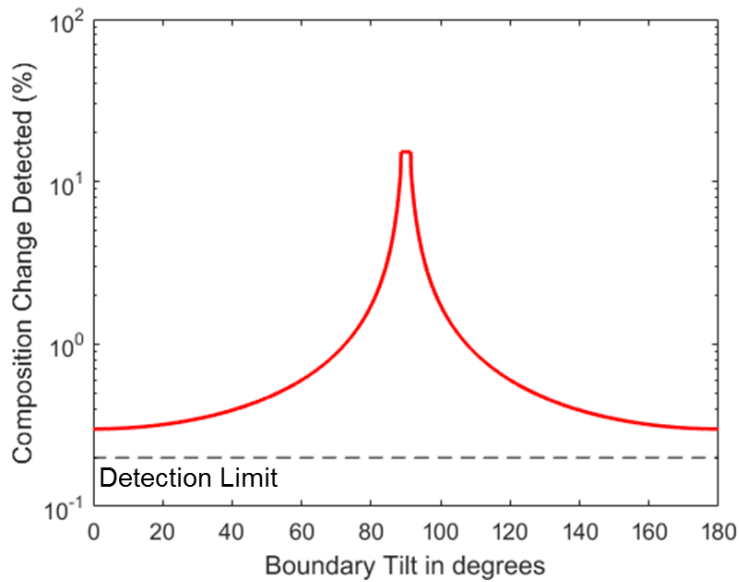
Figure 4.9 Back of the envelope calculation investigating the impact of using a $50\,\mathrm{nm}$ beam spot size to detect a composition change of 50% over $4\,\mathrm{nm}$ at an atomically sharp grain boundary. $90°$ is a grain boundary perpendicular to the surface (parallel to the beam path). The grain boundary was assumed to be a rectangular prism with a width of $4\,\mathrm{nm}$ a height of $2\,\mathrm{\mu m}$ and an infinite length. Measurement volume of the beam was assumed to be a cylinder with height of $2\,\mathrm{\mu m}$ and a diameter of $50\,\mathrm{nm}$. The percent composition change is the ratio of the grain boundary volume (within the measurement spot) to the measurement volume multiplied by the predicted composition increase (50%).

grain boundary tilt on the measured composition of a grain boundary. The grain boundary was assumed to have a 50 % increase in composition occurring over a $4\,\mathrm{nm}$ region with respect to the grain cores.

We have shown that sub-nanometer spatial resolution is not required to detect composition variations at grain boundaries in CIGS, as previously suggested by Abou-Ras et al. [133]. However high sensitivity is required to detect the compositional variations. The high flux of synchrotron light sources, combined with meaningful statistics from measuring multiple spots, yields improved sensitivity to elemental variations. For a single measurement of one pixel we are sensitive to ~ 1 at. % variation in composition. However, when comparing

61

data for over 1000 pixels (at $10.4 \, \text{keV}$) our sensitivity approaches ± 0.13 % for Cu, $\pm 0.19\%$ for Ga, $\pm 0.24\%$ for In, $\pm 0.18\%$ for CGI, and $\pm 0.23\%$ for GGI, which is below the range of values reported in this work for low gallium absorbers. Our analysis of the variation in the overall copper content in high gallium absorbers could be limited by this sensitivity. By having high statistics, we are able to detect composition variations much smaller than the FWHM of the beam. As mentioned previously the large size of the beam relative to length scale of composition variations around grain boundaries, is the reason the values reported here are smaller than those reported in other works.

4.3   Composition of High Performing Regions

In addition to investigating composition and XCE at grain cores and grain boundaries, we also investigate the composition of the best performing regions of each cell. By isolating the best performing areas of the cell, new cells can be grown targeting compositions for optimal charge collection efficiency. Comparing XCE data across all maps collected for low GGI and high GGI CIGS films, we isolated the 90, 95, 99, 99.9, and 99.99 percentiles, of the data.

Figure 4.10 shows the average copper, gallium, and indium composition of each percentile for the low GGI absorber. Consistent with the results from the previous section, it can be seen that regions with higher XCE also have higher copper and gallium concentrations. Indium concentration decreases with increasing XCE percentile. The error bars on the graph represent the variance within each set. The variance decreases as the percentile increases, indicates higher performing regions have similar composition. The average composition between the 90 and 99.9 percentiles fall within the variance in all elements, indicating that regions in the top 90% of X-ray collection efficiency are similar in composition to the regions in the top 99.9%.
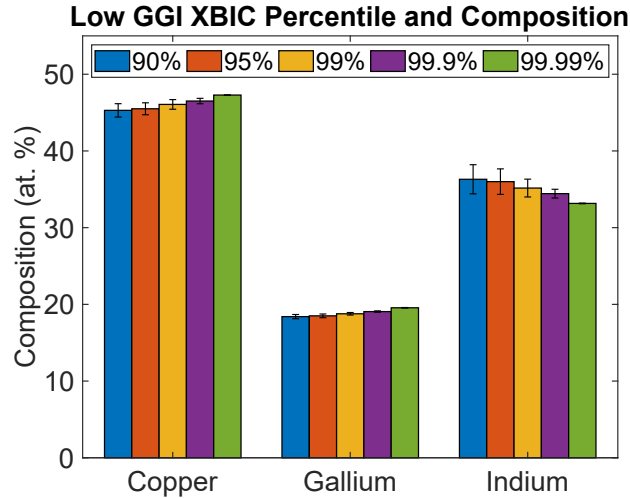
Figure 4.10 Average copper, gallium, and indium composition versus the XCE percentile. The error bars on each bar represent the variance within the percentile

The top 99.99% of pixels measured to have a unique composition. The data used to generate with Figure 4.10 is shown in Table 4.1.

It can be seen in Table 4.1 that the best performing regions of the low GGI absorber have approximately 47% copper, 33% indium, and 20% gallium. It is important to note that this composition does not guarantee optimal performance. Solar cells are limited by the worst performing region, and the root cause of the poor performance may be independent of composition.

Table 4.1 Average composition and XCE with increasing XCE percentile, for the low GGI absorber

Percentile (%)	N	Avg. XCE (%)	Avg. Cu (%)	Avg. In (%)	Avg. Ga (%)
90	2701	82.0	45.3	36.3	18.4
95	1135	84.5	45.5	36.0	18.5
99	270	88.7	46.1	35.2	18.8
99.9	27	93.6	46.5	34.4	19.1
99.99	3	97.8	47.3	33.2	19.6
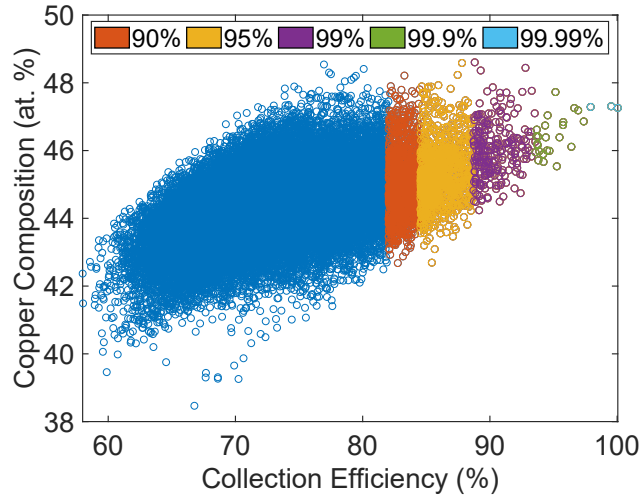
Figure 4.11 Scatter plot showing copper concentration vs. collection efficiency for the low GGI absorber

Figure 4.11 shows a scatter plot of copper concentration vs. collection efficiency. The dark blue points are data that fall below the 90 percentile. Although the correlation between copper and collection efficiency is positive, the distribution of the data is wide. For example, the three data points in the 99.99 percentile of XCE do not fall in the 99.99 percentile of the copper concentration. In fact, there are many pixels with a copper concentration of $\sim 47\%$ indicating that composition is not the only factor affecting XCE. This trend is observed similarly in the indium and gallium as well.

Figure 4.12 shows the average composition of copper, indium, and gallium, in each XCE percentile selected, for the high GGI absorber. Similar to the low gallium absorber it can be seen that as the higher performing pixels also have a higher copper concentration, with a negligible change in the gallium and indium channels. Unlike the low gallium absorber however, the 99.99 percentile is not unique in composition compared to the 90 through 99.9 percentile. This is in agreement with the results from Section 4.2, where we showed that XCE is independent of composition in high GGI absorbers. Table 4.2 shows the average XBIC,

64
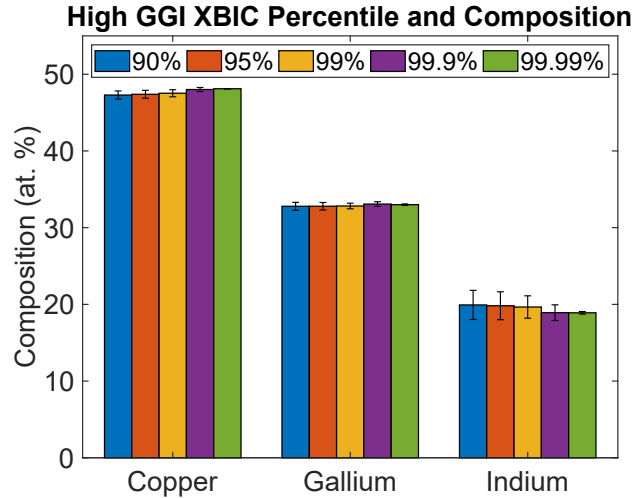
Figure 4.12 Average composition and XCE with increasing XCE percentile, for the high GGI absorber

copper, indium, and gallium concentration for each percentile. The 99.99 percentile of pixels in the high GGI absorber, have an average composition of ∼ 48% copper, 19% indium, and 33% gallium. However, due to the the independence of collection efficiency with respect to comosition, it is unlikely that growing films with this composition would result in increased performance. This highlights the importance of correlative studies of CIGS solar cells, to begin to separate the contribution different material properties (composition, structure, bandgap, etc.) on device performance.

Table 4.2 Average composition and XCE with increasing XCE percentile, for the high GGI absorber

Percentile (%)	N	Avg. XBIC (%)	Avg. Cu (%)	Avg. In (%)	Avg. Ga (%)
90	2701	45.2	47.3	19.9	32.8
95	1135	46.9	47.4	19.8	32.8
99	270	49.7	47.5	19.7	32.8
99.9	27	52.4	48.0	18.9	33.1
99.99	3	54.0	48.1	18.9	33.0

4.4   Discussion

Our results show a similar Cu and In anti-correlation as reported by [61, 133] and clarifies the average behavior of low and high gallium absorbers across multiple boundaries showing that it is not just Cu and In segregating at boundaries but CGI and GGI as well. Given the exhibited Cu and In anti-correlation and the increase in GGI at the boundaries, one could imagine that there is an increase of Cu-In anti-sites at grain boundaries, similar to what has been proposed by other authors [133, 134].

Copper, while shown to be highly mobile in CIS appears to be less mobile in higher gallium CIGS based on the much smaller variation in concentration at grains and grain boundaries, within the detection limits of the measurement [135]. This could be due to the increased stability of the chalcopyrite phase with increasing gallium content [136].

The increased gallium content observed at the grain boundaries for both low and high GGI films could explained by the preferential coordination environment of In and Ga. It has been shown in disordered systems like chalcogenide glasses, that indium prefers to have a fixed coordination number (CN) of 5 while gallium can assume a range of CN (4,5,6) [137–139]. This could explain why more gallium tends to segregate towards grain boundaries, where there is more disorder and the coordination environment can vary. Indium on the other hand sits in the grain core in a tetrahedral configuration.

Additionally, the variations in the predicted bandgap based on GGI from XRF data are $\sim$ $20\,\mathrm{meV}$ which aligns well with PL data measured on the same samples and previously reported values [140]. These data are shown in Figure 4.13 for low GGI CIGS and Figure 4.14 for high GGI CIGS. Bandgap values were calculated from the GGI ratio from XRF maps using the E_g. 4.1 where x = [Ga]/[Ga+In] [136]. The average PL peaks position (bandgap) for the low

66
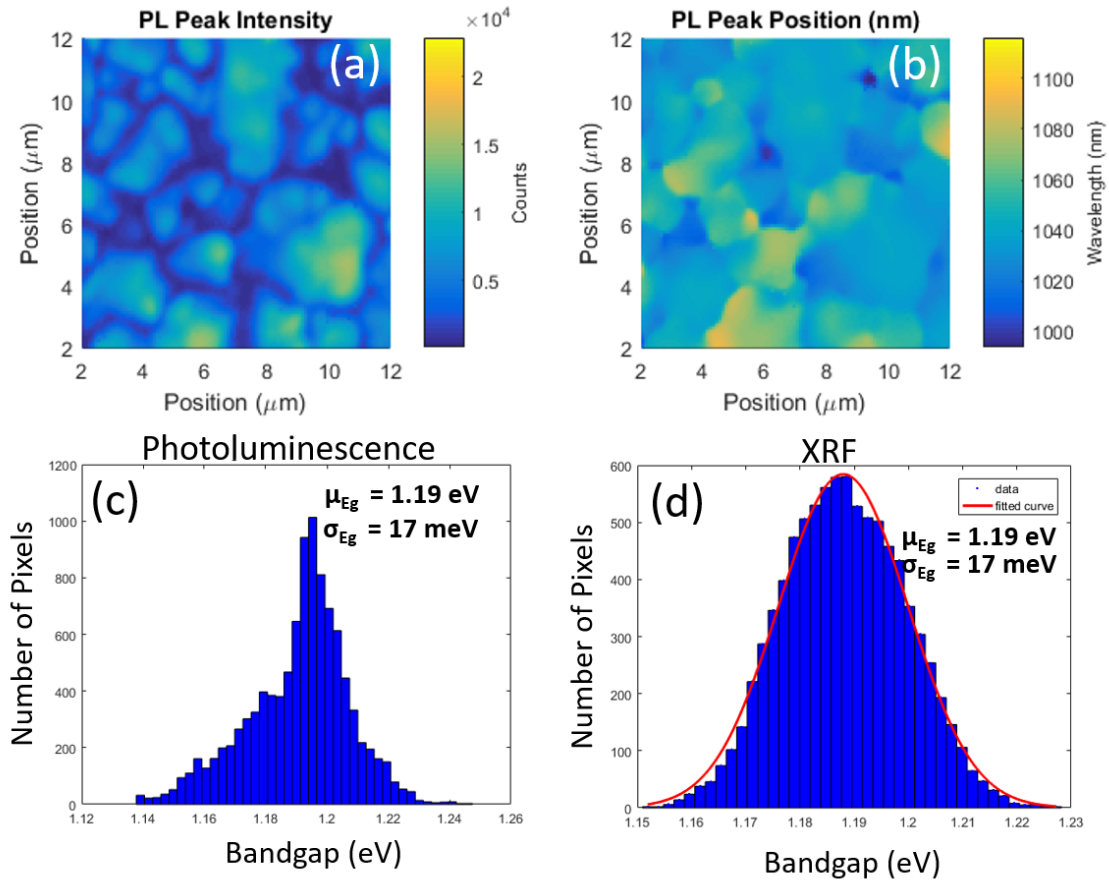
Figure 4.13 Comparison on Low GGI film of Bandgap Variations determined by Gaussian fits of Photoluminescence (PL) spectrum and calculated from GGI ratio measured by XRF. (a) A map of the PL peak intensity. (b) A plot of PL peak position. (c) Distribution of the PL peak position values from (b). σ-E_g is the standard deviation of the PL peak position values and μ-E_g is the average PL Peak position. (d) Distribution of bandgap values calculated from GGI ratios measured by XRF across all grains and boundaries measured. We find good agreement between the bandgap position and standard deviations from two different measurement techniques, however, a non-Gaussian distribution likely caused by the different processes that affect the PL which is much more electrically sensitive, than XRF which is only related to composition
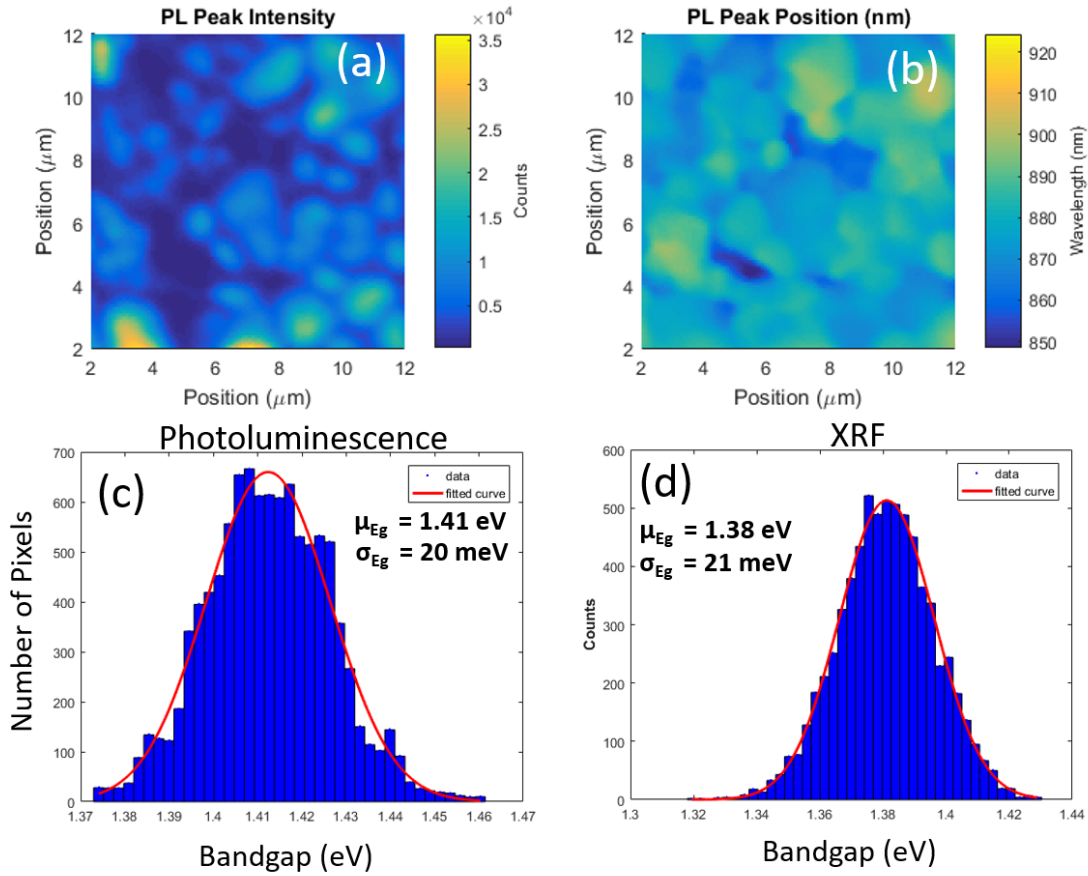
Figure 4.14 Comparison on High GGI film of bandgap variations determined by Gaussian fits of photoluminescence (PL) spectrum and calculated from GGI ratio measured by XRF. (a) A map of the PL peak intensity. (b) A plot of PL peak position. (c) Distribution of the PL peak position values from (b). σ-E$_g$ is the standard deviation of the PL peak position values and μ-E$_g$ is the average PL Peak position. (d) Distribution of bandgap values calculated from GGI ratios measured by XRF across all grains and boundaries measured. We find good agreement between the bandgap position and standard deviations from two different measurement techniques.

gallium film is $1.19\,\text{eV}$ with a standard deviation of $17\,\text{meV}$, the average bandgap calculated by XRF is $1.18\,\text{eV}$ with a standard deviation of $17\,\text{meV}$. The average PL peak position for the high gallium film is $1.41\,\text{eV}$ with a standard deviation of $20\,\text{meV}$ and the average bandgap calculated by XRF is $1.38\,\text{eV}$ with a standard deviation of $21\,\text{meV}$.

$$E_g = 1.04 + 0.65x - 0.26x(1-x) \tag{4.1}$$

The good agreement between composition and PL allows us to correlate composition variations with bandgap fluctuations. The likely cause for the increased collection at grain boundaries in low gallium CIGS is the composition induced electron barrier from an increased GGI and the potential well for holes created by an increased CGI. The decrease in collection at grain boundaries in high gallium absorbers is likely due to the barrier created for electrons by an increased GGI and the 50% smaller hole potential well. The GC collection efficiency for low GGI absorbers could be improved by decreasing this offset (ie: increasing the CGI and GGI). This behavior would also explain why the performance of low gallium CIGS seems to be independent of grain size, based on this study.

To improve the collection efficiency of high gallium CIGS, increasing the CGI at grain cores could promote collection there. Because the collection at grain boundaries is largely independent of composition, the grain cores are regions that should be focused on. Additionally, as one would expect, increasing the average grain size could boost collection efficiency as well to limit the impact of grain boundaries. Due to the apparent lower Cu mobility in high gallium CIGS, adapting growth conditions to enhance copper segregation could be beneficial. Extending the second (copper poor) stage of the co-evaporation process with a long hold at a fixed temperature or decreasing the temperature to enter the mixed phase regime, could improve elemental segregation as well. These processing steps could result in better passivated grain boundaries and increase collection efficiency. Having a higher copper concentration

at the grain cores than the grain boundaries would repel holes, electrically passivating the boundaries and improving current collection in the grain cores.

Lastly, the decreased XCE determined at grain boundaries for high gallium CIGS could be the source for reduced V_{oc} in these devices. Because V_{oc} and recombination are highly correlated, a reduced XCE caused by higher recombination can be correlated to a decrease in voltage as well. It is important to emphasize however, that XCE is a current measurement and further studies are underway to evaluate the behavior of voltage throughout these films.

Chapter 5

IMPACT OF SODIUM ON CIGS INHOMOGENEITIES

The beneficial effects of sodium addition to CIGS absorber layers has been known for quite some time [141, 142]. CIGS cells grown in the presence of Na have increased p-type conductivity [143], an increased V_{oc} and FF [144], and some reports show increased J_{sc} as well [145]. Na addition has also been shown to improve morphology and generate a (112) texture [146, 147].

Na is primarily introduced during growth, via diffusion from the sodium containing soda-lime glass (SLG) substrate. However, for films grown on sodium free substrates such as polyimide or stainless steel, Na is added via precursor layers or doping the Mo back contact prior to growth [148]. It can also be added in the form of a post deposition treatment (PDT) of NaF to films growth on both SLG and Na-free substrates [21, 149]. However, it should be noted that too much sodium can be detrimental at the cell level [150] and on the long-term stability of modules, through the creation of shunt path ways [151].

How and why these benefits occur have been a topic of continued discussion. It is argued that the benefit largely comes from defect passivation at grain boundaries. Density functional theory calculations have found that Na ahnilitates $In_{Cu}^{\bullet\bullet}$ anti-site defects as well as selenium vacancies [50], and an increase in sodium concentration at the grain boundaries has been observed by atom probe tomography and secondary ion mass spectrometry [61, 152, 153].

However, the effect of Na on grain-to-grain homogeneity should be investigated as well. Although the diffusion coefficient of Na along grain boundaries in CIGS is very high, Na also has been shown to diffuse into the grain interiors [154] and transient photo-capacitance have shown a decrease in the urbach tails indicating an increase in the overall film uniformity [155].

Non-uniformities in CIGS absorber layers are known to impact the device performance, from extended charged defects leading to electrostatic potential fluctuations, to bandgap fluctuations originating from a non-uniform distribution of Cu and Ga [70, 89, 133, 156]. This is what motivates the current study. How does the addition of Na from SLG and NaF PDT affect bandgap uniformity in CIGS Cells?

To study this we characterized four samples with Na introduced into the film either from the substrate, a PDT or both. Samples were grown on sodium free alumina (Al_2O_3) and SLG with sister samples exposed to NaF PDT.

5.1 Bandgap Distribution

CIGS Devices with GGI = 30 % were grown at the National Institute of Advanced Industrial Science and Technology (AIST), Japan. Absorber layers were grown via a 3-stage co-evaporation process on molybdenum coated substrates. Sister samples on sodium free (Al_2O_3) and sodium containing (soda lime glass) substrates were used. Each substrate was also treated with and without a NaF post deposition treatment, resulting in 4 unique samples in all. Devices were completed with a $50\,nm$ CdS buffer layer and a $200\,nm$ ZnO:Al window layer. The device properties of each sample is shown in Table 5.1. As expected, as Na concentration increases, the device performance also increases, primarily through increases in V_{oc} and FF.

Table 5.1 Device properties of sodium samples prepared at AIST

Sample	V_{oc} (mV)	$J_{sc}(mA/cm^2)$	FF (%)	Eff. (%)
Al_2O_3	531 ± 2	30.4 ± 0.1	59.0 ± 0.4	9.5 ± 0.1
Al_2O_3 + NaF	607 ± 4	29.9 ± 0.3	68.2 ± 0.1	12.4 ± 0.1
SLG	691 ± 3	31.8 ± 0.2	78.1 ± 0.1	17.1 ± 0.2
SLG + NaF	723 ± 2	31.5 ± 0.2	79.6 ± 0.3	18.1 ± 0.2

To investigate the impact of Na on bandgap inhomogeneities, spatially and spectrally
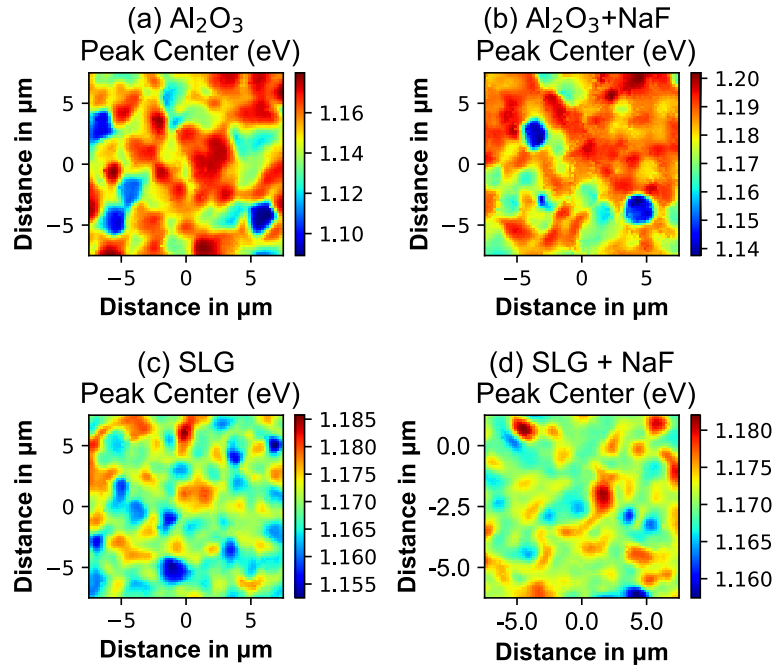
Figure 5.1 PL maps showing peak center positions in eV from samples grown on Na free substrates (a,b) and sodium containing substrates(c,d) as well as samples exposed to NaF post deposition treatments (b,d). Maps are $15\,\mu m \times 15\,\mu m$ with a $200\,nm$ step size

resolved photoluminescence mapping was conducted. PL maps were collected using a Renishaw in-Via Raman microscope with a $532\,nm$ nm laser. Maps were collected with dimensions of $15\,\mu m \times 15\,\mu m$, with a $200\,nm$ step size were collected with a 50x objective yielding a spot size of $\sim 1\,\mu m$. Photoluminescence was collected for each pixel in the map using an Andor InGaAs near-IR detector.

The bandgap was defined as the energy value corresponding to the center of the normalized PL curve. Figure 5.1 shows the x-y maps of bandgap distribution for each substrate and NaF treatment. It can be seen that the range of the colorbars decrease with increasing sodium sources from (a)-(d). It can also be seen that the samples grown on Al_2O_3 substrates have larger feature sizes than the samples grown on SLG.

Table 5.2 Mean, Maximum, Minimum, and Standard Deviation (σ) of PL peak centers shown in Figure 5.1

Sample	Mean (eV)	Maximum (eV)	Minimum (eV)	σ (meV)
Al_2O_3	1.15	1.18	1.08	17
Al_2O_3 + NaF	1.18	1.20	1.09	10
SLG	1.17	1.19	1.15	5
SLG + NaF	1.17	1.18	1.16	3

To quantify the effect of Na concentration on peak center fluctuations the average, maximum, minimum, and standard deviation of each image was determined. These data are shown in Table 5.2. The average bandgap for each image ranges from $1.15\,eV$ to $1.18\,eV$, with the maximum and the minimum of range being associated with Al_2O_3 substrates. Both samples grown on SLG have the same average bandgap. The high and low average peak center for Na free substrates could be due inhomogeneities on length scales greater than the map size. The maximum for each map are similar across all samples, however the minimum bandgap in each map shows a large shift to higher energies ($\sim 80\,meV$) from Al_2O_3 to SLG + NaF. This could be due to defect passivation or a reduction in electrostatic potential fluctuations, both of which reduce the energy average radiative recombination pathway, below the expected bandgap. A similar effect can also be seen by the reduction in the standard deviation of the peak centers. As Na concentration increases, variations in the peak center decrease, indicative of a more homogeneous film. This effect is likely to arise from a reduction in the electrostatic potential fluctuations.

To investigate the effect of Na beyond changes in the PL center from the integrated spectrum, each spectrum was fit to 3 gaussian distributions. All pixels were fit to the same conditions allowing two peak centers to vary from $1.11\,eV$ to $1.3\,eV$ and the third peak to vary from $1.05\,eV$ to $1.1\,eV$ to capture the low energy transition found and many spectra across all

74
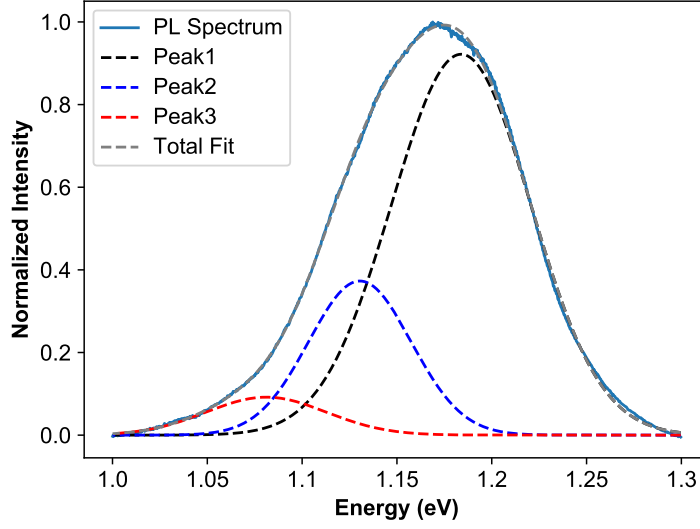
Figure 5.2 Representative PL spectrum from Al_2O_3 + NaF sample. Solid blue line is the normalized PL spectrum. The dashed lines are the result of a least squares fit to 3 Gaussian distributions.

samples. This is shown in Fig. 5.2. It was found that two Gaussian distributions describe the most intense peak well, and one peak was necessary to fit the low energy tail of the spectrum.

In Fig. 5.1(a), low peak center values spanning several micrometers can be observed at (X,Y) = (5 μm, −5 μm) and (X,Y) = (5 μm, −5 μm). Similar features can be seen in Fig. 5.1(b) at (X,Y) = (5 μm, −4 μm), but are lesser in size and magnitude in Fig. 5.1(c,d). These regions are attributed to strong sub-bandgap transitions labeled Peak 3 in Fig. 5.2. While this transition is present in all the samples, the intensity (amount of radiative recombination) associated with was found to decrease with increasing Na concentration.

The distribution of Peak 3 intensity is shown in 5.3. It can be seen that the median intensity value for this transition decreases by an order of magnitude from the sample grown on Al_2O_3 to the sample grown on SLG with NaF treatment. It was also observed that the number of pixels containing a Peak 3 transition decreased from $\sim$ 100% for samples grown on Al_2O_3

75
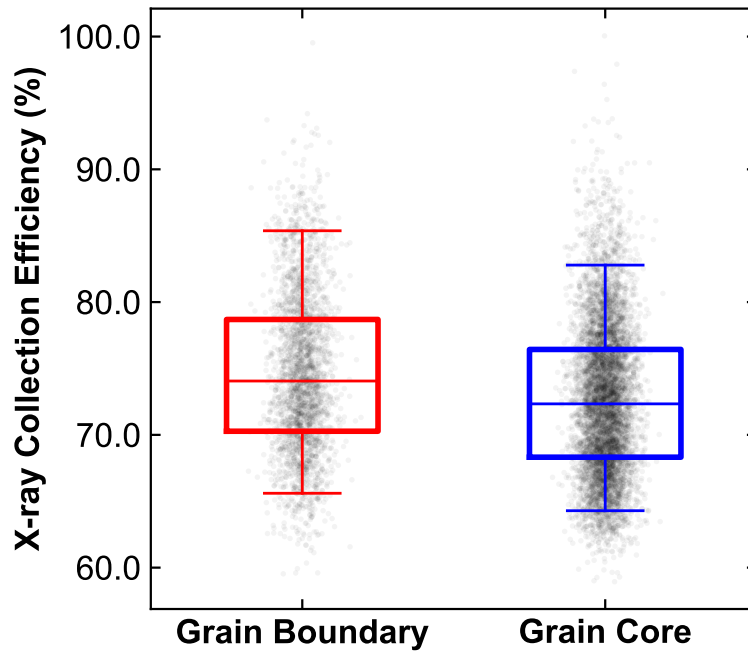
Figure 5.3 Box plot showing the intensity of peak 3 for samples with varried sodium concentration. Data points are plotted in conjunction with box plot distribution with arbitrary x values to show the distribution. A threshold of 0.001 was set for the data for the noise level of the detector

to ∼ 50% for SLG + NaF. Similar increases in uniformity were also observed for Peak 1 and Peak 2. The ratio of the intensity between Peak 1 and Peak 2 decreases with increasing sodium concentration, and the distance between the Peak 1 and Peak 2 centers also decreases.

5.2 Elemental Distribution

The effects of Na concentration on the radiative recombination pathways in CIGS were investigated in the previous section, for low gallium absorbers. Does the increase in homogeneity in optical properties arise from an increase in elemental homogeneity? CIGS absorber layers with GGI = 55 % were grown at the National Renewable Energy Laboratory (NREL), on molybdenum coated soda lime glass substrates. Absorber layers were prepared

with and without NaF post deposition treatments. Post deposition treatments were done by evaporating NaF and holding the substrate temperature at $400\,°C$ for $30\,min$ Devices were completed with $50\,nm$ thick layer of CdS and $200\,nm$ thick ZnO:Al window layer. Table 5.3 shows the device properties for the high gallium device treated with and without NaF. It can be seen that a large boost in the V_{sc} and FF are observed as a result of the post deposition treatment. This is in agreement with the samples grown at AIST and reports in literature [21, 149].

Table 5.3 Device properties of sodium samples prepared at NREL

Sample	V_{oc} (mV)	$J_{sc}(mA/cm^2)$	FF (%)	Eff. (%)
SLG	652	27	65	11.5
SLG + NaF	777	26.5	76	15.6

Samples were measured at the APS beamline 26-ID-C by XRF/XBIC with incident X-ray beam energy above the gallium K edge ($10.4\,keV$) and a spot size of $40\,nm$. The photon energy was kept below $12\,keV$ to maintain a small focal spot size. Therefore, selenium K shell electrons were not excited (Se K edge = $12.66\,keV$). The fluorescence spectra were fitted against a well quantified standard, and the data were corrected for thickness dependent attenuation losses and depth dependent composition gradients as described previously and in [89].

Figure 5.4 shows the difference between the XCE, CGI, and GGI, for NREL samples treated with and without NaF post deposition treatment. The analysis was similar to the method described in Chapter 4, utilizing a watershed analysis to identify grain boundaries. It can be seen that for untreated samples (blue) the grain boundaries exhibit a lower collection efficiency compared to the grain cores on average across all maps. This result is in agreement with the previous study for high gallium CIGS devices. After NaF PDT, it is no longer clear if grain boundaries over or under perform. On average, grain boundaries show an increase in collection
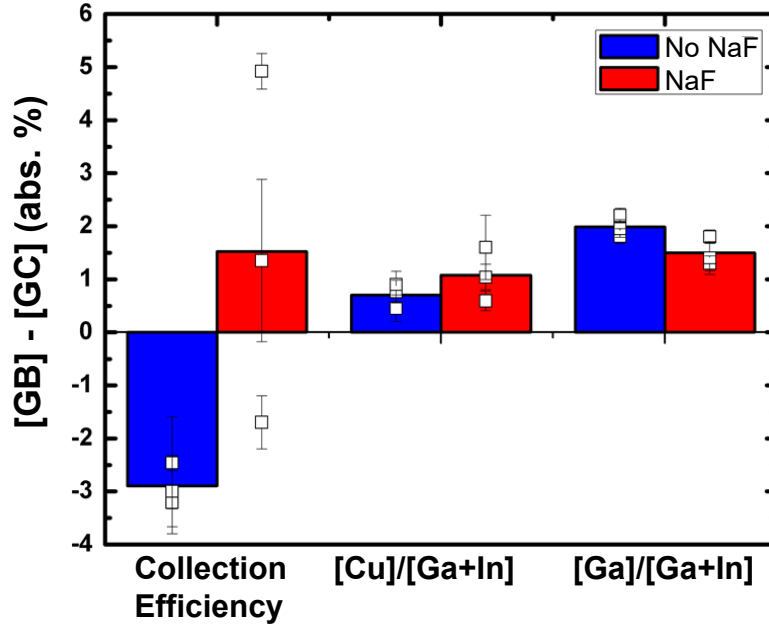
Figure 5.4 Bar graph showing the average change in collection efficiency, [Cu]/[Ga+In], and [Ga]/[Ga+In] , between grain boundaries and grain cores for samples treated with and without NaF post deposition treatment. Each box represents the average change with 95 % confidence intervals for an individual map, and the magnitude of the bar is the average across all maps.

efficiency, however individual maps show varied results. This change in collection efficiency also appears to be independent of changes in composition. However in both samples, grain boundaries exhibit an increase in CGI and GGI compared to the grain cores.

Table 5.4 Standard Deviation of elemental ratios from NREL with and with NaF treatment

Elemental Ratio	SLG	SLG + NaF
σ_{CGI}	2.8%	2.7%
σ_{GGI}	1.9%	1.8%

Table 5.4 shows the standard deviation for the CGI and GGI for samples treated with and without NaF, across all maps measured. It can be seen that the standard deviation of both the CGI and GGI decrease by 0.1% absolute after the NaF treatment. While these results alone are not definitive, due to the small number of samples and difference that approaches

the detection limits for this measurement, it does support the results from the PL study in the previous section. More XRF data should be collected on more samples spanning a broader range of Na concentrations to confirm these findings.

5.3 Spatial Distribution

To investigate the location of Na in the NREL sample with NaF PDF, a soft X-ray scanning transmission microscope (STXM) was used at the Canadian Light Source [157]. Samples for this microscope were prepared using a Focused Ion Beam (FIB) to mill a thin lamella ($100 \, nm$ to $200 \, nm$) of the CIGS film in cross section and subsequently mounted on the post of a molybdenum transmission electron microscopy half-grid. To reduce the risk for gallium ion implantation and surface damage, the lamellae were further thinned using a low energy beam after mounting. The STXM tool is capable of operating just above and below the Na-K absorption edge ($1070.8 \, eV$) ensuring high sensitivity to small traces of this elements.

SX-STM results are presented in Fig. 5.5, showing the on-resonance absorbance image (a) and the differential map (b) for a cross sectional lamella ($< 200 \, nm$) from a CIGS sample treated with a NaF post deposition treatment . The image difference map is the difference between the on-($1077 \, eV$) and off-resonance ($1068 \, eV$) images at the Na-K absorption edge. Bright spots indicate regions of high absorption in that energy range, hence, the presence of Na. It is not surprising to find that the region with the most Na is the soda lime glass, which is the dominating source of Na during CIGS growth. The next bright region of interest is the interface between Mo and CIGS. Due to the high energy associated with surfaces and interfaces, it is natural for contaminates/dopants to segregate and accumulate there. The same segregation is observed towards the ZnO layer suggesting that Na from the soda lime glass can diffuse through the entire CIGS film or Na exists from the PDT. While there is a clear presence

79
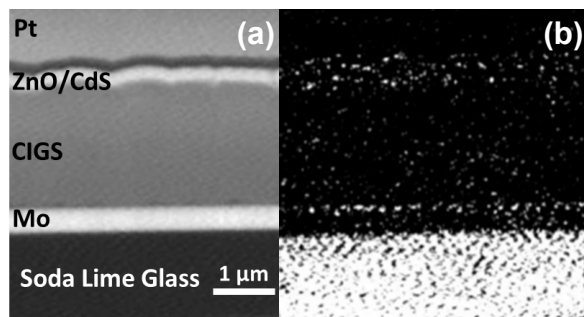
Figure 5.5 (a) On-resonance absorbance X-ray image of a thin lamella of a NREL NaF treated sample. Pt was deposited to protect the surface during the FIB process. (b) Differential map showing the subtraction of the off- from the on-resonance images. White spots indicate regions of high absorption at the Na-K edge.

of Na at interfaces, detecting Na in the bulk is more challenging which points towards the sensitivity limits of this measurement ($\sim$1 at. %) and the limited spatial resolution ($30\,\text{nm}$) for detecting atomically sharp features like grain boundaries. Further tests need to be conducted with increased dwell time to detect Na in the CIGS bulk.

5.4 Discussion

It has been shown that Na leads to a decrease in PL peak center fluctuations, and a suppression of a sub-bandgap peak detected between $1.05\,\text{eV}$ and $1.1\,\text{eV}$ for samples grown at AIST. It was also observed that an increase in collection efficiency is observed at grain boundaries after the addition of a NaF post deposition treatment to the device fabrication process for samples grown at NREL. This increase in collection at grain boundaries is not correlated with a change composition within the detection limits of these measurements. Overall the films were slightly more homogeneous with respect to CGI and GGI after the NaF post deposition treatment. This increase in homogeneity supports the PL results, however composition variations do not account for all of the changes observed in PL. X-ray transmission

maps collected above and below the Na-K edge, for the NREL sample treated with NaF PDT, showed an accumulation of sodium at the CIGS/Mo interface and the CIGS/CdS/ZnO interfaces.

Moving forward, XRF mapping of the AIST sodium series will be conducted on the same spot to correlate the changes observed in PL distributions directly with changes in composition. This will help deconvolve effects from bandgap variations induced by gallium, and the potential fluctuations induced by charged extended defects. Additionally, extending the energy range of data collected at the SXTM to collect full X-ray absorption spectra can identify the chemical environment surrounding Na at the interfaces.

Chapter 6

CIGS GROWTH: KINETICS OF PHASE FORMATION

In the Chapters 4 and 5, I examined the impact of composition variations between grains and grain boundaries on device performance, as well as the impact of Na concentration on bandgap fluctuations and composition variations. It was determined that copper rich grain boundaries lead to improved carrier collection for low gallium absorbers, but does not benefit high gallium absorbers. The question remains: how do these variations originate during growth? The answer to this question is critical to begin engineering CIGS films with desired properties (ie: copper rich grain boundaries). Studying the kinetics of material formation often involves sophisticated characterization methods, and advanced analysis techniques [158–161]. *In situ* techniques commonly study the evolution of structure during growth, by XRD [161] or reflection high energy electron diffraction (RHEED) [162]. These are necessary for studying structural evolution, changing growth regimes, and providing insights into reaction pathways. However, for materials like CIGS whose structure is stable over a wide composition range, and an inhomogeneous distribution of elements are known to impact device performance, these techniques are not suitable. This problem extends beyond CIGS to include material systems like metallic alloys and glasses. To address this we implement, *in situ* X-ray fluorescence microscopy to study the kinetics of nanoscale segregation during CIGS growth.

In the following sections, I describe: the design and construction of the *in situ* stage used in this study, the CIGS growth process selected to investigate, and the results of the investigation. The discussion of the stage and growth methods are also published in [163, 164].

6.1   Development of an In Situ Stage

Designing a stage capable of conducting XRF measurements with sub-micron scale spatial resolution, *in situ* required a strict set of design requirements:

- Target temperatures from room temperature up to $1000\,°C$
- Fast ramp rates ($> 100\,°C/\mathrm{min}$)
- Vertical sample mounting for installation at synchrotron beamline
- Reduce vibrations $< 200\,\mathrm{nm}$
- X-ray transparent window
- Actively cooled front plate
- Atmosphere control
- Exhaust system for toxic gasses
- Feature tracking

Achieving each of these requirements involved multiple design iterations. Figure 6.1(a) shows the initial stage prototype with a simple quartz housing and optical heating element, which failed to meet a majority of the design requirements including: Actively cooled front plate, sub $200\,\mathrm{nm}$ vibrations, X-ray transparent window, and ability to hold the sample in place. Iteration 2, shown in Fig 6.1(b) improved upon these, allowing for an X-ray transparent window, and was able to achieve rapid heating. However, the close proximity of the sample to the front plate, was a likely source for sample contamination. Iteration 3, shown in Fig 6.1(c) improved further, introducing a clamping sample mount, which holds the sample away from the front plate, and the resistive nichrome heaters allowed for rapid temperature ramp rates. However, the sample mount still did not provide sufficient control over sample position, to enable feature tracking. Iteration 6, shown in Fig 6.1(f) was the last iteration prior to the final
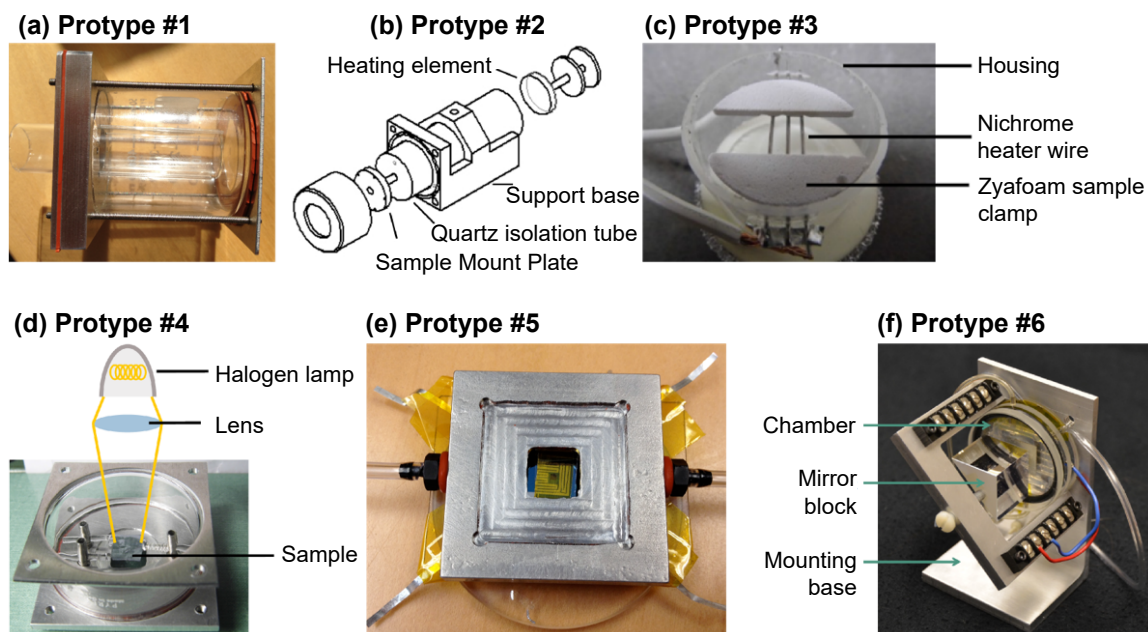
Figure 6.1 (a) Initial stage prototype with sample mounted flush against glass window and large sample chamber. (b) Second stage prototype, telescope assembly, smaller sample chamber, resistive heater. (c) Third prototype, utilized zyafoam insulation to hold sample in place on top of resistive heaters. (d) Fourth prototype, utilized a spring loaded sample holder, and a halogen lamp as the heating element. (e) Fifth prototype, added gas inlet/outlet ports and reverted to a resistive heating element (f) sixth prototype, continued with a resistive heating element, further reduced chamber volume, included mirror block for position tracking with interferometry.

design implemented. Here, mirrors were placed on the back of the stage to track the position via interferometry. The challenge however, was the inability to track the thermal expansion of the sample. The pumping mechanisms for the water cooled front plate introduced large vibrations to the stage.

Figure 6.2 shows a schematic and pictures of the final design of the *in situ* stage. The front plate, back plate, and base of the stage was made from graphite, rather than stainless steel, due to its high temperature tolerance, and resistance to corrosive atmospheres such as H_2S and H_2Se, often used in CIGS growth. A quartz tube completes the outer stage enclosure between the front and back plates. The graphite was impregnated with phenol to ensure that it
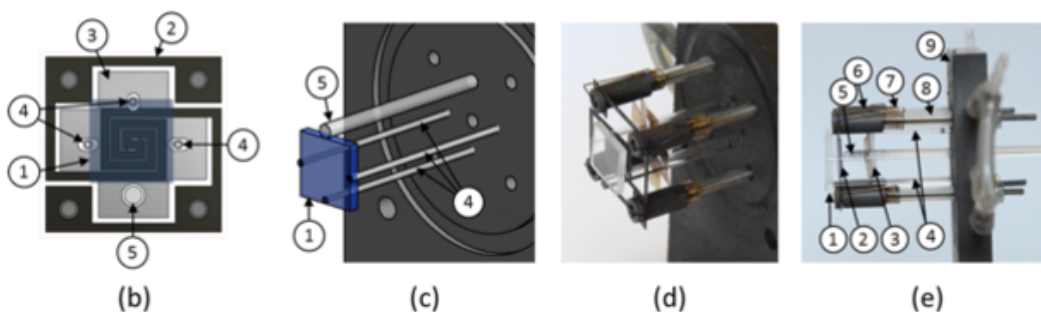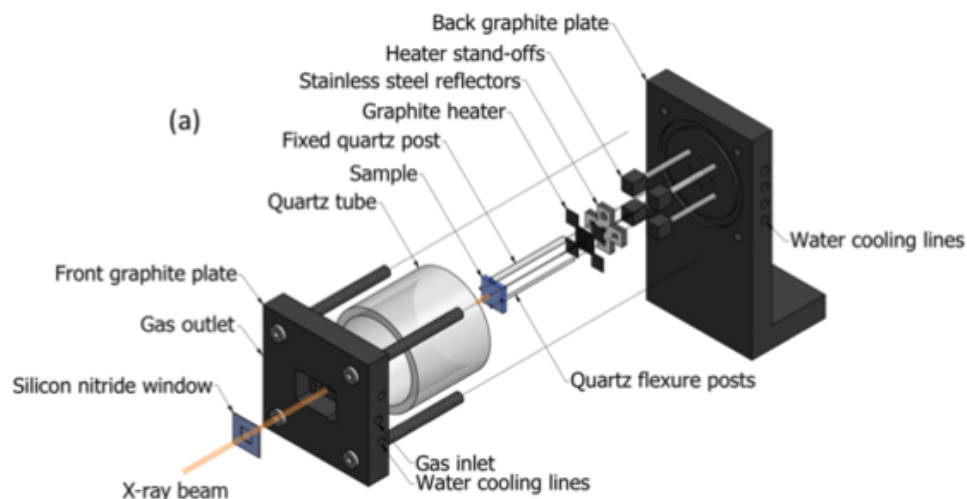
Figure 6.2 Schematics and pictures of the *in situ* stage. (a) Exploded isometric view of all important components of the stage. (b) Sample-facing view of interior components. 1: sample; 2: graphite heater; 3: stainless steel (SS) reflector; 4: quartz flexures; 5: fixed quartz post. (c) Close-up isometric view showing only the back plate, sample (blue), and sample-mounting post and flexures. (d) Photograph of internal components. (e) Photograph of internal components in profile view. 6: graphite contact post; 7: SS spring for capturing graphite heater; 8: quartz-sheathed SS rod for electrical leads to graphite heater. Figure and caption from [163]

is impermeable, and will not release toxic gasses to the environment. The impregnation process however limited the temperatures the graphite could reach, to below $180\,°C$.

To maintain the integrity of the phenol in the graphite and protect the sensitive X-ray optics, active cooling is applied to the front plate. Water is delivered to the stage via a gravity fed systems, once the water exits the stage, it is pumped through a heat exchanger and back to a reservoir kept above the stage. A gravity fed system was selected to reduce the transfer of vibrations from the pump to the stage, via the cooling lines.

A new sample mount was implemented utilizing three quartz flexures and one fixed post. The fixed post limits the degrees of freedom for the substrate expansion by 1. This was intended to allow for feature tracking while collecting measurements. The flexures allow the sample to expand freely in the other three directions.

A laser cut graphite heater was used as a resistive heat source. Current flows through the graphite and thermal energy is transferred radiatively to the sample. The unique design of the heater seen in Fig. 6.2b allows for uniform sample heating, and more accurate 4 point current measurements. The use of graphite and resistive heating allows for the fast temperature ramp rates to temperatures $> 800\,°C$ that were required in the design specifications. The heater is $200\,\mu m$ thick with a resistance between $80\,\Omega$ and $100\,\Omega$. Keeping the graphite heater thin reduces it's thermal mass which also contributes to rapid temperature ramp rates.

6.2 Growth Methods

We studied the growth of CIGS layers via a precursor reaction process as described by Berg et al. [40], with *in situ* with synchrotron X-ray fluorescence (XRF). The *in situ* stage, described in section 6.1, is kept under an inert atmosphere to not degrade the graphite heater or provide gases that could react with the CIGS film. In contrast to Berg, we used helium rather than

argon to reduce the fluorescence signal from the atmosphere. Experiments were conducted at the advanced photon source beamline 2-ID-D. The films were measured at two different beam energies, above the Se-K absorption edge ($12.8\,\mathrm{keV}$) and above the Ga-K absorption edge ($10.5\,\mathrm{keV}$), to allow sufficient sensitivity to all elements of interest. The beam full width half maximum, limiting the spatial resolution for these measurements, was $\sim 150\,\mathrm{nm}$. Films were measured in their initial state, throughout the high temperature process, and again in the final state. The data for the final films were corrected for absorption losses as described in Chapter 3.

CuInGa precursor films were co-sputtered on $2.5\,\mathrm{cm} \times 2.5\,\mathrm{cm}$ molybdenum coated soda lime glass substrates at the University of Delaware with a resulting average film composition of [Cu]/[In+Ga] (CGI) = 0.78 and [Ga]/[Ga+In] (GGI) = 0.22 measured by laboratory XRF. The metallic precursor layers were capped with $10\,\mathrm{\mu m}$ of evaporated selenium. The samples were then cut to $1\,\mathrm{cm} \times 1\,\mathrm{cm}$ prior to mounting in the *in situ* stage.

Figure 6.3 shows an example of a measured temperature time-temperature profile used during *in situ* CIGS film growth at a synchrotron beamline, compared to an industrially relevant process [40] that has produced 13 % efficient devices. The CIGS formation process starts with a fast ramp to $600\,^{\circ}\mathrm{C}$. This temperature is held for 25 minutes before the sample is rapidly cooled to room temperature. In some samples, the pure He inert gas flow was replaced by diluted H_2S (1 vol% in He) for the last 5 minutes at $600\,^{\circ}\mathrm{C}$. We are capable of achieving heating rates of $\sim 25\,^{\circ}\mathrm{C/s}$ and cool down from $600\,^{\circ}\mathrm{C}$ to $30\,^{\circ}\mathrm{C}$ in 3 minutes. This very high rate of heating and cooling gives us unique control over growth profiles and processing conditions.

Temperatures were measured using thermocouples connected to a Keithley 2701 data acquisition unit at 4 different locations in the stage throughout the process: at the graphite heater, in the fixed post that supports the sample, at the cooling water exit, and at the front plate.

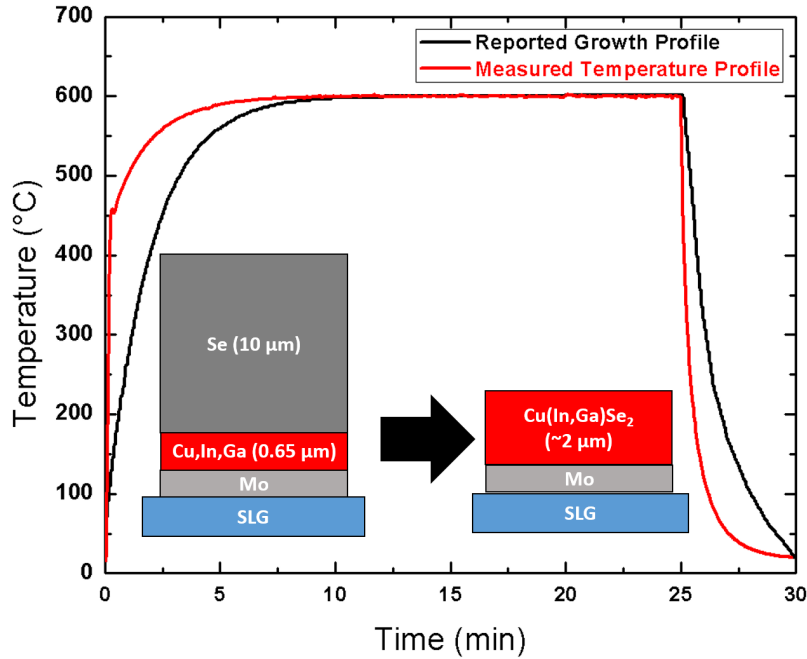Figure 6.3 Measured time-temperature profile from *in situ* growth stage (red) and profile (black) reported in [40]. The inset diagram shows the evolution of the sample stack before and after growth process.
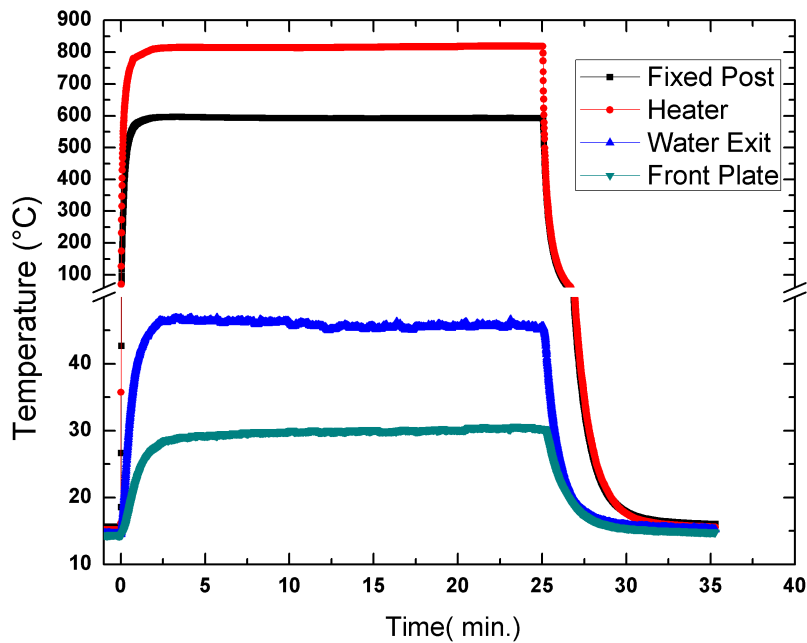
Figure 6.4 Time temperature profiles measured at 4 different locations during a temperature ramp. Fixed post is in direct contact with the edge of the CIGS sample and taken as the sample temperature.

These locations are shown in more detail in [163]. A typical time temperature profile for each thermocouple is shown in Fig. 6.4. Initial measurements utilized a PID controller to maintain a constant fixed post temperature. However, the reproducibility of ramp rates was limited and safety limits would sporadically cause rapid decreases in the supplied power, leading to non-ideal temperature control. To mitigate this, a the heater power output was manually set using LabView. The heater power required to achieve a desired sample temperature was termined by measuring a power-temperature calibration curve at the start of each experiment. The desired power profile at the Keithley 2260B-80-13 was set through LabView. As a result, more reproducible ramp rates were observed, and stable temperatures were achieved throughout the process.

Large thermal temperature gradients ($\sim 550\,°\mathrm{C}$ within $1\,\mathrm{mm}$ to $2\,\mathrm{mm}$) were observed between the sample and the front plate of the stage. The front plate needed to remain cool ($< 50\,°\mathrm{C}$) to protect the sensitive X-ray optics. A unique challenge arose due to this large temperature gradient. A non-negligible amount of selenium sublimed and condensed on both the front plate and the $50\,\mathrm{nm}$ thick Si_3N_4 window. Microscope images of the windows mounted on the front plate are shown Fig. 6.5. It is observed that a majority of the condensation occurred near the edges of the window, closer to the actively cooled front plate. Because the incident beam was positioned roughly in the center of the window, our measurements within a given run were relatively unaffected, as XRF maps of 'dirty' and 'clean' windows could confirm. Despite this test, it is still necessary to mitigate the selenium build up on the window, so the window had to be replaced after each run. This became cost prohibitive as Si_3N_4 X-ray windows are quite expensive, so we replaced the crystalline windows for found that Kapton® polyimide films that can withstand the high temperatures.
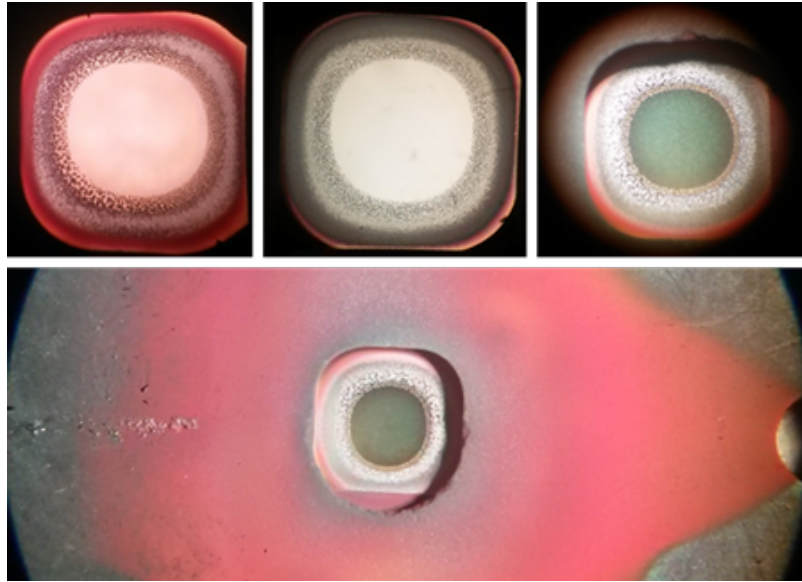
Figure 6.5 Microscope images of the $5\,\mathrm{mm}^2 \times 5\,\mathrm{mm}^2$ Si$_3$N$_4$ X-ray windows (top) and *in situ* stage front plate (bottom) showing condensation of selenium on the windows after high temperature processes.

6.3 Kinetics of Copper Segregation

The following study has been submitted for publication [165]. Figure 6.6 shows the composition evolution of a CIGS film from room temperature to $600\,^\circ\mathrm{C}$ over time. The synthesis process is described in Section 6.2. The left column of the figure shows the evolution of the selenium concentration over time. Rapid selenium evaporation is seen at the start of the heating process, and then the concentration remains constant for the rest of the growth. The right column shows the evolution of the Cu distribution, beginning before heating and ending after heating to $600\,^\circ\mathrm{C}$. Changes in the mass concentration are related to both stoichiometric and topological variations. At elevated temperatures the Cu distribution is highly non-uniform, showing copper rich and copper poor regions, and upon cooling the uniformity increases.

We are not only interested in the change in copper distribution over time, but also changes in indium and gallium, and the correlations between these elements. Figure 6.7 shows the
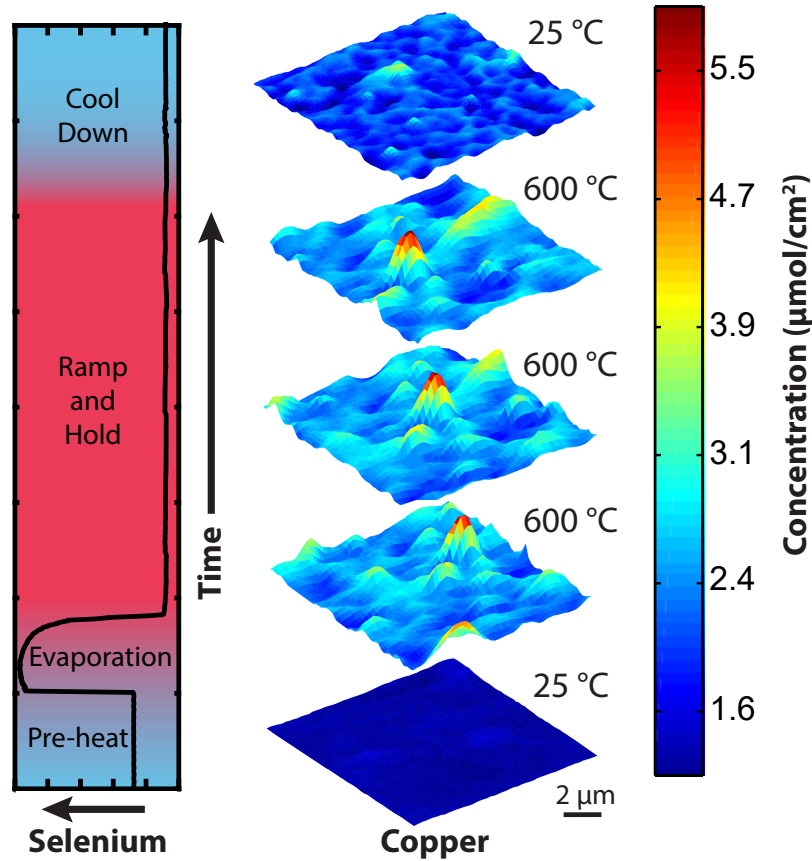
Figure 6.6 Left column: the selenium concentration in arbitrary units, over time during heating. The profile is divided into four regions, and shaded from blue to red corresponding to low and high temperatures. The pre-heat region is prior to a rapid temperature increase from $20\,°C$ to $600\,°C$. The rapid increase in selenium concentration during the evaporation stage is due an increase in Se concentration in the beam path. After evaporation the selenium concentration remains constant from ramp and hold through cool down. Right column: A $10\,\mu m$ x $10\,\mu m$ copper concentration map with $200\,nm$ step size showing the evolution of copper distribution during CIGS growth process. All maps are placed on the same color scale.
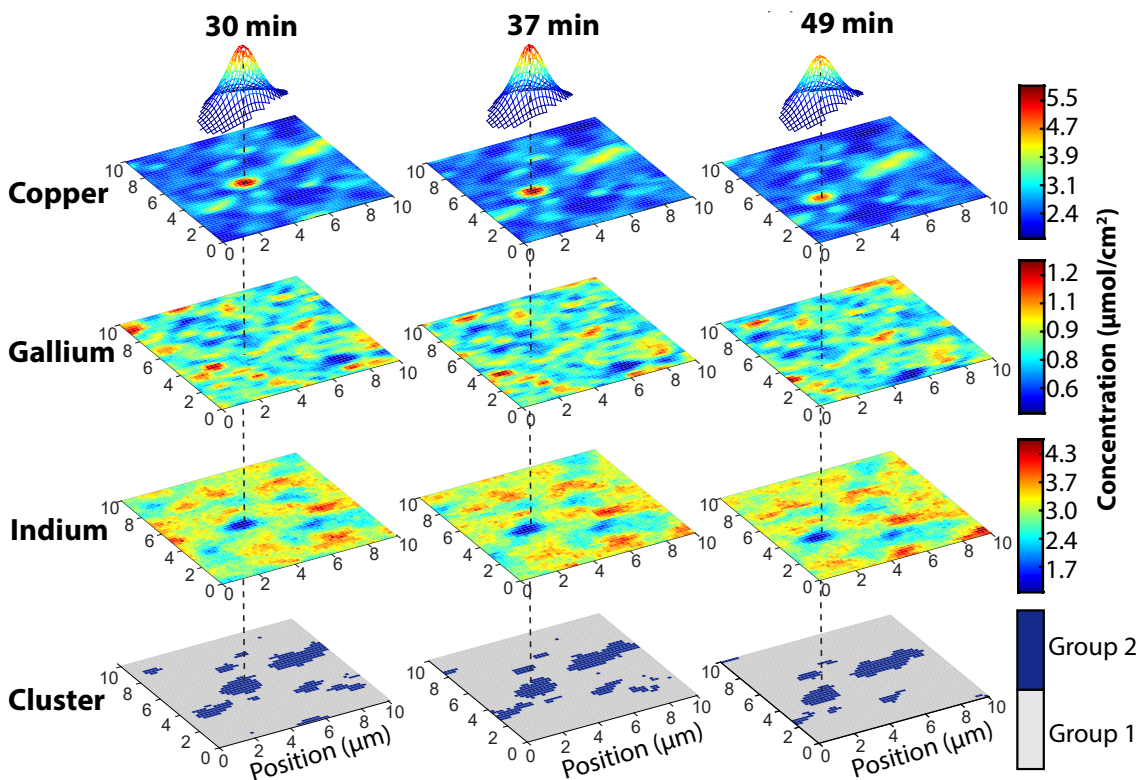
Figure 6.7 Spatial distribution of copper, indium and gallium concentration collected at 600 °C and 30, 37 and 49 min. The meshed peak above the copper maps is the result of a 3D Lorentzian fit of the copper rich particle seen in the top row. The dashed black line identifies the center of the copper rich particle and shows the same position on each of the other elemental maps. It can be seen that the copper rich region also corresponds to a decrease in indium concentration. The bottom row shows the result of a cluster analysis between copper, indium and gallium maps, identifying two unique compositional regions.

distribution of the Cu, In ,and Ga concentrations over time, with a distinct circular feature seen in the copper channel. This region correlates to a very low concentration of indium, and the features observed in the gallium map appear to anti-correlate with indium in some regions. One would tend to fit the circular feature to a 2D Lorenzian or Gaussian function to track the amplitude, width and center position over time. A Lorenzian fit is shown at the top of Fig. 6.7. From this fit we observed a decrease in amplitude and increase in the width over time. In this instance, the feature is easily identifiable, however by hand selecting the copper particle one

introduces inherent bias. One must make assumptions about, which data points are of interest, the shape of the particle, and requires a definition of the 'bulk' concentration. This analysis also neglects other features in the images that can exhibit similar or different behavior, and the overall behavior of the background.

How can data be compared across maps and experiments including multiple features and all data available? We approached this through the use of cluster analyses and classification algorithms [166], the result of which is shown in the last row of Fig. 6.7. The data was clustered to find two groups based on similarity in composition variations. Details on the analysis can be found in Chapter 7. Once the groups were identified in a representative map, a Naïve Bayes classifier was trained to label each pixel as a member of Group 1 or Group 2, for each map collected throughout the remaining times and temperatures, using the same set of classification criteria.

We identified a copper rich group (Group 2) with an average stoichiometry of $Cu_{1.1}In_{1.7}Ga_{0.2}Se_{2.0}$ and cooper poor group (Group 1) with an average stoichiometry of $Cu_{0.9}In_{2.0}Ga_{0.2}Se_{2.0}$. The selenium concentration was estimated from measurements collected above the selenium edge at $12.8\,keV$. We found that selenium is on average 65% of the cation concentration and the Ga/In ratio was lower than expected from the metallic precursors. We attribute these differences to element-specific evaporation rates. The unique stoichiometry of each group, is the result of the CIGS growth taking place in a mixed phase regime, and the large depth penetration of the X-rays. The composition of each group is based on the average composition with respect to the thickness, and the combination of three phases: α-CuInSe$_2$, In$_4$Se$_3$, Cu$_2$In [167]. Given the small Ga/In ratio ($\sim$ 10%) in our films, we approximate the quaternary CIGS phase diagram with the well-established ternary CIS phase diagram [168].

The CIGS phase was validated using XRD. Figure 6.8 shows the 2θX-ray diffraction scan of a CIGS film after annealing at $500\,°C$ for 25 minutes. A Phillips PanAnalytical High
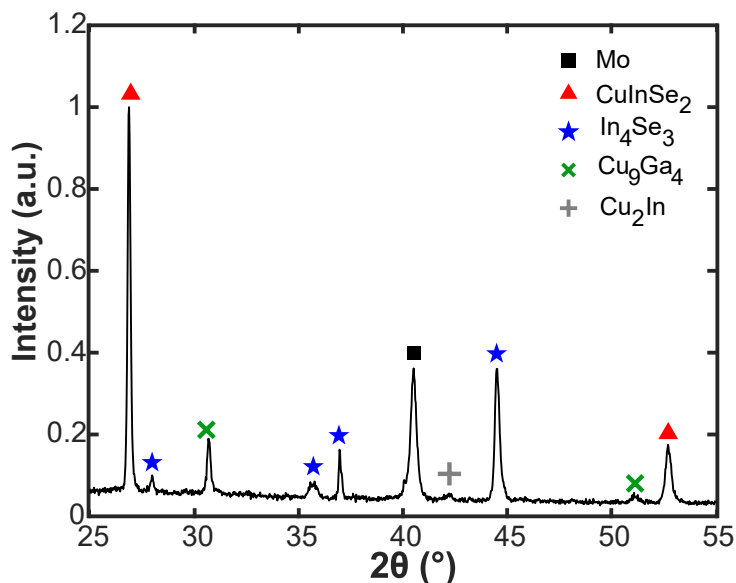
Figure 6.8 Powder X-rat diffraction scan of CIGS films annealed at $500\,°C$ at APS beamline 2-ID-D.

Resolution X-ray Diffractometer was used with a Cu- $K\alpha$ source. A nickel attenuator was used to suppress the contribution from the Cu- $K\beta$ transition. The presence of secondary phases is expected and in good agreement with the compositional analysis. The Mo substrate can be seen clearly at $\sim 40.5°$.

To investigate formation kinetics of each group and the rate of elemental segregation between Group 1 and Group 2, we heated separate samples to $500\,°C$, $550\,°C$ and $600\,°C$ for $25\,min$. We applied the previously described classification algorithm to each map to identify pixels belonging to either Group 2 (copper rich) or Group 1 (copper poor). Copper segregation was of greatest interest because it exhibited the largest variations and most significant trend over time. Elemental segregation between the groups was determined by plotting the difference between the average copper concentration in Group 1 and Group 2 over time, shown in Fig. 6.9 for each temperature measured. With increasing temperature from 500 to 550 and $600\,°C$, the

94
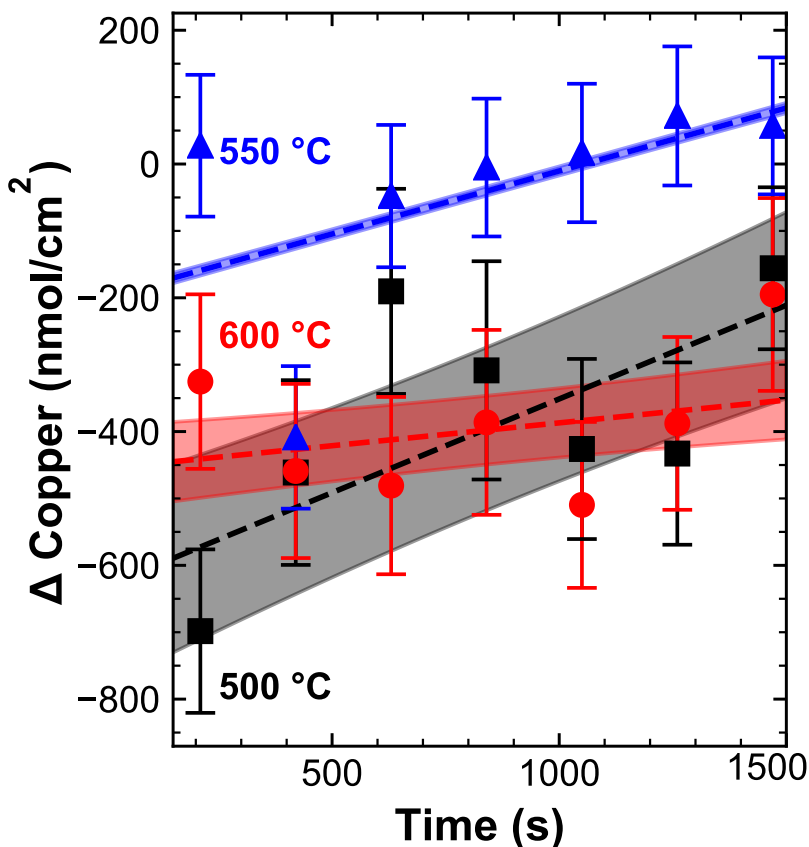
Figure 6.9 Difference in copper concentration between Group 1 and Group 2 over time, at $500\,°C$, $550\,°C$ and $600\,°C$. The dashed line is the result of a linear fit, weighted by the uncertainty on each datapoint. The shaded region are the 95% prediction intervals for the slope.

rate of change in copper concentration from Group 2 to Group 1 decreases in magnitude from $17\,nmol/(cm^2\,min)$ to $11\,nmol/(cm^2\,min)$ and $4\,nmol/(cm^2\,min)$. Contrary to what one expects from thermally activated processes we observe the molar flux of copper to decrease with increasing temperature. This indicates that the phenomena that we observe is not driven by thermal energy, but rather by changes in chemical potential, originating from micro-scale compositional variations.

In order to validate these results we investigated the pseudo binary phase diagram between In_3Se_2 and Cu_3Se_2, shown in Fig. 6.10. The black stars mark the average composition of the
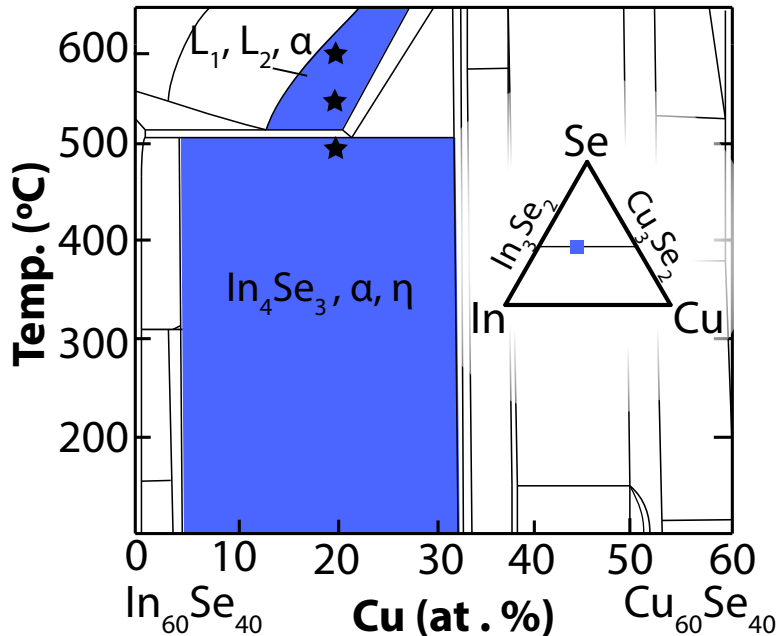
Figure 6.10 The pseduo-binary phase diagram along the In_3Se_2 - Cu_3Se_2 tie line. α-CIGS corresponds to the CIGS chalocpyrite phase. η phase is a Cu_2In compound. L_1 and L_2 are indium rich and copper rich liquid phases (respectively). The star markers identify composition regions where growth occurred. The subset shows the ternary Cu-In-Se phase digram with tie lines between In_3Se_2 and Cu_3Se_2. The square marker identifies the composition from which the pseudo-binary diagram was isolated. Data based on Gödecke et al. [167]

films at each temperature measured. The blue regions depict where the growth occurred, and it is clear that at $500\,^{\circ}C$ the composition of the film is within a mixed phase regime. Based on the average film stoichiometry, we estimate 70% α-CIGS and 30% In_4Se_3 for Group 2, and 45% α-CIGS and 55% In_4Se_3 for Group 1. Cu_2In is negligible in both cases based on stoichiometry. Using the temperature dependent Gibbs free energy according to ref. [169] for α-CIGS and ref. [170] for In_4Se_3, these constituent phases results in an estimated free energy of $-1089\,kJ/mol$ for Group 2 and $-902\,kJ/mol$ for Group 1. This difference in free energy creates a driving force for a net copper flow from Group 2 to 1 which supports our molar flux measurements at $500\,^{\circ}C$.

At $550\,^{\circ}C$, the material is in a different regime where α-CIGS is in equilibrium with two

liquid phases, L1 and L2 replacing In_4Se_3 and Cu_2In, respectively. With Group 2 having a higher copper concentration than Group 1, we attribute L1 to Group 1 and L2 to Group 2. The positive flow rate from Group 2 to 1 is likely due to the monotectic reaction between $L_1 \leftrightarrow L_2 + \alpha$ [167]. Why does the molar flux decrease with increasing temperature? At higher temperatures, the thermal equilibrium is reached quicker, leading to a smaller net flow from Group 2 to 1. Higher flow rates occur earlier during the RTP, which we were unable to quantify due to a combination of the initial substrate expansion and limited time resolution. At $600\,°C$ it is evident that there is no net flux of copper between the two groups, likely due to the fact that diffusion through liquids is much faster than solid state diffusion and the system has already reached equilibrium.

These studies show that copper is the driving force for phase stabilization in CIGS, more so than In, or Ga, indicating that controlling the copper concentration during growth would have the largest impact on the resulting material properties. We have shown that *in situ* XRF can be used to study the elemental diffusion in quaternary material systems with structural stability over a wide range of compositions. This opens up new avenues for materials engineering, where composition is the driver for material properties rather than structure. We are also able to study elemental segregation under real growth and industrially relevant processing conditions. One can imagine the potential for these studies to provide the necessary insight to control where and to what extent elements in any material system segregate during growth.

Future studies would be benefited by slower ramp rates and faster measurement acquisition times. While 3 minutes per map appears sufficient, in the current study, to capture the general trend during growth, it is well known that a series of reactions between elemental precursors take place prior to CIGS phase formation on time scales faster than 3 minutes [168, 169, 171]. Faster acquisition times enabled by next generation synchrotron light sources and beam lines [98, 172], could allow for the detection of changes between each rate limiting step and the

spatial and compositional dependence of these rates. It would allow for larger sample areas and smaller step sizes to provide greater statistics. Currently, only 1 - 2 copper rich particles are detected per map, contributing to the rather large confidence and prediction intervals shown in Fig. 6.9.

However, larger measurement areas, smaller step sizes, and more maps collected per minute will contribute to the complexity of the data set, highlighting even further the need for machine learning techniques to be used in the analysis. Along with the increased data sizes the inherent uncertainty in each of the data points and their resulting classification will need to be accounted for. Propagating experimental uncertainty through the clustering, with methods like fuzzy c-means, and filtering out data with large uncertainties, using non-deterministic classifiers, will result in a reduced uncertainty. Additional, error handling, and accounting for the 'fuzziness' of experimental data, will lead to better informed decisions based on the results.

These techniques offer the opportunity to unravel the kinetics that govern material processing. Applying these techniques to study precursor layers with varied composition and starting compounds, substrate templating, and varied time-temperature growth profiles will be of interest as well. Additionally material systems beyond CIGS, also dominated by fast growth, localized heating, and a high degree of functionality and property tuning, such as additive manufacturing, could highly benefit from this approach.

Chapter 7

MACHINE LEARNING FOR CORRELATIVE X-RAY MICROSCOPY

In the following sections, I describe the development and evaluation of machine learning algoritms used to handle the large amount of data generated from in situ measurements described in Chapter 6. I also I revisit data from the gallium investigations (Chapter 4 to evaluate the potential range and scope of the machine learning algorithms used here. These findings are also published in [173].

7.1 Evaluating the Impact of Sample Size

A challenge with these measurements is the trade-off between XRF map area, spatial resolution, and dwell time. The current optimized processes allows us to collect a $7\,\mu m \times 7\,\mu m$ map in $\sim 200\,s$. However, with this area, we only capture between 1 and 3 features per map. The small number of features, combined with substrate expansion and elemental segregation occurring on a time scale $<< 200\,s$, requires the use of clustering and classification techniques to compare features across maps. A goal of this study is to determine the necessary map size relative to feature size necessary to classify two unique composition regions in the XRF data.

7.1.1 Methods for Data Collection

XRF maps were collected at the Advanced Photon Source Beamline 2-ID-D, utilizing the temperature and ambient controlled *in situ* stage described previously. The incident beam energy was set above the Gallium K edge ($10.5\,keV$) to allow for sufficient sensitivity to all

cations, and the beam spot size was $200\,\mathrm{nm}$. The incident beam angle was $90°$, perpendicular to the sample surface, and the detector was $47°$ from the sample surface. The dwell time was $100\,\mathrm{ms}$. Fluorescence spectra were fitted against a well quantified standard using the MAPS package developed at APS, following the procedure described in Chapter 3. Due to the uncertainty in film thicknesses at elevated temperatures, the composition was not corrected for attenuation.

In order to isolate unique composition regions within the map, two classification techniques were implemented. An unsupervised Gaussian mixture model (GMM) was used to cluster the XRF composition data based on the probability that an individual pixel falls within one of two Gaussian distributions, whose centers are identified using the k-means method. The clustering is based on the expectation-maximization algorithm, wherein the likelihood that each pixel falls within a given distribution is maximized [174]. We also implemented a Naïve Bayes classifier, to predict whether a new data point falls into one group or another based on an initial set of training data. The classifier is based on Bayes' theorem that describes the probability of an event occurring based on prior knowledge of conditions related to that event. More information about Naïve Bayes and Gaussian mixture models can be found in [175]. Both models were implemented in Python using the Scikit-Learn package [166].

7.1.2 Unsupervised Clustering vs. Supervised Classification

To understand the difference between unsupervised machine learning (clustering) and supervised machine learning (classification algorithms), consider a set of 100 previously unknown songs, from which you want to separate the songs into genres of pop and classical music. Rather than listening to all 100 songs and labeling the songs by hand, you could search for unique features (variables) that are distinct between the two groups, like the number of

lyrics, or the year the song was produced. By plotting these two variables against one another, two distinct groups (clusters) should emerge in which, the data points that fall closest to one another belong to the same genre. By listening to one song from each cluster, the appropriate genre can be applied. This is unsupervised learning, because the genre of each song was previously unknown.

Once each of the data points have been labeled as either pop, or classical, a classification algorithm can be trained to assign a genre to any new song based on the number of lyrics and the year the song was produced. This is supervised learning because genre of each song in the input set was previously known.

In the case of *in situ* XRF data, the elemental segregation the film is unknown, requiring the use of a cluster analysis to separate the data into compositionally unique groups. This is done unsupervised using directions of maximum compositional variance (based on the principle components described in Section 7.2 as the appropriate features. In order to track changes in these groups over time, temperature, and across samples, a classification algorithm is used to label each pixel in each new map collected at specified time and temperature.
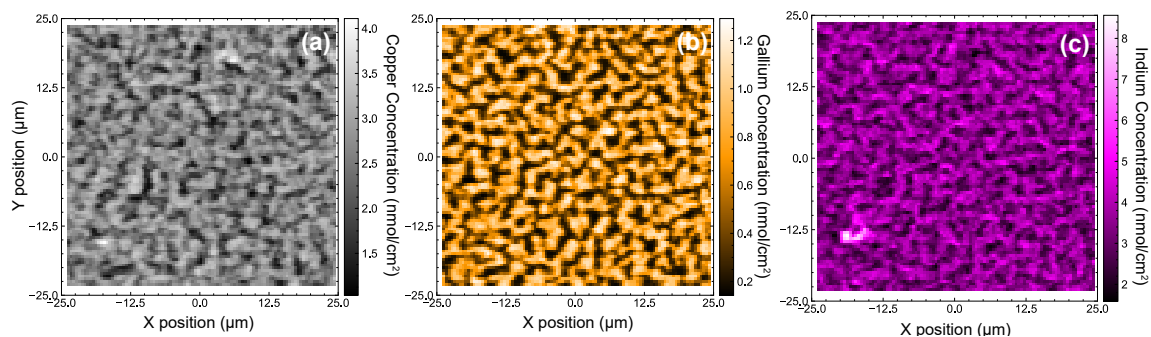
Figure 7.1 $47.5\,\mu m \times 49\,\mu m$ XRF maps of Cu (a), Ga (b), and In (c) with a $500\,nm \times 500\,nm$ pixel size taken at $300\,^{\circ}C$.

Figure 7.1(a-c) shows Cu, Ga, and In XRF maps, respectively, collected from the CIGS precursor stack, after $25\,min$, at $300\,^{\circ}C$. The total collection time for this map was ~ 50

101

min. The gallium and indium channels show a unique formation of islands not evident in the copper map. Indium shows a clear anti-correlation with the gallium channel which is expected, because they are substitutional in the CIGS lattice. The correlation with copper however is not intuitive. In some areas copper and gallium appear to correlate positively, in others negatively. This highlights the need for clustering, to separate these two regions, in order to be able to track each composition region throughout changing time and temperature. However, in some cases a 50 minute collection time is not practical, and smaller maps need to be taken, while still being representative of the larger map. In this case, the question is: what map size should be selected?

(a) 4 x 4 pixel² sub-map **(b) 12 x 12 pixel² sub-map** **(c) 25 x 25 pixel² sub-map**
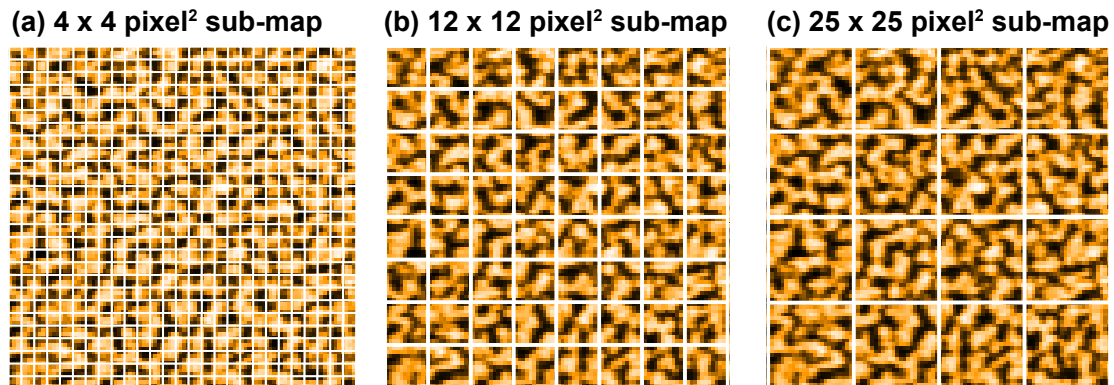
Figure 7.2 Diagram showing the differing submap sizes selected from the same image

To identify the necessary size of the input data set input data set, a moving box analysis was conducted on a large ($47.5\,\mu m \times 49\,\mu m$) XRF map. The map was divided into sub-maps of varying sizes ranging from 2x2 pixels, 4x4 pixels, etc. up to 30x 30 pixels such that a minimum of 9 sub-maps were extracted form the original map. Examples of sub-maps selected, relative to gallium feature size are shown in Fig. 7.2.

Two clusters within each submap were selected to ensure that each cluster is compositionally unique. More than two groups resulted in composition distributions that

were not isolated form one another. Because Naïve Bayes (NB) is a supervised technique, the model needs to be trained with an initial set of input data with corresponding labels, identified as the true case. The labels were taken from the GMM, that was applied to the bottom left sub-map closest to $(X,Y) = (-25\,\mu m, -25\,\mu m)$. As the sub-map size increases the size of the NB training data set also increases.
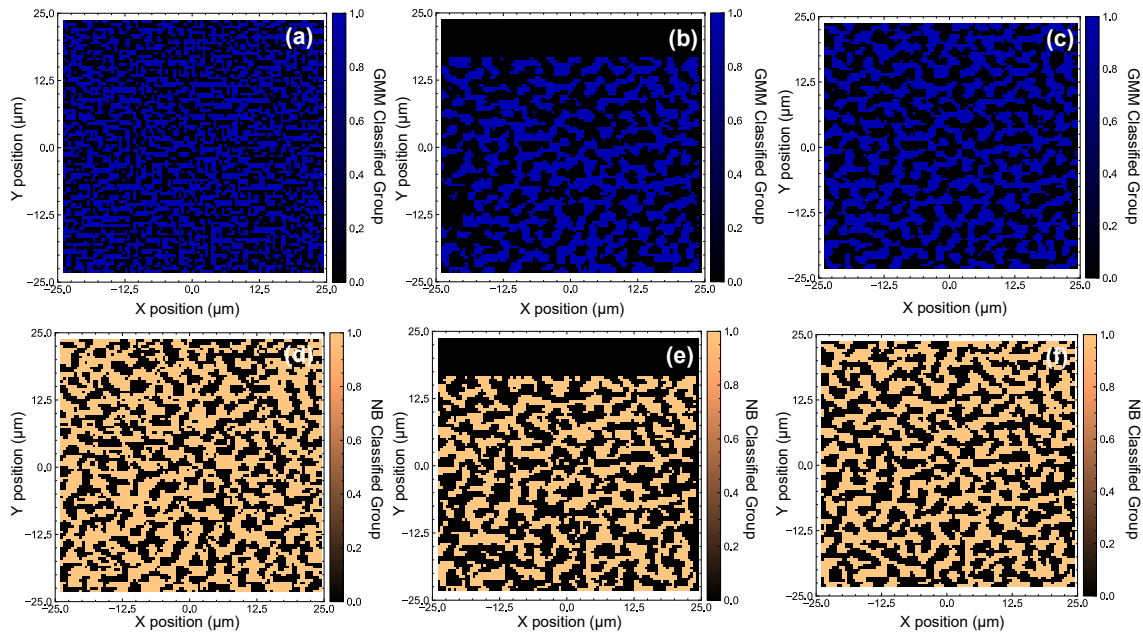
Figure 7.3 (a)-(c) Spatial distribution of the binary pixel classification using an unsupervised Gaussian-Mixture-Model for $1\,\mu m \times 1\,\mu m$, $8\,\mu m \times 8\,\mu m$, and $47.5\,\mu m \times 49\,\mu m$ sub-maps respectively. (d)-(f): Binary classification using a supervised Naïve Bayes (NB) model using the same sub-map sizes as (a)-(c). The entire map includes 9,310 pixels. The black bar in (b) and (d) at $Y > 17.5\,\mu m$ is due to the size of the sub-map, such that this area was not classified.

Figure 7.3 (a)-(f) shows the distribution of pixels classified either Group 0 or Group 1 based on the size of the sub-map using the GMM(a-c) or Naïve Bayes (d-f). Because the GMM is unsupervised, the model always finds two clusters within the sub-map, independent of the labels applied to previous sub-maps. This is evident in Fig. 7.3(a) where the size of the identified groups is much smaller than what can be seen by looking at the XRF maps (see also

103

Fig. 7.2(a)). Interestingly the same sub-map size, classified using NB (Fig. 7.3d), identifies groups much closer to what can be seen from the XRF maps. This is because rather than always identifying two clusters in each map, it labels each pixels based on the probability that it belongs to one group or another. Additionally, in this particular case it is likely that the initial training set for the NB model included pixels that belong to both groups (based on the final map). This correlation between the smallest sub-map and the final map would change if the entire training set belonged to Group 0 or Group 1. This can lead to entire maps being classified as Group 0 or Group 1. This makes the process highly repeatable and increases the similarity between the classified pixels. As the sub-map size increases Fig. 7.3(b,e), the groups identified by each method converge, and are more representative of the features apparent from the XRF map. The rectangular area at $Y > 17.5 \, \mu m$, is due to the size of the sub-map selected. An additional 16 pixel x 16 pixel sub-map would not fit entirely in this region, and for this reason it was unclassified. Figure 7.3(c,f) show the classification of the entire XRF map using GMM and NB respectively. If the training set used is not representative or dissimilar from the test data set, this can lead to a large uncertainty in the classification. This will be discussed further in Section 8.4.

Figure 7.4 shows the distribution of the mean composition of each group as a function of the sub-map size (moving box length). Atomic percentages are calculated by dividing each element by the sum of all cations (Cu, In, Ga) for a given pixel. The mean composition was calculated from the composition of the pixels identified as Group 0 or Group 1 for both GMM (Fig. 7.4 a-c) and NB (Fig.7.4 d-f). It can be seen that, as the sub-map length increases, the variance in the average group composition decreases. Note also that as the sub-map length increases the number of sub-maps decreases, leading to a smaller sample size N. For 2 pixel by 2 pixel map, N = 2303, for 10 pixel x 10 pixel, N = 81, and for 30 pixel x 30 pixel, N = 9. The smallest sub-map size (2 pixel x 2 pixel) does not succeed in identifying compositionally
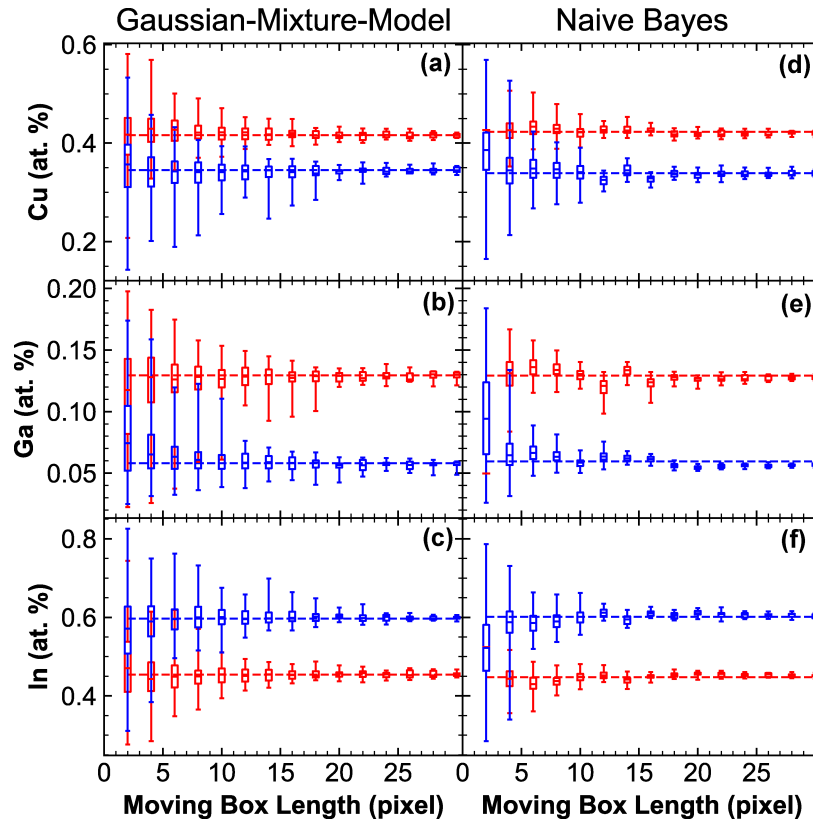
Figure 7.4 Box plots showing the distribution of average copper, indium and gallium composition for each group, identified using a Gaussian mixture model(a)-(c), and a Naïve Bayes model (d)-(f). Top, middle and bottom of the box represent the 75, 50, and 25 percentiles respectively. The edge of the whiskers are the maximum and minimum of the sample set. The red group corresponds to Group 0 from Fig. 7.3, and the blue group corresponds to Group 1. The dashed lines represent the average composition of each group when the entire map is clustered using the Gaussian mixture.

unique groups, for either model, with an observable overlap of the whiskers of each groups box plot. This indicates that a 2 pixel x 2 pixel map is not sufficient to describe the data. While the GMM results in a similar variance for both groups, NB results in Group 0 having a very small distribution and Group 1 having a very large distribution. In our application, we seek to determine the smallest submap size for which the box plots no longer overlap and the groups can be clearly distinguished from each other. This identifies the minimum map size necessary to identify compositionally unique groups. If the features observed in the map are not similar
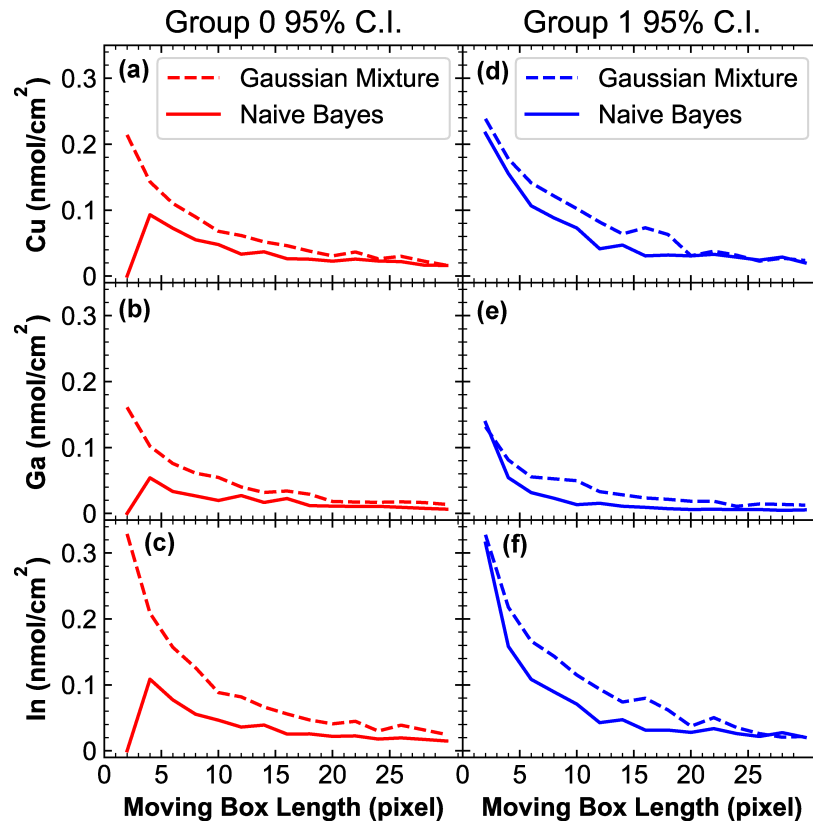
Figure 7.5 Confidence Intervals for average group composition as a function of sub-plot length. Dashed lines are the confidence intervals corresponding to the Gaussian mixture model, and solid lines correspond to the Naïve Bayes classifier. (a-c) compares the confidence intervals for Group 0 across Cu, Ga, and In respectively. (d-f) compares the confidence intervals for Group 1

in size across all elements, this could lead to more than two groups being identified, and require more training data to identify the clusters. For NB this critical size is different for each of the elements. One can see that fewer data points are necessary to classify unique groups using a NB model, than a GMM. It is also interesting to note that with a feature size of $\sim 5\,\mu\mathrm{m}$, only 1 - 2 features are necessary to classify the data. The requirement of smaller map sizes for NB than GMM becomes even more apparent if a larger number of clusters is identified. More data will be necessary to accurately identify each new subgroup.

To better visualize the difference between the two models, Figure 7.5 shows the 95 %

confidence interval (C.I.) for the average group composition for Cu, Ga, and In for both classification methods. As the sub-map size increases, the confidence interval decreases for both cases and all elements. It is interesting to note that for the 2 pixel x 2 pixel sub-map, the Group 0 NB classifier has the narrowest confidence interval. This corresponds to the narrow distribution observed in Figure 7.4 (d-f), likely due to the small data set that was used to train the model, which resulted in narrow composition regions for Group 0. For Group 1, both NB and GMM have similar C.I. across all elements. Between the sub-map length of 4 and 20 pixels the NB classifier out performs the GMM, with a smaller C.I. for the average group composition. For sub-maps larger than 20 pixels, both models perform similarly.

Another parameter that is important when comparing these models, is the fraction of pixels attributed to Group 0 and Group 1. Figure 7.6 shows the distribution of these fractions as a function of sub-map length for both models. At small sub-map sizes, we note for both models a wide distribution that overlaps between the two groups. The dashed lines in each plot represent the group fraction based on clustering the entire XRF image. With a sub-map length > 20 pixels or $10\,\mu\text{m}$, NB begins to converge on the 'true' ratio of Group 0 and Group 1.The GMM model converges on the average, as would be expected, but the distribution is very wide, leading to higher uncertainty than the NB model.

7.1.3   Summary

In this study we showed the potential for machine learning techniques to be applied to *in situ* XRF data to interpret a 9,310 pixel map of 3 separate elements, as two classes of pixels. To understand the strengths and limits of this approach, we compared an unsupervised Gaussian mixture model and a supervised Naïve Bayes classifier. For smaller sample sizes the supervised NB classifier out performed the unsupervised GMM. However, as the sample
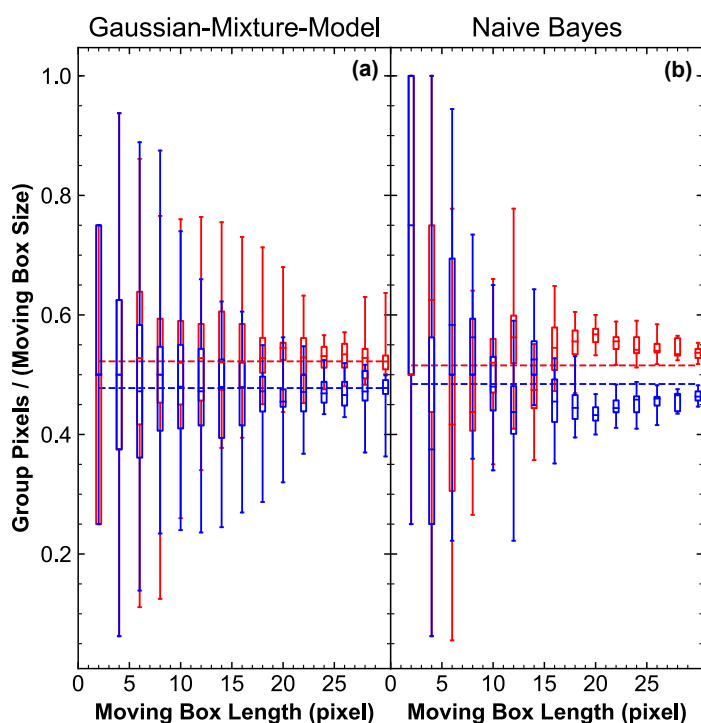
Figure 7.6 the distribution of the number of pixels identified per group (Red = Group 0, Blue = Group 1) relative to sub-map size. The dashed line represents the 'true' group concentration based on a full XRF map clustering. Top, middle and bottom of the box represent the 75, 50, and 25 percentiles respectively. The edge of the whiskers are the maximum and minimum of the sample set.

size increased, the two models converged. The NB classifier was also able to predict the fraction of each group with less data, and with a smaller maximum-minimum spread than the GMM. More specifically, we were able to determine that the NB classifier is able to identify compositionally unique groups from a map size $5\,\mu m \times 5\,\mu m$, which is on the order of the feature size. The unsupervised GMM required an input map size of at least $7\,\mu m \times 7\,\mu m$ for the same feature size. In the following section, we will apply these methods, to understand elemental segregation during CIGS growth. Understanding the relationship between feature

size and map size, enables us to not intervene when dealing with data that has features moving and changing shapes.

7.2 Revisiting the Watershed Analysis

The results from the *in situ* growth study described in Section 6.3, showed the potential for machine learning techniques to separate XRF data into unique compositional groups based on variance within the data. In an effort to validate these results and the algorithms used, I revisited the data presented in Chapter 4. In the previous study we used a watershed analysis to separate the XRF data into regions of grain cores and grain boundaries for two CIGS devices with varying gallium concentrations. We found that grain boundaries tended to be copper and gallium rich. While in low gallium devices this correlated with increased current collection, in high gallium devices grain boundaries under performed with respect to grain cores.

How would these results vary if a cluster analysis was used to segment the data rather than the watershed method? Can machine learning techniques be used to identify grain boundaries in these films without the need for user input? The use of the watershed method has the potential to introduce bias, because a blurring threshold is applied manually and final approval of the watershed image is done by eye. We have shown that there is good agreement between the watershed applied to an XRF image and a corresponding back scattered SEM image of the same spot.

Figure 7.7 shows a comparison between a copper XRF map (Fig. 7.7a), the corresponding watershed analysis (Fig. 7.7b), and label map generated from the cluster analysis (Fig. 7.7c). The uncorrected copper map represents the topology of the film, with the low concentration regions correlating with a thinner region of the map. It can be seen that the watershed (used to identify grain boundaries), correlates with the lower concentration regions very well.
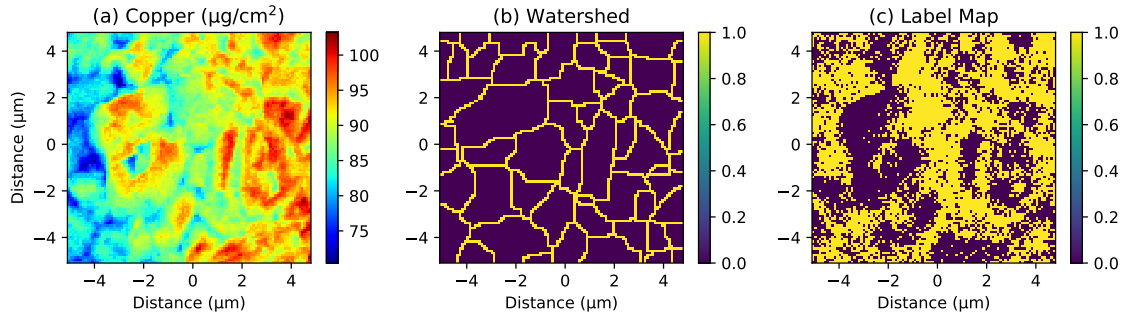
Figure 7.7 (a) $10\,\mu\mathrm{m} \times 10\,\mu\mathrm{m}$ Copper XRF map of low gallium CIGS cell described in Chapter 4. (b) Corresponding watershed map identifying grain boundaries in map, value of 1 is grain boundary. (c) Label map generated from cluster analysis. Color scale corresponds to group number.

To generate the label map multiple data processes steps were used. Absorption corrected and thickness normalized atomic ratios of copper, gallium and indium were placed in a column matrix X with the shape $[N \text{ x } p]$ where N is the number of pixels in the XRF map, and p is the number of elements of interest (in this case $p = 3$). The matrix X was then centered and normalized such that the average along each column equals zero and the standard deviation of each column equals 1. These steps are important to not weight the data in favor of elements that are more abundant (like indium or copper) or data that varies over a wider range. What is of interest in this study is the relative changes in distribution between the elements.

A principal component analysis (PCA) on X was conducted. PCA projects the data along axes of greatest variance and is often used to reduce the number of dimensions in the data and eliminate highly correlated features. This is accomplished by an eigenvalue decomposition of the covariance matrix of X. Equation 7.1 describes the covariance of data matrix X between variables j and k (in this case element j and element k). This also highlights the importance of centering the data around 0, as it is a necessary step for calculating the covariance. Equation 7.2 shows the calculation of covariance of an entire matrix by multiplying a matrix by its

transpose. $N - 1$ is used rather than N because the true mean of the population is unknown and is estimated based on the sample mean.

$$X_{jk} = \frac{1}{N-1} \sum_{i=1}^{N} (X_{ij} - \bar{X}_j)(X_{ik} - \bar{X}_k) \tag{7.1}$$

$$X_{cov} = \frac{X_{\mu=0} * X_{\mu=0}^T}{N-1} \tag{7.2}$$

Equation 7.3 shows the eigendecomposition of the covariance matrix X_{cov} into a matrix of eigenvectors ν and eigenvalues λ. The eigenvectors are the orthogonal directions of greatest variance, and the eigenvalues are their corresponding magnitude (ie: the largest eigenvalue corresponds to the direction of greatest variance, and in this case the first principal component). The product of data matrix X and the eigenvector matrix ν is the linear projection of the data along the direction of maximum variance. More information about eigendecomposition is available in [176].

$$X_{cov}\nu = \lambda\nu \tag{7.3}$$

Figure 7.8 shows the results of the principle component analysis applied to the same XRF map shown in Fig. 7.7(a). It can be seen that the first two principle components show unique features and account for orders of magnitudes greater variance than the third principle component. This also highlights the potential for PCA to reduce noise in the data similar to an approached used to fit XRF spectra described by [127]. Based on this analysis the first two principal components were selected, which describe > 99% of the variance within the data.

The data were then clustered into two groups, to mimic the identification of grain cores and grain boundaries utilized previously. Similar to Section 7.1.1, a Gaussian Mixture Model was applied to the first two principle components. The label map shown in Fig. 7.7(c) is the resulting classification of each pixel. The pixel classifications for the large ($10\,\mu\text{m} \times 10\,\mu\text{m}$)
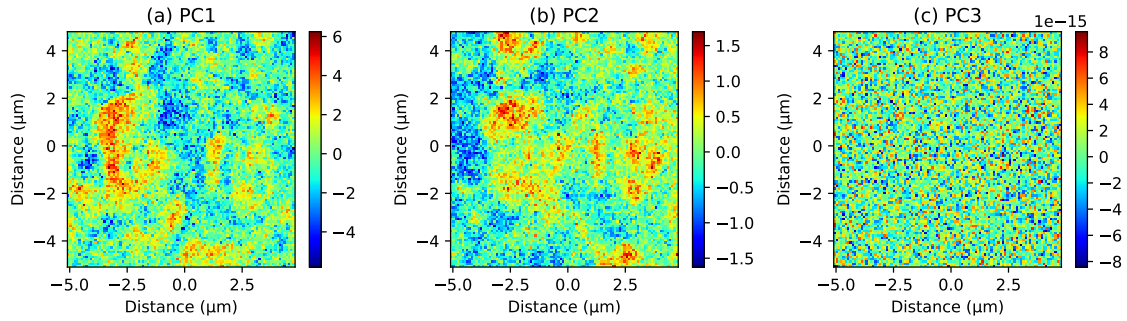
Figure 7.8 Principle Component Maps

overview map were then used to train a Naïve Bayes classification algorithm, to apply the same set of "rules" for classifiying pixels in the smaller $2\,\mu m \times 2\,\mu m$ high resolution maps of the grain boundaries. The classification algorithm was used to label 10 maps each containing 2500 pixels for the low gallium device and 7 maps containing 1600 pixels for the high gallium absorber.

Table 7.1 Clustered group composition and comparison with watershed analysis

	Low Gallium	High Gallium
Group 1 CGI	88%	99%
Group 2 CGI	83%	95%
Group 1 GGI	36%	70%
Group 2 GGI	32%	66%
Group 1 XCE	95%	44%
Group 2 XCE	92%	45%
Group 1 Pixels on GB	**76%**	**64%**
Group 1 Pixels on GC	**27%**	**31%**

The results of the clustering analysis were found to be in good agreement with the results obtained from the watershed analysis from Chapter 4 and are summarized in Table 7.1. Interestingly, the composition of the two groups identified are in line with the composition of the grain boundaries and the grain cores identified previously. Group 1 had a higher copper and gallium concentration than Group 2 in both low and high gallium films. Interestingly the

difference between the two groups was observed to be greater than the differences measured between the grain boundaries and grain cores. For the low gallium film the copper and gallium rich group also exhibited increased collection efficiency measured by XBIC. This was not the case for the high gallium absorber, where the copper and gallium poor group showed a slightly higher collection efficiency.

It was also important to determine the locations of pixels identified as Group 1 or Group 2 to check they are in agreement with grain boundaries and grain cores identified form the watershed analysis. These results are shown in the bottom two rows of Table 7.1. It can be seen that, for the high gallium absorber 76% of all the pixels identified as grain boundaries were labeled as Group 1 (copper and gallium rich), and only 27 % of Group 1 pixels were located on regions identified as grain cores. The grain boundaries in the high gallium film also have a larger percentage of Group 1 pixels than grain cores, but this difference is smaller than for the low gallium film. This also supports the findings in the previous study that there is a smaller difference between grain boundaries and grain cores in high gallium films, because there are fewer Group 1 pixels on the grain boundaries.

These findings can also be used as a validation for the machine learning techniques used in the study of copper segregation during growth. These unsupervised techniques were used to find the same composition variations that were identified from significant input from the researcher and prior knowledge of the samples. However, this also highlights a challenge associated with unsupervised machine learning techniques. How does one bridge the gap between arbitrary group labels (1 or 2) and something more meaningful labels (ie: grain cores and grain boundaries). Unsupervised techniques should not be used alone, and in both cases presented in this chapter, were supported by other analysis/approaches.

Chapter 8

CONCLUSIONS AND RECOMMENDATIONS FOR FUTURE WORK

The purpose of this work was to investigate the impact and origin of inhomogeneities in $CuIn_{1-x}Ga_xSe_2$ thin film solar cells. The unique tunability and inherent inhomogeneity of the composition in this system, mainly in terms of the [Ga]/[Ga+In] and [Cu]/[Ga+In], presents unique challenges [19, 70, 72] and opportunities [22, 57, 90, 165].

Based on these studies we found that the distribution of copper plays a critical role in the electrical properties of CIGS absorber layers as well as during absorber layer growth. Copper rich grain boundaries were determined to correlate with increased X-ray collection efficiency (XCE) in absorber layers with 30 % gallium addition. In absorber layers with 60 % gallium addition, a negligible change in the average copper concentration was observed at the grain boundaries compared to grain cores and the correlation between copper concentration and XCE was just above the detection limits. Copper was also determined to segregate the quickest during growth as well as being a driver for secondary phase formation.

It was also determined that the decrease in performance of high gallium absorber layers could be related to multiple factors, including a bi-modal distribution in grain sizes. It was observed that smaller grains under performed compared to larger grains. Grain boundaries under performed on average compared to grain cores in high gallium absorbers. Additionally, the copper concentration varied less compared to low gallium absorbers. The NaF post deposition treatment was determined to have a negligible impact on composition variations, but a large impact on variations in the bandgap measured by photoluminescence. It was determined that reduction in electrostatic potential fluctuations is likely to contribute to the increase in V_{oc} and FF observed.

Moving forward there are multiple avenues to improve upon the characterization framework developed thus far and discussed in the previous chapters.

8.1   Attenuation Corrections

Chapter 3, describes the experimental methodology used to correct for X-ray attenuation losses in multi-layered structures. This analysis makes several assumptions that can be improved for increased accuracy and broader applicability to other materials and layer stacks. These assumptions include:

- Fixed layer thickness
- Fixed film composition
- Negligible secondary fluorescence

The fixed layer thickness is acceptable for CIGS films and was estimated to contribute $\sim$ 10% uncertainty to the correction. This is due to the surface roughness of typical films ranging from $\sim 100\,\mathrm{nm}$ to $200\,\mathrm{nm}$. This will increase for films with larger surface roughness, and for different measurement geometries, particularly geometries that create longer path length for the incident beam and/or exiting fluorescence.

For the CIGS films under study we showed that depth dependent composition variations had a negligible impact on the correction factor. Thus, assuming a fixed absorber layer composition used for calculating the materials attenuation coefficient (μ), was acceptable for these films but may not hold true for other material systems, for example, metal nanoparticles in a polymer matrix, or materials with strong phase segregation.

Both of these assumptions can be mitigated by implementing an iterative approach to the correction. Using elemental concentration on a pixel by pixel basis to calculate a unique attenuation coefficient, and estimate the thickness across the entire map is an important step.

Using this information in combination with the measurement geometry would allow one to use information from the surrounding pixels to correct the current pixel. This process will be repeated iteratively until the correction converges.

Assuming negligible contribution of secondary fluorescence introduced an estimated ∼5% uncertainty in XRF quantification, based on calculations conducted by Mainz and Klenk on CIGS films [177]. Implementation of a calculation similar to that described by [178] would reduce the uncertainty and allow for this method to be applied to a wider range of materials.

All of the additions described above would not only benefit the corrections used for X-ray fluorescence data, but corrections for X-ray beam induced current data as well.

8.2   Correlative Operando Microscopy

In Chapter 4, correlative operando microscopy was used to investigate composition variations between grain cores and grain boundaries and their effect on local carrier collection efficiency. The following are areas for improvement from the current study:

- Correlation of XBIC results to full device parameters, especially the evaluation of dark current effects, when local illumination corresponds to high minority carrier density
- Implementation of XBIV to investigate the effects of composition variations on voltage
- Measuring XBIC and XBIV under light bias and at elevated temperatures to replicate real operating conditions.

The implementation of temperature dependent XBIV [91] and bias dependent XBIV have been conducted [110], however correlating composition variations with XBIV is still on going. The introduction of light, bias and temperature enables characterization of current and voltage characteristics of solar cells under real operating conditions. XBIV however has difference challenges than those associated with XBIC, as described in [110] and shown in Fig. 2.15.

116

Due to the logarithmic dependence of voltage on injection level, it can be unclear from XBIV alone if a positive ΔV corresponds to a good or poor performing region. This highlights the importance of combining XBIV and XBIC for evaluating cell performance.

In Chapter 5, photoluminescence microscopy was used to investigate the impact of Na concentration on bandgap fluctuations in CIGS devices. PL microscopy also lends itself toward operando measurements. Studies thus far however have yet to reveal correlations between PL peak center, position, or width, electrical properties (current or voltage). Given the known dependence of V_{oc} on bandgap described in Equation 2.3 and 2.4, this has been surprising, as well as reports of the importance of bandgap fluctuations in these devices [70, 72]. This could be due to the very high injection levels induced by the laser used for these measurements, changing the dominant recombination mechanism. Investigating the injection dependence of the current and voltage characteristics will be important for enabling operando PL microscopy.

8.3   In Situ X-ray Fluorescence Microscopy

In Chapter 6 the design and implementation of a heating stage for *in situ* XRF measurements was discussed. The stage is capable of achieving temperature ramp rates $> 300\,°C/\text{min}$ and vibration stability $< 200\,\text{nm}$, and the atmospheric control to inert and corrosive gasses such as H_2S and H_2Se. The application of *in situ* XRF to study the growth of CIGS absorber layers via a rapid thermal growth process was also discussed. In situ XRF is ideal for studying growth kinetics of materials with structural stability over a wide composition range like CIGS. Learnings from these studies will lead to next generation *in situ* stage design, as well as new *in situ* growth studies.

The next generation XRF stage should be designed to ensure the ease of use for a broader range of samples, and include more flexible measurement geometries. The quartz flexures used

currently allow for substrate expansion, but are very brittle, and make the process of sample exchanges very time consuming. A new, more flexible sample mount, should be designed to allow for samples with variable sizes rather than the fixed $1\,\text{cm} \times 1\,\text{cm}$ that is currently utilized, and increase the speed of sample changes. Additionally, utilizing a curved X-ray transparent front plate , possibly made out of Kapton, will enable broader range of measurement geometries, and the use of additional detectors for other measurements, like XRD. However, the specifications met by the current stage will need to be carried over in any new design iterations.

The next generation of CIGS growth studies utilizing the *in situ* stage should be geared towards tuning, heating and cooling rates, investigating alternative precursor layer stacks, and investigating CIGS layers with varied gallium concentrations. In the study described in Chapter 6, it was observed that the cation/anion ratio was greater than the 1:2 expected for CIGS. This was attributed to the rapid heating rates leading to excess selenium evaporation. Slower heating rates should be investigated to improve selenium evaporation rates during growth. Additionally, altering the compounds used in the precursor stack from elemental Cu,In,Ga, and Se to selenides ($CuSe_2$, Ga_2Se_3, In_4Se_3), could reduce the selenium lost to evaporation during growth. It would also be of interest to investigate copper segregation as function of precursor compounds and stoicheometry to better control the rate of copper segregation. These studies can lead to investigations of patterned substrates to promote copper segregation to desired regions, such as grain boundaries.

8.4 Data Analytics and Machine Learning

In Sections 7.1.2 and 7.2, machine learning techniques are applied to identify unique composition regions in XRF maps of CIGS absorber layers, both during growth and in

completed devices. It was shown that unsupervised learning techniques including clustering with Gaussian Mixture Models can be validated, using a watershed analysis (which correlates grain boundaries) and pseudo-binary phase diagrams. It is interesting to note that the directions of largest variance within the data, identified statistically, are also the trends identified with significant input from the researcher. A moving box analysis was also used to compare the minimum size of the data set necessary to identify two groups of unique composition.

While PCA, GMM, and NB classifiers proved useful for the studies described herein, the same approach may not be well suited future studies. It is important to consider the assumptions built into these methods. PCA assumes that the directions of maximum variance in the data are linear. A built-in assumption in Naïve Bayes classifiers are that features are independent. When using GMM it is assumed that the clusters being identified can be described accurately by a Gaussian distribution, and is limited by the number of groups identified by the researcher. Evaluating each of these assumptions and using the 'right tool for the job' is critical.

The analyzes described herein can be improved by propagating experimental uncertainty through the clustering. The uncertainty in the indium channel, for example, is greater than that for copper and gallium (shown in Section 4.2). Using methods like fuzzy c-means, where data points are weighted based on their uncertainty prior to clustering. Additionally, uncertainty in the clustering analysis can be accounted for by using non-deterministic classifiers. In this case, data points with large uncertainties can be ignored and not assigned to either 'group'. As with any analysis, it is important to validate of the classification and clustering algorithms. Machine learning techniques can 'cluster an elephant', so to speak, so ensuring that the results of the analysis are what they seem to be, is critical. Methods of validation used in this work are described in Sections 6.3, 7.1.2, and 7.2.

This additional error handling, accounting for the 'fuzziness' of experimental data, and validation, can lead to better informed decisions based on the results.

REFERENCES

[1] M. Z. Jacobson, M. A. Delucchi, Z. A. Bauer, S. C. Goodman, W. E. Chapman, M. A. Cameron, C. Bozonnat, L. Chobadi, H. A. Clonts, P. Enevoldsen, J. R. Erwin, S. N. Fobi, O. K. Goldstrom, E. M. Hennessy, J. Liu, J. Lo, C. B. Meyer, S. B. Morris, K. R. Moy, P. L. O'Neill, I. Petkov, S. Redfern, R. Schucker, M. A. Sontag, J. Wang, E. Weiner, and A. S. Yachanin, "100% Clean and Renewable Wind, Water, and Sunlight All-Sector Energy Roadmaps for 139 Countries of the World," *Joule*, vol. 1, no. 1, pp. 108–121, 2017.

[2] R. E. Smalley, "Future Global Energy Prosperity: The Terawatt Challenge," *MRS Bulletin*, vol. 30, no. 06, pp. 412–417, 2005.

[3] M. Z. Jacobson, M. A. Delucchi, G. Bazouin, Z. A. F. Bauer, C. C. Heavey, E. Fisher, S. B. Morris, D. J. Y. Piekutowski, T. A. Vencill, and T. W. Yeskoo, "100% clean and renewable wind, water, and sunlight (WWS) all-sector energy roadmaps for the 50 United States," *Energy Environ. Sci.*, vol. 8, no. 7, pp. 2093–2117, 2015.

[4] R. Jones-Albertus, D. Feldman, R. Fu, K. Horowitz, and M. Woodhouse, "Technology advances needed for photovoltaics to achieve widespread grid price parity," *Progress in Photovoltaics: Research and Applications*, vol. 24, no. September 2016, pp. 1272–1283, 2016.

[5] Department of Energy, "The SunShot Initiative : Making Solar Energy Affordable for All Americans," 2016. [Online; accessed 15-December-2017].

[6] Department of Energy, "R & d will include focus on reliability, resilience, and storage," September 2017. [Online; accessed 5-December-2017].

[7] M. Munsell, "GTM Research: 20 US States at Grid Parity for Residential Solar," February 2016. [Online; accessed 5-December-2017].

[8] D. M. Powell, M. T. Winkler, H. J. Choi, C. B. Simmons, D. B. Needleman, and T. Buonassisi, "Crystalline silicon photovoltaics: a cost analysis framework for determining technology pathways to reach baseload electricity costs," *Energy & Environmental Science*, vol. 5, no. 3, p. 5874, 2012.

[9] S. Kurtz, H. Atwater, A. Rockett, T. Buonassisi, C. Honsberg, and J. Benner, "Solar research not finished," *Nature Photonics*, vol. 10, no. 3, pp. 141–142, 2016.

[10] S. Kurtz, N. Haegel, R. Sinton, and R. Margolis, "A new era for solar," *Nature Photonics*, vol. 11, no. 1, pp. 3–5, 2017.

[11]   K. P. Bhandari, J. M. Collier, R. J. Ellingson, and D. S. Apul, "Energy payback time (EPBT) and energy return on energy invested (EROI) of solar photovoltaic systems: A systematic review and meta-analysis," *Renewable and Sustainable Energy Reviews*, vol. 47, pp. 133–141, 2015.

[12]   Fraunhofer Institute for Solar Energy Systems, "Photovoltaics report," tech. rep., Freiburg, Germany, 2014.

[13]   M. Stoppa and A. Chiolerio, "Wearable Electronics and Smart Textiles: A Critical Review," *Sensors*, vol. 14, pp. 11957–11992, 2014.

[14]   S. Hegedus, "Thin Film Solar Modules: The Low Cost, High Throughput and Versatile Alternative to Si Wafers," *Progress in Photovoltaics: Research and Applications*, vol. 14, pp. 393–411, 2006.

[15]   S. Pearton, J. Corbett, and T. SHI, "Hydrogen in crystalline semiconductors," *Journal of Applied Physics*, vol. 43, no. 3, pp. 153–195, 1987.

[16]   C. Li, Y. Wu, J. Poplawsky, T. J. Pennycook, N. Paudel, W. Yin, S. J. Haigh, M. P. Oxley, A. R. Lupini, M. Al-Jassim, S. J. Pennycook, and Y. Yan, "Grain-boundary-enhanced carrier collection in CdTe solar cells," *Physical Review Letters*, vol. 112, no. 15, pp. 1–5, 2014.

[17]   L. Kronik, D. Cahen, and H. W. Schock, "Effects of Sodium on Polycrystalline Cu(In,Ga)Se2 and Its Solar Cell Performance," *Advanced Materials*, vol. 10, no. 1, pp. 31–36, 1998.

[18]   S.-H. Wei, S. B. Zhang, and A. Zunger, "Effects of Na on the electrical and structural properties of CuInSe2," *Journal of Applied Physics*, vol. 85, no. 10, pp. 7214–7218, 1999.

[19]   A. Rockett and R. W. Birkmire, "CuInSe2 for photovoltaic applications," *Journal of Applied Physics*, vol. 70, no. 7, 1991.

[20]   P. Würfel and U. Würfel, *Physics of solar cells : from basic principles to advanced concepts*. Wiley-VCH, 2009.

[21]   P. Jackson, R. Wuerz, D. Hariskos, E. Lotter, W. Witte, and M. Powalla, "Effects of heavy alkali elements in Cu(In,Ga)Se2 solar cells with efficiencies up to 22.6%," *Physica Status Solidi - Rapid Research Letters*, vol. 10, no. 8, pp. 583–586, 2016.

[22]   M. A. Contreras, J. Tuttle, A. Gabor, A. Tennant, K. Ramanathan, S. Asher, A. Franz, J. Keane, L. Wang, J. Scofield, and R. Noufi, "High Efficiency Cu(ln,Ga)Se2 based solar cells: Processing of novel absorber structures," in *IEEE Photovoltaics Specialist Conference*, (Hawaii), pp. 68–75, 1994.

[23] M. A. Contreras, J. Tuttle, A. Gabor, A. Tennant, K. Ramanathan, S. Asher, A. Franz, J. Keane, L. Wang, and R. Noufi, "High efficiency graded bandgap thin-film polycrystalline Cu(In,Ga)Se2 - based solar cells," *Solar Energy Materials and Solar Cells*, vol. 42, pp. 231–246, 1996.

[24] K. Ramanathan, G. Teeter, J. C. Keane, and R. Noufi, "Properties of high-efficiency CuInGaSe2 thin film solar cells," *Thin Solid Films*, vol. 480-481, pp. 499–502, 2005.

[25] A. Chirilă, P. Reinhard, F. Pianezzi, P. Bloesch, A. R. Uhl, C. Fella, L. Kranz, D. Keller, C. Gretener, H. Hagendorfer, D. Jaeger, R. Erni, S. Nishiwaki, S. Buecheler, and A. N. Tiwari, "Potassium-induced surface modification of Cu(In,Ga)Se2 thin films for high-efficiency solar cells.," *Nature materials*, vol. 12, no. December, pp. 1107–11, 2013.

[26] P. Reinhard, A. Chirila, P. Blosch, F. Pianezzi, S. Nishiwaki, S. Beucheler, and A. N. Tiwari, "Review of Progress Toward 20% Efficiency Flexible CIGS Solar Cells and Manufacturing Issues of Solar Modules," *IEEE Journal of Photovoltaics*, vol. 3, no. 1, pp. 572–580, 2013.

[27] R. Caballero, C. A. Kaufmann, T. Eisenbarth, T. Unold, R. Klenk, and H. W. Schock, "Highe efficiency low temperature grown Cu(In,Ga)Se2 thin film solar cells on flexible substrates using NaF precursor layers," *Progress in Photovoltaics: Research and Applications*, vol. 19, no. 5, pp. 547–551, 2011.

[28] E. Eser, S. Fields, W. K. Kim, E. McQuiston, K. Kim, and W. N. Shafarman, "Cu(InGa)Se2 photovoltaics on insulated stainless steel web substrate," *Conference Record of the IEEE Photovoltaic Specialists Conference*, pp. 661–666, 2010.

[29] A. N. Tiwari, M. Krejci, F.-J. Haug, and H. Zogg, "12.8cu(in,ga)se2 solar cell on a flexible polymer sheet," *Progress in photovoltaics research and application*, vol. 7, no. 5, pp. 393–397, 1999.

[30] J. H. Yun, K. H. Kim, M. S. Kim, B. T. Ahn, S. J. Ahn, J. C. Lee, and K. H. Yoon, "Fabrication of CIGS solar cells with a Na-doped Molayer on a Na-free substrate," *Thin Solid Films*, vol. 515, pp. 5876–5879, may 2007.

[31] T. Wada, N. Kohara, S. Nishiwaki, and T. Negami, "Characterization of the Cu(In,Ga)Se2/Mo interface in CIGS solar cells," *Thin Solid Films*, vol. 387, pp. 118–122, jan 2001.

[32] K. Orgassa, H. W. Schock, and J. H. Werner, "Alternative back contact materials for thin film Cu(In,Ga)Se2 solar cells," *Thin Solid Films*, vol. 431-432, no. 03, pp. 387–391, 2003.

[33] T. Nakada, Y. Hirabayashi, T. Tokado, D. Ohmori, and T. Mise, "Novel device structure for cu(in,ga)se$_2$ thin film solar cells using transparent conducting oxide back and front contacts," *SOLAR ENERGY*, vol. 77, no. 6, pp. 739–747, 2004.

[34] M. A. Contreras, A. M. Gabor, A. Tennant, S. Asher, J. Tuttle, and R. Noufi, "Accelerated publication 16.4% total area conversion efficiency thin-film polycrystalline MgF2/ZnO/CdS/Cu(In,Ga)Se2/Mo solar cell," *Progress in Photovoltaics: Research and Applications*, vol. 2, no. 4, pp. 287–292, 1994.

[35] V. Kapur, U. Choudary, and A. Chu, "Process of forming a compound semiconductive material," Apr. 8 1986. US Patent 4,581,108.

[36] S. Niki, M. Contreras, I. Repins, M. Powalla, K. Kushiya, S. Ishizuka, and K. Matsubara, "CIGS absorbers and processes," *Progress in Photovoltaics: Research and Applications*, vol. 18, pp. 453–466, sep 2010.

[37] M. A. Green, Y. Hishikawa, W. Warta, E. D. Dunlop, D. H. Levi, J. Hohl-Ebinger, and A. W. Ho-Baillie, "Solar cell efficiency tables (version 50)," *Progress in Photovoltaics: Research and Applications*, vol. 25, no. 7, pp. 668–676, 2017.

[38] C. J. Hibberd, E. Chassaing, W. Liu, D. B. Mitzi, D. Lincot, and A. N. Tiwari, "Non-vacuum methods for formation of Cu(In, Ga)(Se, S)2 thin film photovoltaic absorbers," *Progress in Photovoltaics: Research and Applications*, vol. 18, no. 6, pp. 434–452, 2010.

[39] J. Palm, V. Probst, W. Stetter, R. Toelle, S. Visbeck, H. Calwer, T. Niesen, H. Vogt, O. Hernández, M. Wendl, and F. H. Karg, "CIGSSe thin film PV modules: From fundamental investigations to advanced performance and stability," *Thin Solid Films*, vol. 451-452, pp. 544–551, 2004.

[40] D. M. Berg, F. Cheng, and W. N. Shafarman, "H2S reaction of Se-capped metallic precursors to form Cu(In,Ga)(S,Se)2 absorber layers," in *IEEE Photovoltaic Specialists Conference*, (Denver, CO), pp. 323–327, 2014.

[41] B. Basol, M. Pinarbasi, S. Aksu, J. Wang, Y. Matus, T. Johnson, Y. Han, M. Narasimham, and B. Metin, "Electro- plating based technolgy for roll-to-roll manufacturing," *23rd EU PVSEC*, 2008.

[42] W. Wang, Y. W. Su, and C. H. Chang, "Inkjet printed chalcopyrite CuInxGa1-xSe2 thin film solar cells," *Solar Energy Materials and Solar Cells*, vol. 95, pp. 2616–2620, 2011.

[43] C. R. Abernathy, C. W. Bates, A. a. Anani, B. Haba, and G. Smestad, "Production of single phase chalcopyrite CuInSe2 by spray pyrolosis.," *Applied Physics Letters*, vol. 45, no. 1984, pp. 890–892, 1984.

[44] D. A. Eisenberg, M. Yu, C. W. Lam, O. A. Ogunseitan, and J. M. Schoenung, "Comparative alternative materials assessment to screen toxicity hazards in the life cycle of CIGS thin film photovoltaics," *Journal of Hazardous Materials*, vol. 260, 2013.

[45] N. Naghavi, S. Spiering, M. Powalla, B. Cavana, and D. Lincot, "High-efficiency copper indium gallium diselenide (CIGS) solar cells with indium sulfide buffer layers deposited by atomic layer chemical vapor deposition (ALCVD)," *PROGRESS IN PHOTOVOLTAICS*, vol. 11, pp. 437–443, NOV 2003.

[46] T. Nakada and M. Mizutani, "18% efficiency Cd-free Cu(In, Ga)Se-2 thin-film solar cells fabricated using chemical bath deposition (CBD)-ZnS buffer layers," *JAPANESE JOURNAL OF APPLIED PHYSICS PART 2-LETTERS*, vol. 41, pp. L165–L167, FEB 15 2002.

[47] T. Toerndahl, C. Platzer-Bjoerkman, J. Kessler, and M. Edoff, "Atomic layer deposition of Zn1-xMgxO buffer layers for Cu(In,Ga)Se2 solar cells," *Progress in Photovoltaics: Research and Applications*, vol. 15, pp. 225–235, MAY 2007.

[48] T. M. Friedlmeier, P. Jackson, A. Bauer, D. Hariskos, O. Kiowski, R. Wuerz, and M. Powalla, "Improved Photocurrent in Cu(In, Ga)Se-2 Solar Cells: From 20.8% to 21.7% Efficiency with CdS Buffer and 21.0% Cd-Free," *IEEE JOURNAL OF PHOTOVOLTAICS*, vol. 5, pp. 1487–1491, SEP 2015.

[49] U. Rau, P. O. Grabitz, and J. H. Werner, "Resistive limitations to spatially inhomogeneous electronic losses in solar cells," *Applied Physics Letters*, vol. 85, no. 24, pp. 6010–6012, 2004.

[50] S.-H. Wei and A. Zunger, "Calculated natural band offsets of all II–VI and III–V semiconductors: Chemical trends and the role of cation d orbitals," *Applied Physics Letters*, vol. 72, no. 16, p. 2011, 1998.

[51] P. Jackson, D. Hariskos, R. Wuerz, O. Kiowski, A. Bauer, T. M. Friedlmeier, and M. Powalla, "Properties of Cu(In,Ga)Se2 solar cells with new record efficiencies up to 21.7%," *Physica Status Solidi (RRL) - Rapid Research Letters*, vol. 9, pp. 28–31, 2015.

[52] F. Kröger and H. Vink, "Relations between the Concentrations of Imperfections in Crystalline Solids," *Solid State Physics*, vol. 3, pp. 307–435, 1956.

[53] U. Rau, K. Taretto, and S. Siebentritt, "Grain boundaries in Cu (In,Ga)(Se, S)2 thin-film solar cells," *Applied Physics A*, vol. 96, pp. 221–234, 2009.

[54] D. Cahen and R. Noufi, "Defect chemical explanation for the effect of air anneal on CdS/CuInSe2 solar cell performance," *Applied Physics Letters*, vol. 54, no. 6, p. 558, 1989.

[55] B. Tell, J. L. Shay, and H. M. Kasper, "Room-temperature electrical properties of ten I-III-VI2 semiconductors," *Journal of Applied Physics*, vol. 43, no. 1972, pp. 2469–2470, 1972.

[56] R. Noufi, R. Axton, C. Herrington, and S. K. Deb, "Electronic Properties versus Composition of Thin Films of CuInSe2," *Applied Physics Letters*, vol. 45, no. 1984, pp. 668–670, 1984.

[57] S. B. Zhang, S.-h. Wei, and A. Zunger, "Defect physics of the CuInSe2 chalcopyrite semiconductor," *Physical Review B*, vol. 57, no. 16, pp. 9642–9656, 1998.

[58] C. Persson and A. Zunger, "Anomalous Grain Boundary Physics in Polycrystalline CuInSe2: The Existence of a Hole Barrier," *Physical Review Letters*, vol. 91, no. 26, p. 266401, 2003.

[59] C. Persson and A. Zunger, "Compositionally induced valence-band offset at the grain boundary of polycrystalline chalcopyrites creates a hole barrier," *Applied Physics Letters*, vol. 87, no. 21, pp. 1–4, 2005.

[60] Y. Yan, C.-S. Jiang, R. Noufi, S.-H. Wei, H. Moutinho, and M. Al-Jassim, "Electrically Benign Behavior of Grain Boundaries in Polycrystalline CuInSe2 Films," *Physical Review Letters*, vol. 99, no. 23, p. 235504, 2007.

[61] O. Cojocaru-Miredin, C. Pyuck-Pa, D. Abou-ras, S. S. Schmidt, R. Caballero, and D. Raabe, "Characterization of grain boundaries in Cu(In,Ga)Se2 Films using Atom Probe Tomography," *IEEE Journal of Photovoltaics*, vol. 1, no. 2, pp. 207–212, 2011.

[62] C. Lei, C. M. Li, A. Rockett, and I. M. Robertson, "Grain boundary compositions in Cu(InGa)Se2," *Journal of Applied Physics*, vol. 101, no. 2, p. 024909, 2007.

[63] M. J. Hetzer, Y. M. Strzhemechny, M. Gao, M. a. Contreras, a. Zunger, and L. J. Brillson, "Direct observation of copper depletion and potential changes at copper indium gallium diselenide grain boundaries," *Applied Physics Letters*, vol. 86, no. 16, p. 162105, 2005.

[64] M. Kawamura, T. Yamada, N. Suyama, A. Yamada, and M. Konagai, "Grain Boundary Evaluation of Cu(In,Ga)Se2 Solar Cells," *Japanese Journal of Applied Physics*, vol. 49, p. 062301, 2010.

[65] M. J. Romero, H. Du, G. Teeter, Y. Yan, and M. M. Al-Jassim, "Comparative study of the luminescence and intrinsic point defects in the kesterite Cu2ZnSnS4 and chalcopyrite Cu(In,Ga)Se2 thin films used in photovoltaic applications," *Physical Review B*, vol. 84, p. 165324, 2011.

[66] J. Kim, S. Kim, C.-S. Jiang, K. Ramanathan, and M. M. Al-Jassim, "Direct imaging of enhanced current collection on grain boundaries of Cu(In,Ga)Se2 solar cells," *Applied Physics Letters*, vol. 104, no. 063902, pp. 1–5, 2014.

[67] M. Takihara, T. Minemoto, Y. Wakisaka, and T. Takahashi, "An investigation of band profile around the grain boundary of Cu(InGa)Se2 solar cell material by scanning probe

microscopy," *Progress in Photovoltaics: Research and Applications*, vol. 21, pp. 595–599, 2013.

[68] S. Siebentritt, S. Sadewasser, M. Wimmer, C. Leendertz, T. Eisenbarth, and M. Lux-Steiner, "Evidence for a Neutral Grain-Boundary Barrier in Chalcopyrites," *Physical Review Letters*, vol. 97, no. 14, p. 146601, 2006.

[69] C.-S. Jiang, M. a. Contreras, I. Repins, H. R. Moutinho, Y. Yan, M. J. Romero, L. M. Mansfield, R. Noufi, and M. M. Al-Jassim, "How grain boundaries in Cu(In,Ga)Se2 thin films are charged: Revisit," *Applied Physics Letters*, vol. 101, no. 3, p. 033903, 2012.

[70] S. Siebentritt, "What limits the efficiency of chalcopyrite solar cells?," *Solar Energy Materials and Solar Cells*, vol. 95, no. 6, pp. 1471–1476, 2011.

[71] I. Repins, L. Mansfield, A. Kanevce, S. A. Jensen, D. Kuciauskas, S. Glynn, T. Barnes, W. Metzger, J. Burst, C.-s. Jiang, P. Dippo, S. Harvey, C. Perkins, B. Egaas, A. Zakutayev, J.-h. Alsmeier, T. Lußky, R. G. Wilks, M. Bär, Y. Yan, S. Lany, P. Zawadzki, J.-s. Park, S. Wei, N. Renewable, H.-z. Berlin, E. Gmbh, and B. T. U. Cottbus-senftenberg, "Wild Band Edges : The Role of Bandgap Grading and Band-Edge Fluctuations in High-Efficiency Chalcogenide Devices," in *IEEE Photovoltaic Specialist Conference*, (New Orleans, LA), pp. 309–314, 2016.

[72] D. Abou-Ras, N. Schäfer, C. J. Hages, S. Levcenko, J. Márquez, and T. Unold, "Inhomogeneities in Cu(In,Ga)Se ₂ Thin Films for Solar Cells: Band-Gap Versus Potential Fluctuations," *Solar RRL*, vol. 1700199, p. 1700199, 2017.

[73] W. Shockley and H. J. Queisser, "Detailed balance limit of efficiency of p☐n junction solar cells," *Journal of Applied Physics*, vol. 32, no. 510, pp. 1–11, 1961.

[74] M. Gloeckler and J. R. Sites, "Efficiency limitations for wide-band-gap chalcopyrite solar cells," *Thin Solid Films*, vol. 480-481, pp. 241–245, 2005.

[75] M. Contreras, L. Mansfield, B. Egaas, J. Li, M. Romero, and R. Noufi, "Improved energy conversion efficiency in wide-bandgap Cu(In,Ga)Se2 solar cells," in *IEEE Photovoltaic Specialists Conference*, (Seattle, Washington), pp. 1–6, 2011.

[76] T. Eisenbarth, T. Unold, R. Caballero, C. Kaufmann, D. Abou-Ras, and H.-W. Schock, "Origin of defects in CuIn1–xGaxSe2 solar cells with varied Ga content," *Thin Solid Films*, vol. 517, no. 7, pp. 2244–2247, 2009.

[77] W. N. Shafarman, R. Klenk, and B. E. Mccandless, "Device and material characterization of Cu(InGa)Se2 solar cells with increasing band gap," *Journal of Applied Physics*, vol. 79, no. 9, pp. 7324–7328, 1996.

[78] G. Hanket, J. Boyle, and W. Shafarman, "Characterization and device performance of (AgCu)(InGa)Se2 absorber layers," *IEEE Photovoltaic Specialists Conference*, pp. 1240–1245, 2009.

[79] Argonne National Laboratory Presentation, "Basics of Synchrotron Radiation Beamlines and Detectors," 2007.

[80] D. H. Bilderback, P. Elleaume, and E. Weckert, "Review of third and next generation synchrotron light sources," *Journal of Physics B: Atomic, Molecular and Optical Physics*, vol. 38, pp. S773–S797, 2005.

[81] O. F. Vyvenko, T. Buonassisi, A. Istratov, and E. R. Weber, "X-ray beam induced current/microprobe x-ray fluorescence: synchrotron radiation based x-ray microprobe techniques for analysis of the recombination activity and chemical nature of metal impurities in silicon," *Journal of Physics*, vol. 16, no. 2, pp. 1–12, 2004.

[82] T. Buonassisi, O. F. Vyvenko, A. A. Istratov, E. R. Weber, G. Hahn, D. Sontag, J. P. Rakotoniaina, O. Breitenstein, J. Isenberg, and R. Schindler, "Observation of transition metals at shunt locations in multicrystalline silicon solar cells," *Journal of Applied Physics*, vol. 95, no. 3, pp. 1556–1561, 2004.

[83] W. Seifert, O. Vyvenko, T. Arguirov, M. Kittler, M. Salome, M. Seibt, and M. Trushin, "Synchrotron-based investigation of iron precipitation in multicrystalline silicon," *Superlattices and Microstructures*, vol. 45, no. 4-5, pp. 168–176, 2009.

[84] W. Seifert, O. F. Vyvenko, T. Arguirov, A. Erko, M. Kittler, C. Rudolf, M. Salome, M. Trushin, and I. Zizak, "Synchrotron microscopy and spectroscopy for analysis of crystal defects in silicon," *Physica Status Solidi (C)*, vol. 6, no. 3, pp. 765–771, 2009.

[85] M. I. Bertoni, D. P. Fenning, M. Rinio, V. Rose, M. Holt, J. Maser, and T. Buonassisi, "Nanoprobe X-ray fluorescence characterization of defects in large-area solar cells," *Energy & Environmental Science*, vol. 4, pp. 4252–4257, 2011.

[86] B. West, H. Guthrey, L. Chen, A. Jeffries, S. Bernardini, B. Lai, J. Maser, W. Shafarman, M. Ai-jasim, M. Bertoni, and I. A. Fulton, "Electrical and Compositional Characterization of Gallium Grading in Cu(In,Ga)Se2 Solar Cells," (Denver, CO), pp. 1726–1728, 2014.

[87] B. West, S. Husein, M. Stuckelberger, B. Lai, J. Maser, B. Stripe, V. Rose, H. Guthrey, M. Al-jassim, and M. Bertoni, "Correlation between grain composition and charge carrier collection in Cu(In,Ga)Se2 solar cells," (New Orleans, LA), pp. 1–4, 2015.

[88] B. West, M. Stuckelberger, H. Guthrey, L. Chen, B. Lai, J. Maser, J. J. Dynes, W. Shafarman, M. Al-jassim, and M. I. Bertoni, "Synchrotron x-ray characterization of alkali elements at grain boundaries in Cu(In,Ga)Se2 solar cells," (Portland, OR), 2016.

[89] B. M. West, M. Stuckelberger, A. Jeffries, S. Gangam, B. Lai, B. Stripe, J. Maser, V. Rose, S. Vogt, and M. I. Bertoni, "X-ray fluorescence at nanoscale resolution for multicomponent layered structures: a solar cell case study," *Journal of Synchrotron Radiation*, vol. 24, no. 1, pp. 1–8, 2017.

[90] B. M. West, M. Stuckelberger, H. Guthrey, L. Chen, B. Lai, J. Maser, V. Rose, W. Shafarman, M. Al-Jassim, and M. I. Bertoni, "Grain Engineering: How Nanoscale Inhomogeneities Can Control Charge Collection in Solar Cells," *Nano Energy*, vol. 32, pp. 488–493, 2017.

[91] M. E. Stuckelberger, T. Nietzold, B. West, R. Farshchi, D. Poplavskyy, J. Bailey, B. Lai, J. M. Maser, and M. I. Bertoni, "How Does CIGS Performance Depend on Temperature at the Microscale?," *IEEE Journal of Photovoltaics*, pp. 1–10, 2017.

[92] M. Stuckelberger, B. West, S. Husein, H. Guthrey, M. Al-Jassim, R. Chakraborty, T. Buonassisi, J. M. Maser, B. Lai, B. Stripe, *et al.*, "Latest developments in the x-ray based characterization of thin-film solar cells," (New Orleans, LA), pp. 1–6, 2015.

[93] B. Watts, D. Queen, A. L. D. Kilcoyne, T. Tyliszczak, F. Hellman, and H. Ade, "Soft X-ray beam induced current technique," in *Journal of Physics: Conference Series*, vol. 186, p. 012023, 2009.

[94] M. Stuckelberger, T. Nietzold, G. Hall, B. West, J. Werner, B. Niesen, C. Ballif, V. Rose, D. Fenning, and M. Bertoni, "Charge Collection in Hybrid Perovskite Solar Cells: Relation to the Nanoscale Elemental Distribution," *IEEE Journal of Photovoltaics*, vol. 7, no. 2, pp. 590–597, 2017.

[95] A. Johannes, D. Salomon, G. Martinez-criado, and M. Glaser, "In operando x-ray imaging of nanoscale devices : Composition , valence , and internal electrical fields," no. December, pp. 1–7, 2017.

[96] R. Winarski, M. Holt, V. Rose, P. Fuesz, D. Carbaugh, C. Benson, D. Shu, D. Kline, G. Stephenson, I. McNulty, and J. Maser, "A Hard X-ray Nanoprobe Beamline for Nanoscale Microscopy," *Journal of Synchrotron Radiation*, vol. 19, pp. 1056–1060, 2012.

[97] E. Nazaretski, H. Yan, K. Lauer, N. Bouet, X. Huang, W. Xu, J. Zhou, D. Shu, Y. Hwu, and Y. S. Chu, "Design and performance of an X-ray scanning microscope at the Hard X-ray Nanoprobe beamline of NSLS-II," *Journal of Synchrotron Radiation*, vol. 24, pp. 1113–1119, nov 2017.

[98] G. Martinez-Criado, J. Villanova, R. Tucoulou, D. Salomon, J. P. Suuronen, S. Laboure, C. Guilloud, V. Valls, R. Barrett, E. Gagliardini, Y. Dabin, R. Baker, S. Bohic, C. Cohen, and J. Morse, "ID16B: A hard X-ray nanoprobe beamline at the ESRF for nano-analysis," *Journal of Synchrotron Radiation*, vol. 23, pp. 344–352, 2016.

[99]   F. Salvat, J. M. Fernandez-Varea, E. Acosta, and J. Sempau, "PENELOPE, A Code System for Monte Carlo Simulation of Electron and Photon Transport," 2001. Available at: http://www.oecdnea. org/tools/abstract/detail/nea-1525 (accessed October 4, 2016.

[100] R. Alig, S. Bloom, and C. Struck, "Scattering by ionization and phonon emission in semiconductors," *Physical Review B*, vol. 22, no. 12, pp. 5565–5582, 1980.

[101] A. Walsh and K. T. Butler, "Prediction of electron energies in metal oxides," *Accounts of Chemical Research*, vol. 47, no. 2, pp. 364–372, 2014.

[102] S. O. Kasap and J. A. Rowlands, "Direct-conversion flat-panel X-ray image sensors for digital radiography," vol. 90, (New Orleans, LA), pp. 591–604, 2002.

[103] J. Emara, T. Schnier, N. Pourdavoud, T. Riedl, K. Meerholz, and S. Olthof, "Impact of Film Stoichiometry on the Ionization Energy and Electronic Structure of CH3NH3PbI3 Perovskites," *Advanced Materials*, vol. 28, no. 3, pp. 553–559, 2016.

[104] J. Grant, W. Cunningham, A. Blue, V. O'Shea, J. Vaitkus, E. Gaubas, and M. Rahman, "Wide bandgap semiconductor detectors for harsh radiation environments," *Nuclear Instruments and Methods in Physics Research A*, vol. 546, pp. 213–217, 2005.

[105] A. Owens and A. Peacock, "Compound semiconductor radiation detectors," *Nuclear Instruments and Methods in Physics Research*, vol. 531, pp. 18–37, 2004.

[106] S. Awadalla, *Solid-state radiation detectors: technology and applications*. CRC Press, 2015.

[107] L. Berger, *Handbook of chemistry and physics*. CRC Press, 2015.

[108] S. J. Pearton, C. R. Abernathy, M. E. Overberg, G. T. Thaler, D. P. Norton, N. Theodoropoulou, A. F. Hebard, Y. D. Park, F. Ren, J. Kim, and L. A. Boatner, "Wide band gap ferromagnetic semiconductors and oxides," *Journal of Applied Physics*, vol. 93, no. 1, pp. 1–13, 2003.

[109] C. a. Klein, "Bandgap dependence and related features of radiation ionization energies in semiconductors," *Journal of Applied Physics*, vol. 39, no. 1968, pp. 2029–2038, 1968.

[110] M. E. Stuckelberger, T. Nietzold, B. M. West, B. Lai, M. Maser, V. Rose, and M. I. Bertoni, "X-Ray Beam Induced Voltage: A Novel Technique for Electrical Nanocharacterization of Solar Cells," (Washington, D.C.), pp. 1–7, 2017.

[111] T. Buonassisi, A. Istratov, M. Pickett, M. Heuer, J. Kalejs, G. Hahn, M. Marcus, B. Lai, Z. Cai, S. Heald, T. Ciszek, R. Clark, D. Cunningham, A. Gabor, R. Jonczyk, S. Narayanan, E. Sauar, and E. Weber, "Chemical natures and distributions of metal impurities in multicrystalline silicon materials," *Progress in Photovoltaics: Research and Applications*, vol. 14, no. 6, pp. 513–531, 2006.

[112] T. Paunesku, S. Vogt, J. Maser, B. Lai, and G. Woloschak, "X-Ray Fluorescence Microprobe Imaging in Biology and Medicine," *Journal of Cellular Biochemistry*, vol. 99, pp. 1489–1502, 2006.

[113] D. De Boer, "Calculation x-ray fluorescence intensities from bulk and multilayer samples," *X-Ray Spectrometry*, vol. 19, no. 3, pp. 145–154, 1990.

[114] A. Brunetti, B. Golosio, M. G. Melis, and S. Mura, "A high-quality multilayer structure characterization method based on X-ray fluorescence and Monte Carlo simulation," *Applied Physics A*, vol. 118, pp. 497–504, 2014.

[115] R. van Grieken and A. A. Markowicz, "Quantification in XRF Analysis of Intermediate-Thickness Samples," in *Handbook of X-ray spectometry*, ch. 6, pp. 407–432, New York: Marcel Dekker, Inc., second ed., 2002.

[116] T. Schoonjans, L. Vincze, V. A. Solé, M. Sanchez del Rio, P. Brondeel, G. Silversmit, K. Appel, and C. Ferrero, "A general Monte Carlo simulation of energy dispersive X-ray fluorescence spectrometers — Part 5," *Spectrochimica Acta Part B: Atomic Spectroscopy*, vol. 70, pp. 10–23, 2012.

[117] V. Solé, E. Papillon, M. Cotte, P. Walter, and J. Susini, "A multiplatform code for the analysis of energy-dispersive X-ray fluorescence spectra," *Spectrochimica Acta Part B: Atomic Spectroscopy*, vol. 62, no. 1, pp. 63–68, 2007.

[118] C. G. Ryan, B. E. Etschmann, S. Vogt, J. Maser, C. L. Harland, E. Van Achterbergh, and D. Legnini, "Nuclear microprobe - Synchrotron synergy: Towards integrated quantitative real-time elemental imaging using PIXE and SXRF," *Nuclear Instruments and Methods in Physics Research, Section B: Beam Interactions with Materials and Atoms*, vol. 231, pp. 183–188, 2005.

[119] M. O. Krause, "Atomic Radiative and Radiationless Yields for K and L shells," *Journal of physical chemistry reference data*, vol. 8, no. 2, pp. 307–322, 1979.

[120] J. Hubbell, P. Trehan, and N. Singh, "A Review, Bibliography, and Tabulation of K, L, and Higher Atomic Shell X-Ray Fluorescence Yields," *Journal of physical chemistry reference data*, vol. 23, no. 2, pp. 339–364, 1994.

[121] AXO-Dresden, "Thin Film XRF Reference Samples," 2015. [Online; accessed 15-June-2015].

[122] Q. Hu, M. Aboustait, M. T. Ley, J. C. Hanan, V. Rose, and R. Winarski, "Combined three-dimensional structure and chemistry imaging with nanoscale resolution," *Acta Materialia*, vol. 77, pp. 173–182, 2014.

[123] A. Beer, "Bestimmung der Absorption des rothen Lichts in farbigen Flüssigkeiten," *Annalen der Physik*, vol. 162, no. 5, pp. 78–88, 1852.

[124] M. J. Berger, J. H. Hubbell, S. M. Seltzer, J. Chang, J. S. Coursey, R. Sukumar, D. S. Zucker, and K. Olsen, "XCOM: Photon cross sections database," *NIST Standard reference database*, vol. 8, 2013.

[125] W. Yun, B. Lai, Z. Cai, J. Maser, D. Legnini, E. Gluskin, Z. Chen, A. a. Krasnoperova, Y. Vladimirsky, F. Cerrina, E. Di Fabrizio, and M. Gentili, "Nanometer focusing of hard x rays by phase zone plates," *Review of Scientific Instruments*, vol. 70, no. 5, p. 2238, 1999.

[126] S. Vogt, "MAPS : A set of software tools for analysis and visualization of 3D X-ray fluorescence data sets," *J. Phys. IV France*, vol. 104, pp. 635–638, 2003.

[127] S. Vogt, J. Maser, and C. Jacobsen, "Data analysis for X-ray fluorescence imaging," *Journal de Physique IV France*, vol. 104, pp. 617–622, 2003.

[128] M. Tsukahara, S. Mitrovic, V. Gajdosik, G. Margaritondo, L. Pournin, M. Ramaioli, D. Sage, Y. Hwu, M. Unser, and T. M. Liebling, "Coupled tomography and distinct-element-method approach to exploring the granular media microstructure in a jamming hourglass," *Physical Review E*, vol. 77, no. 6, p. 061306, 2008.

[129] G. W. Delaney, T. Di Matteo, and T. Aste, "Combining tomographic imaging and DEM simulations to investigate the structure of experimental sphere packings," *SOFT MATTER*, vol. 6, no. 13, pp. 2992–3006, 2010.

[130] Y. Fu, Y. Xi, Y. Cao, and Y. Wang, "X-ray microtomography study of the compaction process of rods under tapping," *Physical Review E*, vol. 85, no. 5, 1, p. 051311, 2012.

[131] T. Nietzold, B. M. West, M. Stuckelberger, B. Lai, S. Vogt, and M. I. Bertoni, "Quantifying x-ray fluorescence data using maps," *Journal of Visualized Experiments*, 2017.

[132] G. E. Lloyd, "Atomic Number and Crystallographic Contrast Images with the SEM: A Review of Backscattered Electron Techniques," *Mineralogical Magazine*, vol. 51, pp. 3–19, 1987.

[133] D. Abou-Ras, S. S. Schmidt, R. Caballero, T. Unold, H. W. Schock, C. T. Koch, B. Schaffer, M. Schaffer, P. P. Choi, and O. Cojocaru-Mirédin, "Confined and chemically flexible grain boundaries in polycrystalline compound semiconductors," *Advanced Energy Materials*, vol. 2, pp. 992–998, 2012.

[134] Y. Yan, W.-J. Yin, Y. Wu, T. Shi, N. R. Paudel, C. Li, J. Poplawsky, Z. Wang, J. Moseley, H. Guthrey, H. Moutinho, S. J. Pennycook, and M. M. Al-Jassim, "Physics of grain boundaries in polycrystalline photovoltaic semiconductors," *Journal of Applied Physics*, vol. 117, p. 112807, 2015.

[135] K. Gartsman, L. Chernyak, V. Lyahovitskaya, D. Cahen, V. Didik, V. Kozlovsky, R. Malkovich, E. Skoryatina, and V. Usacheva, "Direct evidence for diffusion and electromigration of Cu in CuInSe2," *Journal of Applied Physics*, vol. 82, no. 9, p. 4282, 1997.

[136] S.-H. Wei, S. B. Zhang, and A. Zunger, "Effects of Ga addition to CuInSe2 on its electronic, structural, and defect properties," *Applied Physics Letters*, vol. 72, no. 24, p. 3199, 1998.

[137] R. Khanal, D. B. Buchholz, R. P. H. Chang, and J. E. Medvedeva, "Composition-dependent structural and transport properties of amorphous transparent conducting oxides," *Physical Review B*, vol. 91, no. 20, pp. 1–13, 2015.

[138] M. Ramzan, T. Kaewmaraya, and R. Ahuja, "Molecular dynamics study of amorphous Ga-doped In2O3: A promising material for phase change memory devices," *Applied Physics Letters*, vol. 103, no. 7, pp. 1–5, 2013.

[139] A. Murat and J. E. Medvedeva, "Electronic properties of layered multicomponent wide-band-gap oxides: A combinatorial approach," *Physical Review B - Condensed Matter and Materials Physics*, vol. 85, no. 15, pp. 1–13, 2012.

[140] L. Gütay, C. Lienau, and G. H. Bauer, "Subgrain size inhomogeneities in the luminescence spectra of thin film chalcopyrites," vol. 97, no. 052110, pp. 1–3, 2010.

[141] J. R. Tuttle, M. A. Contreras, T. J. Gillespie, K. R. Ramanathan, A. L. Tennant, J. Keane, A. M. Gabor, and R. Noufi, "Accelerated publication 17.1efficient cu(in,ga)se2-based thin-film solar cell," *Progress in Photovoltaics: Research and Applications*, vol. 3, no. 4, pp. 235–238, 1995.

[142] D. Schroeder and A. Rockett, "Electronic effects of sodium in epitaxial $CuIn_{1-x}Ga_xSe_2$," *Journal of Applied Physics*, vol. 82, no. 10, pp. 4982–4985, 1997.

[143] M. Ruckh, D. Schmid, M. Kaiser, T. Schaffler, T. Walter, and H. W. Schock, "INFLUENCE OF SUBSTRATES ON THE ELECTRICAL PROPERTIES OF Cu(ln,Ga)Se, THIN FILMS," vol. 7059, (Waikoloa, HI), pp. 156–159, 1994.

[144] M. Bodegard, L. Stolt, and J. Hedestrom, "The influence of sodium on the grain structure of cuinse2 films for photovoltaic applications," *12th EU PVSEC*, pp. 1743–1746, 1994.

[145] U. Rau, M. Schmitt, D. Hilburger, F. Engelhardt, O. Seifert, J. Parisi, W. Riedl, J. Rimmasch, and F. Karg, "Influence of na and s incorporation on the electronic transport properties of cu (in, ga) se/sub 2/solar cells," in *IEEE Photovoltaic Specialists Conference*, (Washington, D.C.), pp. 1005–1008, 1996.

[146] J. Hedstrom, H. Ohlsen, M. Bodegard, A. Kylner, L. Stolt, D. Hariskos, M. Ruchh, and H.-W. Schock, "ZnO/CdS/Cu(In,Ga)Se2 thin film solar cells with improved performance," (Louisville, KY,), pp. 364–371, 1993.

[147] S. Ishizuka, A. Yamada, M. M. Islam, H. Shibata, P. Fons, T. Sakurai, K. Akimoto, and S. Niki, "Na-induced variations in the structural, optical, and electrical properties of Cu (In,Ga) Se2 thin films," *Journal of Applied Physics*, vol. 106, no. 3, 2009.

[148] M. Bodegard, K. Granath, L. Stolt, and A. Rockett, "Behavior of na implanted into mo thin films during annealing," *Solar energy Materials and Solar Cells*, vol. 58, pp. 199–208, 1999.

[149] D. Rudmann, A. F. Da Cunha, M. Kaelin, F. Kurdesau, H. Zogg, A. N. Tiwari, and G. Bilger, "Efficiency enhancement of Cu(In,Ga)Se2 solar cells due to post-deposition Na incorporation," *Applied Physics Letters*, vol. 84, no. 7, pp. 1129–1131, 2004.

[150] A. Rockett, J. S. Britt, T. Gillespie, C. Marshall, M. M. Al Jassim, F. Hasoon, R. Matson, and B. Basol, "Na in selenized Cu(In,Ga)Se2 on Na-containing and Na-free glasses: Distribution, grain structure, and device performances," *Thin Solid Films*, vol. 372, no. 1, pp. 212–217, 2000.

[151] M. Theelen, V. Hans, N. Barreau, H. Steijvers, Z. Vroon, and M. Zeman, "The impact of alkali elements on the degradation of cigs solar cells," *Progress in Photovoltaics: Research and Applications*, vol. 23, no. 5, pp. 537–545, 2015.

[152] J. Keller, R. Schlesiger, I. Riedel, J. Parisi, G. Schmitz, A. Avellan, and T. Dalibor, "Grain boundary investigations on sulfurized Cu(In,Ga)(S,Se)2 solar cells using atom probe tomography," *Solar Energy Materials and Solar Cells*, vol. 117, pp. 592–598, 2013.

[153] A. Stokes, M. Al-Jassim, A. Norman, D. Diercks, and B. Gorman, "Nanoscale insight into the p-n junction of alkali-incorporated cu(in,ga)se2 solar cells," *Progress in Photovoltaics: Research and Applications*, vol. 25, no. 9, pp. 764–772, 2017.

[154] A. Laemmle, R. Wuerz, T. Schwarz, O. Cojocaru-Miredin, P. P. Choi, and M. Powalla, "Investigation of the diffusion behavior of sodium in Cu(In,Ga)Se 2 layers," *Journal of Applied Physics*, vol. 115, no. 15, 2014.

[155] P. T. Erslev, J. W. Lee, W. N. Shafarman, and J. D. Cohen, "The influence of Na on metastable defect kinetics in CIGS materials," *Thin Solid Films*, vol. 517, pp. 2277–2281, feb 2009.

[156] L. Gutay and G. H. Bauer, "Non-uniformities of opto-electronic properties in Cu (In, Ga) Se2 thin films and their influence on cell performance studied with confocal photoluminescence," *Photovoltaic Specialists Conference (*, pp. 1–4, jan 2009.

[157] K. V. Kaznatcheev, C. Karunakaran, U. D. Lanke, S. G. Urquhart, M. Obst, and A. P. Hitchcock, "Soft X-ray spectromicroscopy beamline at the CLS: Commissioning results," *Nuclear Instruments and Methods in Physics Research, Section A: Accelerators, Spectrometers, Detectors and Associated Equipment*, vol. 582, no. 1, pp. 96–99, 2007.

[158] A. Sakdinawat and D. Attwood, "Nanoscale X-ray imaging," *Nature Photonics*, vol. 4, no. 12, pp. 840–848, 2010.

[159] R. K. Vasudevan, A. Tselev, A. P. Baddorf, and S. V. Kalinin, "Big-data reflection high energy electron diffraction analysis for understanding epitaxial film growth processes," *ACS Nano*, vol. 8, no. 10, pp. 10899–10908, 2014.

[160] S. V. Kalinin, B. G. Sumpter, and R. K. Archibald, "Big–deep–smart data in imaging for guiding materials design," *Nature Materials*, vol. 14, no. 10, pp. 973–980, 2015.

[161] A. M. Holder, S. Siol, P. F. Ndione, H. Peng, A. M. Deml, B. E. Matthews, L. T. Schelhas, M. F. Toney, R. G. Gordon, W. Tumas, J. D. Perkins, D. S. Ginley, B. P. Gorman, J. Tate, A. Zakutayev, and S. Lany, "Novel phase diagram behavior and materials design in heterostructural semiconductor alloys," *Science Advances*, vol. 3, no. June, 2017.

[162] A. Ichimiya and P. I. Cohen, *Reflection high-energy electron diffraction*. Cambridge University Press, 2004.

[163] R. Chakraborty, J. Serdy, B. West, M. Stuckelberger, B. Lai, J. Maser, M. I. Bertoni, M. L. Culpepper, and T. Buonassisi, "Development of an in situ temperature stage for synchrotron X-ray spectromicroscopy," *Review of Scientific Instruments*, vol. 86, no. 113705, pp. 1 – 6, 2015.

[164] B. M. West, M. Stuckelberger, L. Chen, R. Lovelett, B. Lai, J. Maser, W. Shafarman, and M. I. Bertoni, "Growth of Cu(In,Ga)(S,Se)$_2$ films: Unravelling the mysteries by in-situ X-ray imaging," in *IEEE Photovoltaic Specialists Conference*, (Portland, OR.), pp. 0530–0533, 2016.

[165] B. M. West, M. Stuckelberger, B. Lai, J. Maser, and M. I. Bertoni, "Kinetics at the nanoscale: the potential of in-situ X-ray microscopy and big data analytics," January 2018. [Submitted].

[166] F. Pedregosa, G. Varoquaux, A. Gramfort, V. Michel, B. Thirion, O. Grisel, M. Blondel, G. Louppe, P. Prettenhofer, R. Weiss, V. Dubourg, J. Vanderplas, A. Passos, D. Cournapeau, M. Brucher, M. Perrot, and É. Duchesnay, "Scikit-learn: Machine Learning in Python," *Journal of Machine Learning Research*, vol. 12, pp. 2825–2830, 2012.

[167] T. Godecke, T. Haalboom, and F. Ernst, "Phase Equilibria of Cu-In-Se II. The In-In2S3-Cu2Se-Cu Subsystem," *Zeitschrift für Metallkunde*, vol. 91, no. 8, pp. 635–650, 2000.

[168] A. Brummer, V. Honkimäki, P. Berwian, V. Probst, J. Palm, and R. Hock, "Formation of CuInSe2 by the annealing of stacked elemental layers - Analysis by in situ high-energy powder diffraction," *Thin Solid Films*, vol. 437, no. 1-2, pp. 297–307, 2003.

[169] W. Kim, *Study of Reaction Pathways and Kinetics in Cu (InxGa1-x) Se2 Thin Film Growth*. PhD thesis, University of Florida, 2006.

[170] C. Chang, A. Davydov, B. Stanbery, and T. Anderson, "Thermodynamic assessment of the Cu-In-Se system and application to thin film photovoltaics," (Washington, D.C.), pp. 849–852, 1996.

[171] M. Purwins, A. Weber, P. Berwian, G. Müller, F. Hergert, S. Jost, and R. Hock, "Kinetics of the reactive crystallization of CuInSe2 and CuGaSe2 chalcopyrite films for solar cell applications," *Journal of Crystal Growth*, vol. 287, no. 2, pp. 408–413, 2006.

[172] J. Maser, B. Lai, T. Buonassisi, Z. Cai, S. Chen, L. Finney, S.-C. Gleber, R. Harder, C. Jacobsen, W. Liu, C. Murray, C. Preissner, C. Roehrig, V. Rose, D. Shu, D. Vine, and S. Vogt, "A next-generation in-situ nanoprobe beamline for the Advanced Photon Source," *Proc. SPIE*, vol. 8851, no. September 2015, pp. 885106–1–885106–6, 2013.

[173] B. M. West, M. Stuckelberger, L. Chen, R. Lovelett, B. Lai, J. Maser, W. Shafarman, and M. I. Bertoni, "Machine Learning and Correlative Microscopy: How Big Data Techniques can Benefit Thin Film Solar Cell Characterization," in *IEEE Photovoltaic Specialists Conference*, (Washington, D.C.), pp. 1–6, 2017.

[174] A. Dempster, N. Laird, and D. Rubin, *Maximum likelihood from incomplete data via the EM algorithm*, vol. 39. Wiley for the Royal Statistical Society, 1977.

[175] T. Hastie, R. Tibshirani, and J. Friedman, *The Statistical Learning*, vol. 1. Springer-Verlag New York, 2009.

[176] D. J. Griffiths, *Introduction to quantum mechanics*. Upper Saddle River, NJ: Pearson/Prentice Hall, 2nd ed.. ed., 2005.

[177] R. Mainz and R. Klenk, "In situ analysis of elemental depth distributions in thin films by combined evaluation of synchrotron x-ray fluorescence and diffraction," *Journal of Applied Physics*, vol. 109, p. 123515, jan 2011.

[178] A. G. Karydas, "Self-element secondary fluorescence enhancement in XRF analysis," *X-Ray Spectrometry*, vol. 34, no. 5, pp. 426–431, 2005.